UCONN LIBRARY

University of Connecticut
OpenCommons@UConn

Doctoral Dissertations | University of Connecticut Graduate School

11-10-2016

Ga2O3 Nanorod-based High Temperature Gas Sensors: A 3-D Nano- Architecture and Mechanism Study

HUI-JAN LIN
University of Connecticut - Storrs, hui-jan.lin@uconn.edu

Follow this and additional works at: https://opencommons.uconn.edu/dissertations

Recommended Citation
LIN, HUI-JAN, "Ga2O3 Nanorod-based High Temperature Gas Sensors: A 3-D Nano- Architecture and Mechanism Study" (2016). *Doctoral Dissertations*. 1265.
https://opencommons.uconn.edu/dissertations/1265

Ga_2O_3 Nanorod-based High Temperature Gas Sensors: A 3-D Nano-Architecture and Mechanism Study

Hui-Jan Lin, Ph.D

University of Connecticut, 2016

With the ever-demanding call for energy efficient industries and sustainable environment in the 21st century, monitoring and control of feedstock fuel combustion process are critically important in advanced energy generation systems such as power plants, gas turbines, and automotive engines, etc. The energy efficiency is essentially achieved through the fast, precise and self-sufficient measurement, as well as effective feedback control of physical parameters such as temperature and pressure, and chemical parameters such as specie concentration. However as of now, chemical and physical sensors that are able to operate in harsh environments, such as high temperature up to 1000 °C, are extremely limited due to the daunting challenges in structural stability, sensitivity, selectivity, and functional stability required in the sensor materials. In this study, we successfully synthesized large-scale three-dimensional (3-D) β-Ga_2O_3 nanorod arrays (NRAs) on Si substrates using a cost-effective hydrothermal deposition process followed by high temperature annealing. Based on these 3-D β-Ga_2O_3 NRAs, we design and investigate three material and sensor design strategies in order to improve and understand the new materials architecture and sensing mechanism at high temperature. Firstly, using trace amount of perovskite oxide nanoparticles decoration, 3-D β-Ga_2O_3 NRA gas sensors are not only sensitized to a degree that rivals noble metal nanoparticle sensitizing effect, but also greatly enhanced in their oxidative gas selectivity, e.g., in NO_2 detection over O_2. Secondly, post hydrogen treatment is utilized to tune the defects in the β-Ga_2O_3 to help enhance the sensor performance at high temperature.

Furthermore, UV-assisted photoelectron generation in wide bandgap β-Ga_2O_3 significantly enhanced the sensor performance. Finally, an in-depth understanding of the 3-D architecture and sensing mechanism is being pursued using various complementary spectroscopy tools such as *ex-situ* and *in-situ* X-ray Photoelectron Spectroscopies (XPS).

Ga_2O_3 Nanorod-based High Temperature Gas Sensors: A 3-D Nano-Architecture and Mechanism Study

Hui-Jan Lin

B.S., National Cheng Kung University, 2004

M.S., National Cheng Kung University, 2006

A Dissertation

Submitted in Partial Fulfillment of the

Requirements for the Degree of

Doctor of Philosophy

at the

University of Connecticut

2016

Copyright by

Hui-Jan Lin

2016

Approval Page

Doctor of Philosophy Dissertation

Ga_2O_3 Nanorod-based High Temperature Gas Sensors: A 3-D Nano-Architecture and Mechanism Study

Presented by

Hui-Jan Lin, B.S., M.S.

Major Advisor

_____

Puxian Gao

Associate Advisor

_____

Mei Wei

Associate Advisor

_____

Steven L. Suib

Associate Advisor

_____

Menka Jain

Associate Advisor

_____

Seok-Woo Lee

University of Connecticut
2016

To My Family

Acknowledgement

First of all, I would like to express the deepest appreciation to my advisor Professor Puxian Gao, who has guided me continuously in regard to the research study. Without his supervision and constant help this dissertation would not have been possible. During the past few years, he has provided intelligent discussion and suggestion not only about the research but also the meaning of the life. I am down to earth grateful to him for being a great mentor in all aspects.

I would also thank my committee members, Professor Mei Wei, Professor Steven L. Suib, Professor Menka Jain and Professor Seok-Woo Lee for their valuable comments, support, feedback and insightful criticism.

Also show my appreciation to research staffs in IMS, Dr. Roger Ristau and Dr. Lichun Zhang for their teaching and kind help in TEM operation. Dr. John Baltrus and Dr. Paul Ohodnicki from national energy technology laboratory in department of energy for their help in *in-situ* XPS, Dr. Chang-Yong Nam from Brookhaven National Laboratory for his insightful guidance and comments. Dr. Yong Ding from Georgia Tech for his help for the operation of high-angle annular dark field images of TEM.

Additionally, I would like to thank all my labmates. Dr. Yanbing Guo, Dr. Haiyong Gao, Dr. Zheng Ren, Dr. Greg Wrobel, Dr. Caihong Liu, Dr. Kuo-Ting Liao, Sanka Piyadasa, Sibo Wang, Mingwan Zhang for their valuable advices in the experiments.

Finally, I would like to express my sincere gratitude to my family- my father, mother, sister and brother- for their teaching, unselfish love during my life.

Thank you everyone in my life.

Table of Contents

CHAPTER 1

Introduction

1.1: Gas Sensor

The device that could detect environmental gases by interaction between its sensing element and gases is called gas sensor and there are two main parts, receptor and transducer, included in the gas sensor device. After the receptor is exposed to certain gas, the output signal of the device would change compared with the initial output signal in the environment. The changed output signal may also be transformed to real actions, such as sound alarms, turn on or off the machines by the transducer.

Gas sensors have been developed and studied for decades to monitor and detect the atmosphere and people can prevent to be exposed to harmful gases that might cause severely effects on human health. Before the electrical gas sensors were invented, canaries were traditionally used in coal mining as early detection systems against life threatening gases such as carbon monoxide and methane back in 1911. Normally, the canary is a very songful bird but it would stop singing and eventually die in the presence of these gases, signaling to the miners to exit the mine immediately. Although considered as moderately toxic compared to other highly poisonous gases, carbon monoxide (CO) detection has always been of vital importance as it lacks color, odor or taste and it is present in numerous natural and artificial environments.[4] Additionally, miners would carry one kind of safety lamp named Davy lamps, invented by Sir Humphry Davy in 1815, for use in flammable atmosphere to reduce the danger of explosions. Nowadays, more and more researches and technologies have been developed for gas detection and

applied in different areas such as daily life room temperature carbon monoxide detection or high temperature oxygen detection for mobile engines.

Gas sensors are becoming more and more important to protect human beings through detecting toxic, flammable and combustible gases. Moreover, theses sensors have been widely used in the area of automotive emission control, public security, environment hazard monitoring or medical diagnosis.

1.2: Gas Sensor Properties

For gas sensors, there are several important factors been emphasized, including sensitivity, response time, recovery time, stability and selectivity. All these factors are used to value the performance of the gas sensors.

Here we describe the brief definition of sensitivity, response time and recovery time that would be mentioned repeatedly through the thesis. As one of the most important parameters of gas sensor, much effort has been made to enhance the sensitivity of gas sensors and it has been attracting more and more attention for a long time. However, there is not a uniform definition for the sensitivity of gas sensors now. Based on the published literatures,[13] in the n-type metal oxide semiconductor gas sensors cases, sensitivity (S) is usually defined as R_a / R_g for reducing gases and R_g / R_a for oxidizing gases, where R_a represents the resistance of gas sensors in the reference gas and R_g represents the resistance of gas sensors in the reference gas containing target gases.[16] On the other hand, another popular definition of sensitivity refers to the ratio of the resistance change to the initial resistance of the gas sensor, for example, sensitivity of an n-type semiconductor gas sensor with exposure to reducing gases is labeled as $(R_a - R_g)/ (R_g)$.

Larger sensitivity value means the gas sensor material is more sensitive to certain targeting gas, which means the gas could be easily detected at certain concentration by the gas sensor material. Sensitivity is mostly related to the sensing material as well as the mechanism of the sensing system. Furthermore, the sensitivity can be affected by other parameters, such as operation temperatures, gas concentrations, gases species or humidity etc.

Response / Recovery time are typically defined as the time it takes for a gas sensor to read a certain percentage of full-scale reading after being exposed to target gas at a given concentration. Usually, it selects 90% of the full reading, named t_{90}, in the gas sensor which is shown in **Figure 1-1**. Therefore, for metal oxide semiconductor gas sensors, the response time is counted from beginning to 90% of saturated scale, while recovery time is calculated the time needed from the saturated to 10% of the full scale.

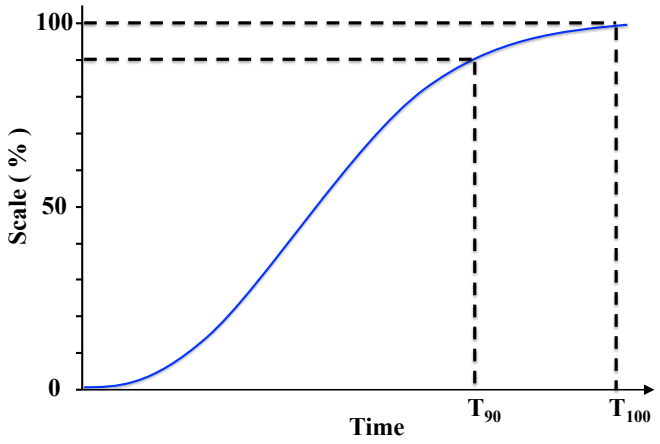

Figure 1-1: A typical sensor response and response time t_{90}.

In real applications, fast response / recovery time are very crucial for gas sensors. In the hazardous environments, the gas sensor device with fast response time could provide alarm signals immediately and evacuate or protect operating personnel; fast recovery

time is important for repeatable usage of gas sensors.

Selectivity (or specificity) is the ability for a gas sensor material to detect a target gas without affected by the presence of other interfering gases. Most gas sensor materials are sensitive to a family of gases and very few sensors specific for only one gas. Different techniques are employed in order to achieve some degree of selectivity to suit practical applications. For example, most hydrocarbons can be removed by passing through a charcoal filter while letting only CO, H_2 pass through.[17, 18] However, in solid-state sensors, temperature is another natural factor which can be used to differentiate gas species and create the selectivity since the surface temperature of gas sensors can be set differently in order to make it more sensitive to one gas and less sensitive to others. Additionally, the most popular way to reach the goal of selectivity is to build gas sensor arrays in the sensor device system. Since each portion of the sensor arrays has different sensitivity to certain gas, selective detection for the gas sensor system can be reached by means of both data analysis techniques and gas response database.[14]

Stability and detection limit of the gas sensors should also be tested for practical applications. The definition of stability is the ability for the gas sensor to provide reproducible results for a certain period of time, which means sensitivity, response time, recovery time and selectivity should retain in the time span. Detection limit is the lowest concentration of certain gases that can be detected or differentiated from the output signal under given conditions, particularly at a given temperature.

1.3: High Temperature Gas Sensor

Nowadays, large scale stationary power generation is dominated by fossil fuel based

combustion process, which usually involves combustion turbines or fuel-fired gasifiers. In both cases, high temperature and high pressure are typical harsh environments, which can reach 1300 °C in turbines and 1600 °C in gasifiers, while the respective pressure could reach 30 and 300 atmospheres. To ensure energy and fuel is operated efficiently in these systems, proper monitoring and control of their combustion processes is rather critical. This normally requires deployment of a number of various types of sensors to monitor chemical and physical parameters, such as specie concentrations, flow rate, temperature, as well as pressure. On the other hand, in a typical mobile energy generation system such as automotive engines, a number of oxygen and temperature sensors are usually deployed in our vehicles to ensure the rightful air/fuel ratio, combustion and emission control processes, with one of obvious outcomes being the fuel economy that we all care about. Meanwhile, during these energy production processes, the combustion induced emissions in both stationary and mobile energy systems are stringently regulated these days, which also require the critical functions provided by harsh environment sensors and control systems in order to give us a clean and sustainable energy generation process.[21]

According to U.S. Department of Energy (DOE), harsh environment sensors, if successfully and properly employed, are predicted to save 0.25 quadrillion BTU/year of energy across all industries.[28] As stated earlier, in both mobile and stationary energy industries, monitoring and control of the fuel combustion processes and the combustion-induced emissions hold the key for enhancing and ensuring sustainable energy and environment. However, commercially available sensor technologies for harsh environment are extremely limited due to the stringent requirements in sensor materials'

structural and functional stability in harsh environments, and the required high sensitivity and selectivity in sensor performance.[29] Therefore, there is an urgent need to develop rapidly responsive, highly sensitive, robust, and low cost high temperature sensors that are able to *in-situ* and real time monitor gaseous species in harsh environment.

High temperature solid-state gas sensors can be classified in three categories based on different sensing principles and sensor configurations. (I) Solid electrolyte-based gas sensors, including potentiometric and amperometric type gas sensors, (II) Resistive gas sensors and (III) Impedancemetric gas senors which could be operated in either solid electrolyte-based or semiconductor-based configurations.

1.3.1: Solid Electrolyte Based Gas Sensors

There are two major conduction mechanisms in semiconductor materials, one is electronic conduction and the other is ionic conduction. The transportation media of electron conduction are electrons and holes and the cause for ions conduction is from the migration of ions through point defects sites in the lattice instead.[30]

In solid electrolyte based sensors which include three minor types, equilibrium potentiometric, non-equilibrium potentiometric (mixed potential) and electrochemical pumping current (amperometric) types, ionic conductivity dominates the conduction and the electronic conduction contributes for a relatively small portion (usually less than 1%) to the total conductivity.[31] Here we will introduce working principles and configurations of each type.

(a) Equilibrium Potentiometric Type

The signal is measured by the potential difference between the working (sensing)

electrode and reference electrode. The potential difference should depend on the concentration of the analyte in gas or solid phases. However, the equilibrium potentiometric gas sensors have been classified into three types.[30]

Type I is the conventional solid-state ionic sensor, the gas to be detected is converted to the mobile component in a solid electrolyte. As shown in **Figure 1-2 (a)**, the working (sensing) component and the reference component are separated by the solid electrolyte, and a potential difference is established between the two sides of the solid electrolyte and also dependent on the difference in activity across the solid electrolyte of the species that will equilibrate with the conduction ions in the solid electrolyte. One popular example of type I gas sensor is an oxygen sensor with an oxygen-ion conductor, such as yttria-stabilized zirconia (YSZ). A porous layer of platinum (Pt) as the electrodes, and the reactions taking place at the three-phase contact points could be described as the following:

$$O_{2(gas)} + 4e^-_{(metal)} \Leftrightarrow 2O^{2-}_{(electrolyte)}$$

The electromotive force (EMF) of the cell is determined by the Nernst equation:

$$E = \frac{RT}{4F} \, ln \frac{P}{P_0}$$

where E represents electromotive, R is the gas constant, T is absolute temperature, F is Faraday's constant, P and P_0 stand for oxygen partial pressure at the sensing and reference sides, respectively. In addition, due to lack of suitable solid electrolytes, there're no solid electrolytes with mobile ions originating from other gases such as NO_x, SO_x or CO_2, although Matsumoto demonstrated non-solid state CO_3^{2-} mobile electrolyte on 2001.[32] Therefore, type I is usually used as O_2, H_2, F_2 or Cl_2 with corresponding solid

electrolytes (mobile ions) YSZ (O^{2-}), $HUO_2PO_4 \cdot 4H_2O$ (H^+), LaF_3 (F^-), $PbCl_2$-KCl (Cl^-), respectively.

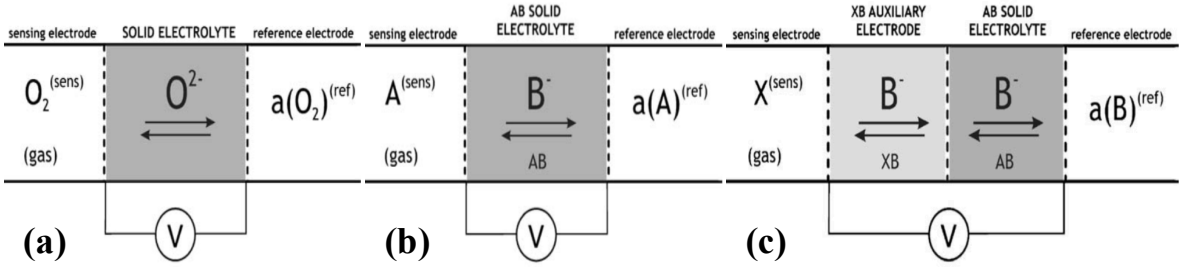

Figure 1-2: schematic illustration of (a) type I potentiometric gas sensor with oxygen conductor, (b) type II with anion conductor and (c) type III with anion conductor.[30]

Type II equilibrium potentiometric gas sensor does not have mobile ions of the chemical species (target gases) to be detected, but an ion related to the target gas can diffuse in the solid electrolyte to reach equilibrium with the atmosphere. Basically, type II has the same sensor configuration as type I, including a porous layer of metal electrode and the solid electrolyte between working (sensing) and reference electrodes shown in **Figure 1-2 (b)**. For example, solid electrolyte K_2CO_3 can be used as a CO_2 sensor. The only mobile ions of the solid electrolyte K_2CO_3, K^+, interacts with CO_2 molecules as below:

$$2K^+_{(electrolyte)} + CO_{2(gas)} + \frac{1}{2} O_{2(gas)} + 2e^-_{(metal)} \Leftrightarrow K_2CO_{3(electrolyte)}$$

Therefore, the concentration of CO_2 can be calculated by Nernst equation as well. In addition, type II equilibrium potentiometric gas sensor is usually used to sense CO_2, NO_x or SO_X.

Type III is known as a surface-modified solid-state ionic sensors. For practical applications, type I or type II potentiometric equilibrium gas sensor can only operate in certain cases. When taking other parameters into consideration, such as temperature or

gas pressure, the available equilibrium potentiometric gas sensors of either type I or type II would be very limited. Therefore, an additional auxiliary phase was introduced into the system shown in **Figure 1-2 (c)** to provide an equilibrium reaction between the target species and the ion that is mobile in the solid electrolyte, so that the voltage generated by the electrochemical cell is related to the concentration of the target species. Thus, the introduction of auxiliary phase covered on the electrodes would offer much more feasibility for practical applications at high temperature.[14, 33]

In summary, for all these three types of equilibrium potentiometric gas sensor discussed above, the output signal, EMF, follows the Nernst equation:

$$E = E^0 + \frac{RT}{nF}\, ln\ \ (\frac{p}{p_0})$$

(b) Non-Equilibrium Potentiometric Type

However, discrepancies were found and not fully followed the Nernst equation in practical applications. The discrepancies could be from that two or more competitive potentiometric reactions occur at the sensing electrode simultaneously, also knows as 'mixed potential'. **Figure 1-3** illustrates the sensing mechanism of a mixed-potential type YSZ-based H_2 sensor, which sensing electrode exposes to target gas (H_2 in air) and reference electrode exposes to reference gas (air). In the sensing electrode, a steady-state condition is achieved by the following two electrochemical reactions:

$$2H^+ + 2O^{2-} \rightarrow 2H_2O + 4e^-$$

$$O_2 + 4e^- \rightarrow 2O^{2-}$$

Therefore, a mixed potential can be generated when these two electrochemical reactions, the anodic reaction of H_2 and the cathodic reaction of O_2, reach a steady-state

condition. In addition, some percentage of the target gas will diffuse through the sensing electrode and be oxidized within the sensing electrode via gas-phase reaction as the following, shown in **Figure 1-3(d)**:

$$2H_2 + O_2 \rightarrow 2H_2O$$

Therefore, in the mixed-potential type gas sensor, the sensitivity of H_2 can be determined by the balance of three catalytic activities which were mentioned-above. Besides, several materials have been proposed as the auxiliary phase to improve the catalytic activity of the sensing electrode towards the target gas.

Mixed-potential type gas sensor can be used to detect various target gases if electrodes were selected properly. It's widely used to detect CO, NO_x and HCs in combustion exhausts. However, since it's highly dependent on kinetics, the response tends to decrease with increasing temperature, the operational temperature range of mixed-potential type gas sensor is limited.

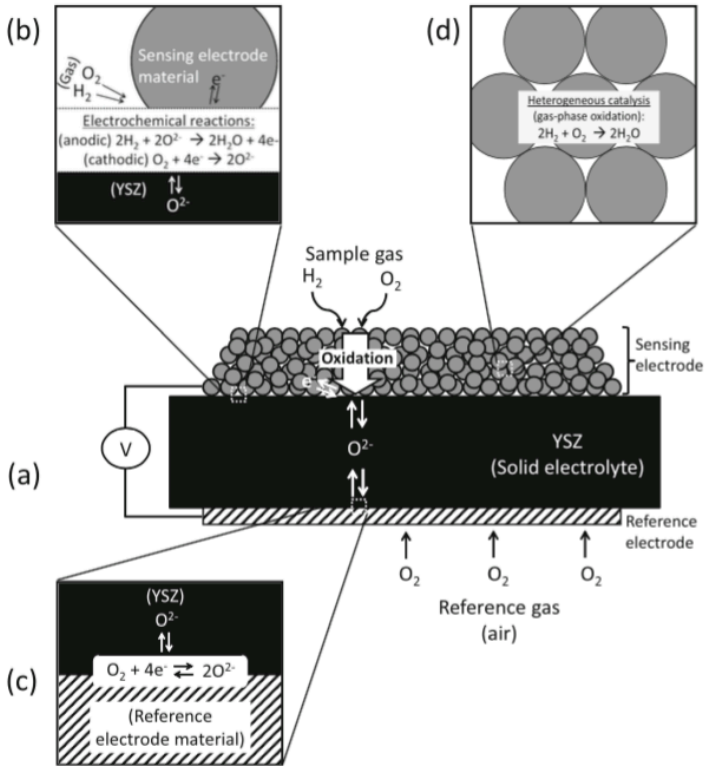

Figure 1-3: Illustration of (a) the typical construction of a mixed-potential type YSZ-based sensor, (b) the electrochemical reactions occurring at the SE/YSZ interface, (c) equilibrium RE reaction of O_2 at the RE/YSZ interface and (d) the gas-phase oxidation (heterogeneous catalysis) within the SE layer.[32]

(c) Electrochemical Pumping Current (Amperometric) Type

In contrast to potentiometric gas sensor, amperometric sensors have linear dependence of the electric signal on gas concentration, small temperature sensitivity. Furthermore, amperometric type gas senor has simpler construction due to lack of any reference electrode. Amperometric gas sensors are widely used in controlling the operatin of lean-burn engine due to their detection range, sensitivity and high temperature stability. **Figure 1-4** shows the typical type of amperemetric oxygen sensor which has a hole in the middle as the diffusion barrier. External voltage should be applied across the galvanic to occur the following electrochemical reactions:[34]

Cathode: $O_{2(gas)} + 4e^-_{(electrode)} \rightarrow 2O^{2-}_{(electrolyte)}$

Anode: $2O^{2-}_{(electrolyte)} \rightarrow O_{2(gas)} + 4e^-_{(electrode)}$

At cathode, oxygen molecules reduce to oxygen ion in the first place, and then move across the cell to reach the anode to oxidize to oxygen molecules. The limiting current is related to geometrical parameters of the diffusion barrier and oxygen concentration and can be described as below:

$$I_{lim} = -\frac{nFD_{O_2}AP_T}{RTL}\ln(1 - x_{o_2})$$

where I_{lim} represents the limiting current, n stands for the number of electrons involved in the reaction, F is the Faraday constan, D_{O_2} is the diffusion coefficient of O_2, A is the area of the diffusion hole, P_T is the total pressure, R is the gas constant, T is temperature, L is the length of the diffusion hole and x_{o_2} is the oxygen mole fraction. In the case of small values of oxygen mole fraction (below 10%), the logarithm becomes linear and I_{lim} can be described as the following:

$$I_{lim} = -\frac{nFD_{O_2}AP_T}{RTL}x_{O_2}$$

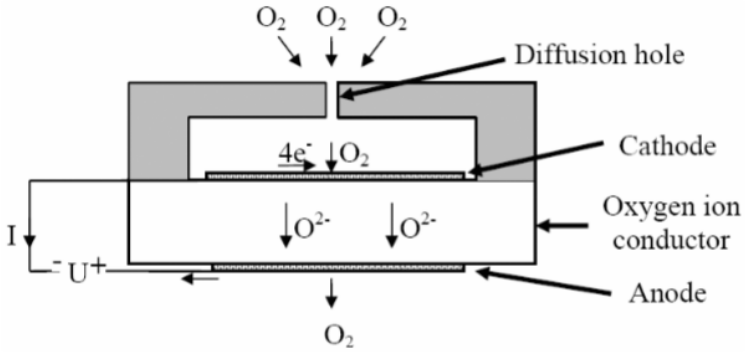

Figure 1-4: Design and sensing mechanism of a typical amperometric oxygen sensor with a hole as the diffusion barrier.[33]

1.3.2: Resistive Gas Sesnsor

In this research work, it's focused on the resistive type gas sensor and therefore we would elaborate more details about resistive gas sensor type in this section. Unlike the solid electrolyte type gas sensors, the resistive type gas sensors have relatively simple configuration, easy fabrication which might lead to low cost of manufacturer and possibility of miniaturization to micro electronic mechanical system through semiconductor manufacturing technology.

The resistive type gas sensor is based on metal oxide semiconductor material and it consists of the sensing element (metal oxide semiconductor) and the supported inert substrates which connected to two metallic electrodes or interdigitated electrodes, as shown in **Figure 1-5**.[12]

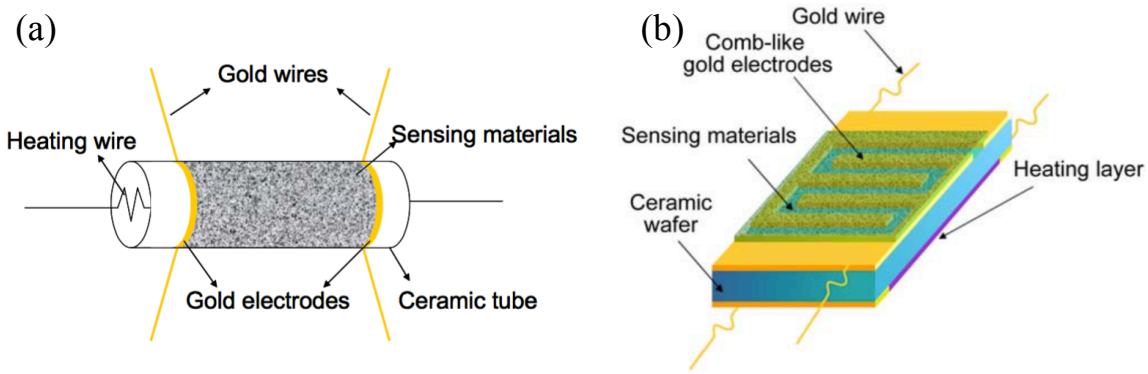

Figure 1-5: the configuration of the resistive types on (a) ceramic tube substrate with two gold wires as electrodes, (b) ceramic wafer substrate with gold interdigitated electrodes.[12]

The measured output signal of the resistive type gas sensor is electrical resistance that changes due to the interaction between target gas and the sensing element, i.e. metal oxide semiconductor. Based on the working mechanism, the resistive type gas sensor can be classified as:

(a): Surface conduction-based sensor:

In this type, the major working mechanism occurs on the surface of the metal oxide semiconductor. The change of output signal is either from the adsorption and desorption of gas species on the metal oxide surface or from the gas species react with lattice oxygen to form oxygen vacancies around the surface.

This working mechanism usually dominates at low to mid temperature, around 300-500 °C, and can be used to explain for sensors detecting exhaust gases such as CO, NO_x, SO_x or HCs. The detailed progress is that when the metal oxide semiconductor is exposed to atmosphere containing oxygen molecules, oxygen molecules are absorbed on the surface of metal oxides and would extract electrons from the conduction band E_c and trap the electrons at the surface in the form of ions such as O^-, O^{2-} or O_2^-. Therefore, a band banding and electron-deplete region, i.e. space-charge layer, will also created on the surface of semiconductor shown in **Figure 1-6 (a)**, Schottky barrier will also be form between the grain, shown in **Figure 1-6 (b)**. However, reaction of oxygen species with other gases or replacement of the adsorbed oxygen ions by other gas molecules would change the band bending and thus lead to change the conductivity. For example, when the gas sensor is exposed to CO in the reference gas, CO will be oxidized by O^- and release electrons back to the conduction band of the semiconductor. The number of surface O^- ions and the thickness of space-charge layer will decease. Followed by the lower Schottky barrier between the grains and lead to increased conductivity duo to the easier electron conduction in sensing later through different grains, which were shown in **Figure 1-6 (b)** and **(c)**.[13] However, the phenomenon will be opposite for p-type semiconductor.

Besides, the height of Schottky barrier, the thickness of the depletion layer or the density of the surface oxygen ions can be determined by the oxygen partial pressure of the atmosphere and thus, would influence the surface conductivity of the semiconductor.

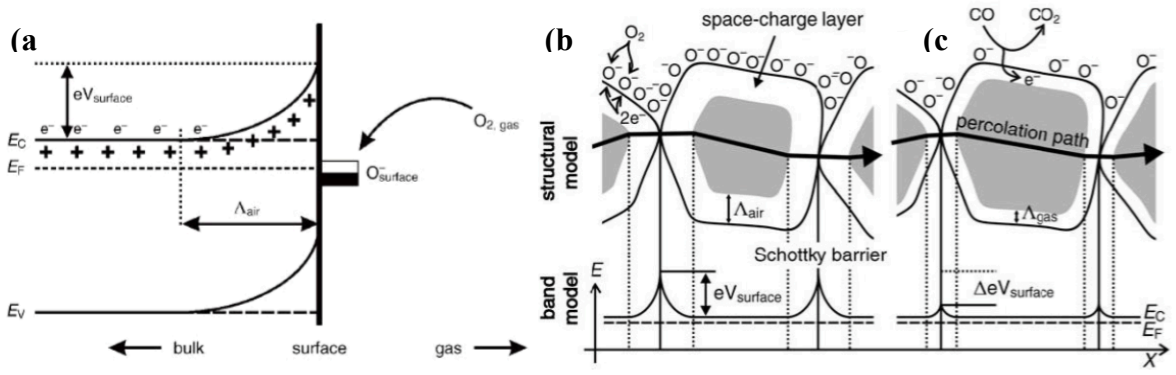

Figure 1-6: (a) Schematic diagram of band bending after chemisorptions of charged oxygen ions. E_c, E_v and E_F represent the energy of the conduction band, valence band and the Fermi level, respectively. Λ_{air} stands for the thickness of the space-charged layer, and $eV_{surface}$ denotes the potential barrier. e^- is the conducting electron and + represents the donor sites. (b) with and (c) without CO gas, structural and band models of conductive mechanism upon exposure to reference gas.[13]

(b) Bulk-conduction based sensors

Other than surface-conduction based sensors, bulk-conduction based sensors require higher temperature to induce the high mobility of the defect species in the materials. Basically speaking, a non-stoichiometric oxide semiconductor, an oxygen deficient leads to oxygen vacancies within the semiconductor. Furthermore, oxygen vacancies diffuse quickly no matter from interior of the grains to the surface or opposite. The reaction between oxygen molecules and the oxygen vacancies, $V_O^{\cdot\cdot}$, can be expressed as:

$$O_O^x \leftrightarrow V_O^{\cdot\cdot} + 2e^- + \frac{1}{2}O_{2(g)}$$

The relationship between oxygen partial pressure and the electrical conductivity (σ) of a bulk-conduction-based sensor would be represented as the following:

$$\sigma = \sigma_0 \exp\left(-\frac{E_A}{kT}\right) P_{O_2}^{\pm\frac{1}{n}}$$

where E_A is the activation energy which represents the sensitivity of the electrical conductivity to temperature changes. A positive dependence (+1/n) is usually observed at high oxygen pressure in the hold-conduction region, while a negative dependence (-1/n) is usually found at low oxygen pressure in the electron-conduction region. Therefore, select semiconductor material with small n and E_A would obtain high oxygen sensitivity and low interference to temperature fluctuation.[34, 35]

In summary, for high temperature gas sensor, particularly on the surface chemistry change with respect to low temperature range, the interactions between gas species and oxides can be described as three different scenarios according to temperature range that is shown in **Figure 1-7**:

(I) Upper - Low temperature: direct chemisorption of reducing gas onto the surface resulting in an injection of electrons into the solid.

(II) Middle – Medium temperature: oxygen defects will be generated on the surface of the metal oxide due to a surface reaction.

(III) Lower – High temperature: high defect mobility will be achieved due to high temperature, thus the inner lattice oxygen atom will transfer to the surface and change the crystal defect equilibrium.

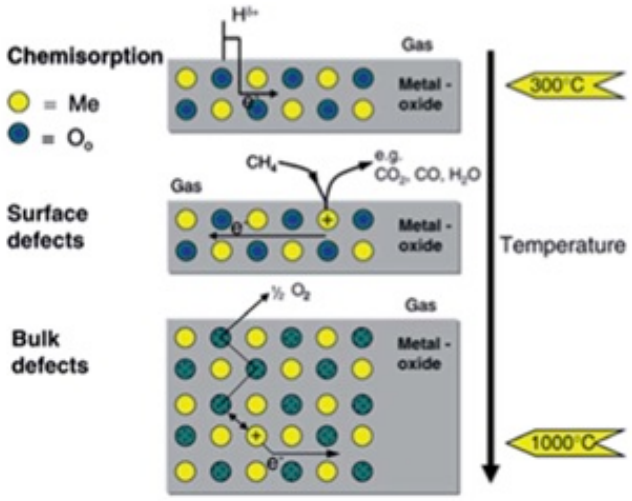

Figure 1-7: Model of the three regimes of gas reaction of simple oxide semiconductors in different temperature regime. Low, medium and high temperature regimes are represented by upper, middle and lower of the figure respectively.[47]

1.4: Introduction of Nanowire Based Sensing

Sensors with one-dimensional (1D) nano-structures have been aroused stimulated considerable interests for scientific, academic and industrial researches because of their specific optical, electrical, magnetic, and mechanical properties owing to their unique structural dimensionality and possible quantum confinement effects. Recently, several efforts are contributed to the sensor fields, such as the utilization of one-dimensional nanostructures (e.g., nanotubes, nanowires, and nanorods) as novel variety gases sensing materials in high temperatures, pressure sensors, PH sensors in carbon capture sequestration, ultra-violet detectors at radiation environments or wireless sensors in all different environments.[35] Taking gas sensor as an example, the confinement effects in nanostructures are anticipated to enhance the three "S" features (sensitivity, selectivity,

and stability) important for sensor technology. Due to their high surface-to-volume ratio, which amplifies the influence of surface states and transduction phenomenon, the gas sensing ability of nano-sensors will be enhanced.[36]

Researchers at Yale University have developed ultrasensitive nano-sensors based on semiconducting nanowires and easy to fabricated. The artist's concept can be used to explain how nanowire-based sensor works which is shown in **Figure 1-8**.[37] With the intrinsic or external decoration on the surface of nanowires, the spotted acceptors which include lots of different colored and functionalized Y-shape projections are designed to bind with certain targeted reactors such as antibodies in human body, metal ions in wasted pollution water, different gases in industrial tunnels or hydrogen ions in acid solution. When the target sources are present in the surrounding, they would connect to corresponding acceptors and cause the conductivity of the nanowire to change. The change in conductivity can create a signal to be detected and analyzed.

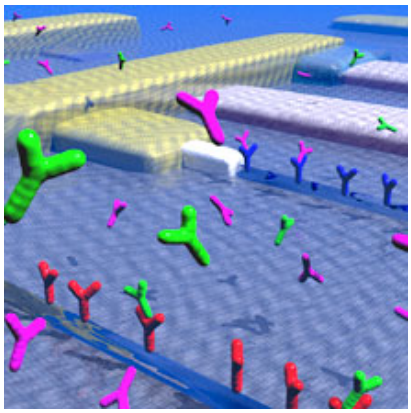

Figure 1-8: A concept of how nanowire-based sensor works and detects specific molecules.[37]

1.4.1: Physical and chemical properties enabled by 1D nanostructures

As compared conventional bulk materials to nanomaterials, due to the high aspect ratios of 1D nanomaterials, large specific surface areas and structural confinement on the nanoscale dimensions, 1D nanomaterials exhibit some unique physical properties and have demonstrated many novel properties in different applications. The nanomaterial possesses some remarkable and specific peculiar properties that may be significantly distinctive from the physical properties of bulk materials Here we briefly review some important results and properties related to the 1D nanostructures.

(I) Color: materials show different colors when they are converted to nanoscale. Take gold as an example shown in **Figure 1-9**, gold nanorods show different color depending on the aspect ratio, which is due to the two intense surface plasmon resonance peaks (longitudinal surface plasmon peak and transverse surface plasmon peak corresponding to the oscillation of the free electrons along and perpendicular to the long axis of the rods). Due to the spherical symmetry, the plasmon oscillation are isotropic in the case of gold nanoshpere; while in the nanorod condition, the oscillation can occur along the width and the length of the nanorod. Therefore, two principle plasmon bands can be tuned referring to different aspect ratio and change the optical properties.[39]

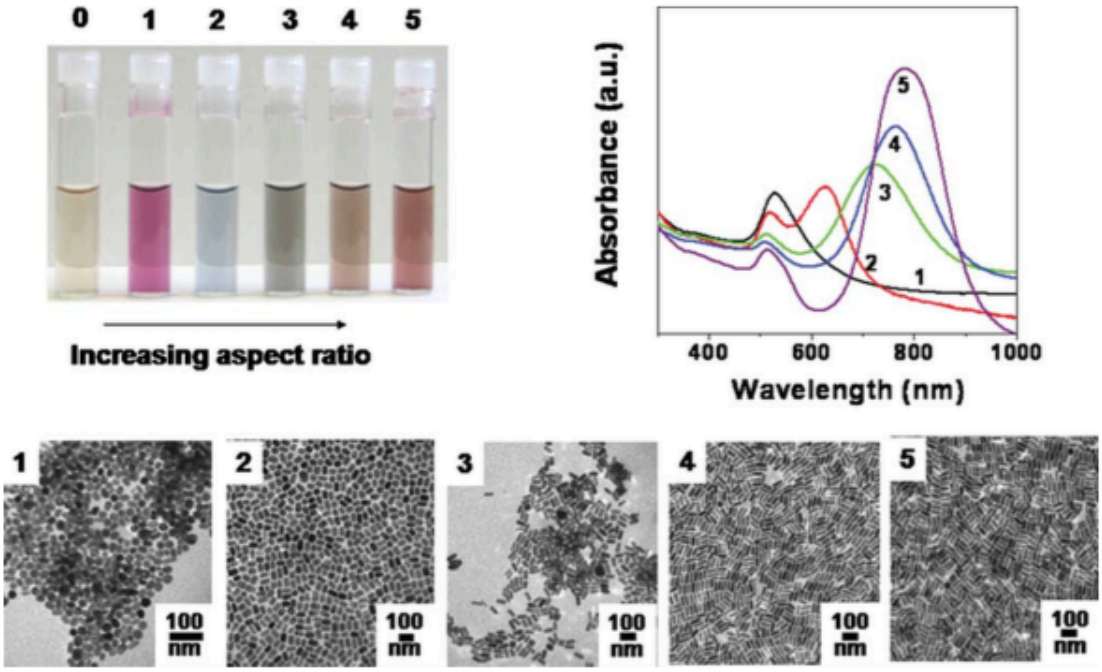

Figure 1-9: Optical properties and spectra of aqueous solutions composed of gold nanoshperes (via 0) and increasing aspect ration to gold nanorods (from 1 to 5) and corresponding transmission electron microscopic images.[39]

(II) Thermal stability and melting point: typically, the melting point of nanosized particles was predicted to be lower than the bulk melting point and was observed by many researches. The reason of melting point changing is because nanoscale materials have much larger surface to volume ratio than bulk materials, drastically altering their thermodynamic and thermal properties.

Shin et al. reported the relationship between the diameter of Sn nanowires and melting behavior. Sn nanowires were fabricated into the anodic aluminum oxide (AAO) template with 7 and 15 nm as the pore diameter shown in **Figure 1-10 (a)** and **(b)** respectively. After DSC test up to 510K, Sn nanowires with radii 7 and 15 nm break into smaller fragments shown in **Figure 1-10 (c)** and **(d)**. **Figure 1-10 (e)** show that depression of the melting point of Sn nanowires increased linearly with the reciprocal radius and nanowires

were fragment after first DSC cycle test. Thus, the nanowire length decreased and caused further depression of the second melting point.[38]

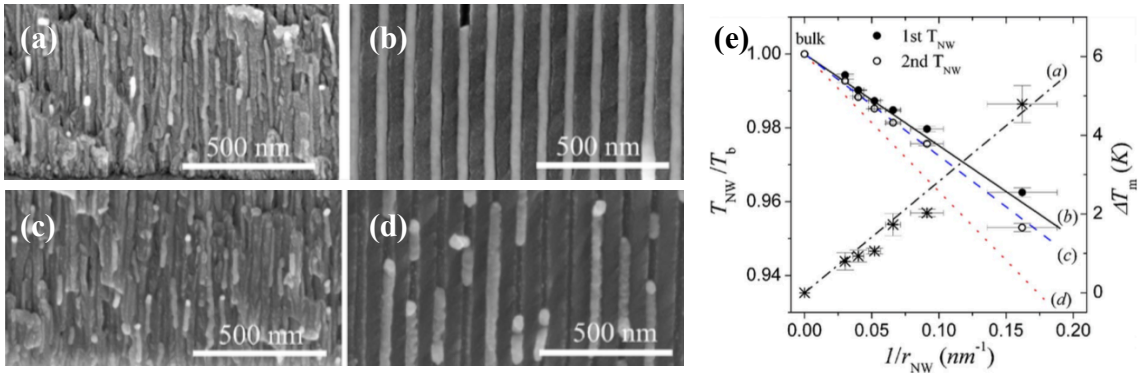

Figure 1-10: Cross-sectional SEM images of as-prepared Sn nanowires with radii of (a) 7 and (b) 15 nm. After first DSC cycle, cross-sectional images of Sn with radii (c) 7, and (d) 15 nm. (e) The first and second melting temperature are normalized and are denoted by solid and open circles, respectively.[38]

Wang et al. fabricated Zn nanowires in the holes of porous anodic aluminum oxide template and investigated the relationship between the melting behavior and the diameters of Zn nanowires. The results also showed that the melting temperature of Zn nanowires depends on the diameter reciprocally.[40]

Therefore, for 1D nanostructured materials, there are some remarkable properties associated with the reduction in melting point as following. It's possible to purify the nanowire and undergo the zone-refining process under a moderate and low temperature compared with the bulk materials. Besides, the 1D nanomaterials may become extremely sensitive to environmental changes as the thickness of nanowires is reduced to nanoscale.

(III) Mechanical properties: the mechanical properties of materials behave qualitatively different as the dimensions are reduced from microscale to nanoscale. On the microscale, the hardness or yield stress of a polycrystalline typically increase with decreasing grain

size, called Hall-Patch effect. This phenomenon can be explained by the mechanism that the area of the grain boundaries increases as the grain size decreases, and thus dislocations will be blocked more efficiently and piled up at the grain boundaries and makes material tougher. However, the phenomenon might become opposite under nanoscale. It's believed that the abnormal behavior was from sliding motion at grain boundaries, i.e. for a polycrystalline, the mechanical strength increases in the first place and then decreases with decreasing grain size. As for 1D nanostructured materials, the mechanical properties usually exhibit stronger than that have larger dimensions and it can be explained by a reduction in the number of defects per unit length.

(IV) Chemical properties: One of the important factors for the chemical applications of nanomaterials is the increment of their surface area that increases the chemical activity of the material. Due to their enhanced chemical activity, nanostructural materials can be used as catalysts to react with such noxious and toxic gases as carbon monoxide and nitrogen oxide in automobile catalytic converters and power generation equipment to prevent environmental pollution arising from burning gasoline and coal.

For example, compared with bulk morphology, ZnO nanowire is a better photocatalyst due to their high surface to volume ratio. Zhou and Wong showed that due to their high purity and crystallinity, ZnO nanowires had a higher catalytic activity than either nanoparticles or bulk ZnO.[44] Additionally, both the effective band gap and redox potential of ZnO will increase if the size of the nanowire is smaller than around 50 nm, and the photogenerated electrons and holes will have a higher reducing/oxidizing power. Besides, one possible way to hinder the recombination of photogenerated electron and

hole would be create a larger band gap, and therefore can improve the charge transfer efficiency between catalyst and the pollutants.

1.4.2: Stability of 1D Nanostructures under Extreme Environment

Future energy technologies will require materials to perform under different extremely harsh environment such as high stress, temperature, pressure, chemical reactivity, photon or radiation conditions. Take coal-fired power plants as an example, it takes about 50% more operating temperature and around twice the operating pressure to achieve the improvement of efficiency from 35% to 60%. Therefore, new materials that can survive under these extremely high thermo and pressure environments must be required. The materials that can withstand thermomechanical extremes, high pressure and stress, strain and strain rate, and high and low temperature, is found across a broad range of energy technologies, such as efficient steam turbines and heat exchangers, fuel-efficient vehicles, and strong wind turbine blades. Aging process in materials will accelerate under the extremely harsh operating environments, and further lead to affect performance and eventually to failure. For example, high temperature not only weakens chemical bonds but also speeds up the chemical reactions of corrosion.

Photons and energetic particles can produce tons of point defects and then merge into larger clusters, which leads to decrease the performance and failure the materials in a short time. Therefore, the ability to prevent the degradation from the energetic particles is a key issue to achieve more efficient energy generation system, such as photovoltaics, solar collectors and nuclear reactors etc.

1.4.3: 1D Nanostructure-Based Sensors for Extreme Environment- A New Dimension of Materials Challenge

Nowadays, basic sensors used for monitoring the operation of the combustion and emission control systems rely on optical techniques. However, most of the optical sensor systems have a temperature dependence that makes them unsuitable for the extreme environments of advanced combustion systems. Advanced fiber optic and optical materials for high-temperature (1300–1650 °C) environments are needed. For control purposes, it would be better to measure real-time composition of combustion gases, and typically the temperature of coal-fired boilers is around 1300 ~ 1650 °C.

On the other hand, the drawback of steam-plant materials is corrosion and it's strongly influenced by the pH of the hot circulating water. However, pH sensor materials will be degraded by hot water, thus fabrication of pH sensor that can sustain at high temperature, high corrosive circumstance is a current challenge. Lvov and Palmer (2004) summarize a variety of high-temperature pH and electrochemical measurement and monitoring approaches attractive for application in a broad range of energy applications.

1.5: Motivation and Background of the Research

Practically, most high temperature gas sensing technologies are based on indirect or non-contact methods such as calorimetery, chromatography, and spectroscopic methods such as laser diode based spectroscopy, which is still in testing stage after more than two decades development. For Calorimetry, by measuring calorific value and density of the gases, the gas species can be determined. As for Chromatography, through gas chromatography, the mixing gases can be separated and identified. But these facilities are

usually too expensive or too cumbersome for measurements in industrial environments. In addition, they are usually lack of spatial and temporal resolutions due to the intrinsic indirect and non-contract methodologies with probes far away from the detected locations and regions.

To allow *in-situ* and real-time measurement, solid state gas sensors are another technology candidate of the choice for sensing and control in power generation and automotive industries. The clear merits of the solid state sensors come from the ease of fabrication, simple enough configurations, comparatively cheap, and the miniaturizing ability through traditional microfabrication technology. In the past decades, various solid state sensors have been developed for monitoring combustion process.[23, 46, 47]Among those, resistor-type and solid electrolyte based potentiometric gas sensors have been extensively studied for high temperature environment. High-temperature sensors for *in-situ* and real-time combustion environment monitoring are often based on electronic, ionic, or mixed ionic-electronic conductors. Pure ionic conductors are used in potentiometric, mixed-potential or amperometric sensors, but electronic and mixed (ionic–electronic) conductors are used in resistor-type sensors.

1.5.1: High Temperature Solid State Resistive Type Sensor

In the resistor-type sensors, the surface adsorption and desorption of the target gases on the sensing materials are normally detected through the induced surface and bulk electronic or electronic-ionic transport property changes. The most commonly used semiconductor metal oxides include SnO_2, TiO_2, and ZnO, which could handle the temperature range up to 500 °C. Recently, the emerging semiconductor metal oxides

including CeO_2, Ga_2O_3, NiO, $LaFeO_3$, $SrFeO_3$, $SrTiO_3$ have promised as new resistor-type sensor materials potentially useful in a higher temperature region of 500-1200 °C. However, with most of them being sensitive to the reducing gases including H_2, CO, CH_4 etc., the cross-sensitivity is an issue leading to the selectivity problems. Recently, mesoporous metal oxide catalytic filters using Ga_2O_3, SiO_2 and $AlVO_4$ have been studied and suggested to be an efficient window to screen out the non-specific bindings for better gaseous specificity.

On the other hand, the latest development of sensors for combustion relevant gas detection has shifted toward optical sensors directly using photon-matter interactions such as luminescence, optical spectrum (absorption/reflection/transmission), or electro-activated mechanical sensors (e.g., surface acoustic wave), which allow the remote monitoring and wireless detection of gas species in various advanced power systems ranging from combustion engines to coal-fired power plants. Optical method based sensors present an interesting and potentially viable solution to avoid the challenge of making reliable electrical contacts on sensing elements such as nanomaterials in order to fabricate electrical or electrochemical sensors.

Despite the booming research on using SAW and fiber optical sensors for wireless and remote sensing application in harsh environments, several other important optical methods such as photocurrent and photoluminescence have been largely neglected as means for real time gas detection.[54] In fact, these optical sensing modes can easily prevail over the other methods with some outstanding merits. For example, in the case of photocurrent, the sensing response time could be as short as a fraction of second and the selectivity could be very high given the photocurrent can be very distinctly varied upon

different chemical species introduction upon UV illumination.[53] A photodetector based on gallium nitride (GaN) and an UV arc discharge lamp are integrated (**Figure 1-11**) to form an auto-combustion exhaust gas sensor.[54] The arc discharge lamp induces electronic transitions in the gas molecules flowing between the light source and the GaN photodetector. These transitions modify the fraction of light in the UV spectral region which is detected by the GaN photodetector, as a function of the exhaust gas concentration.

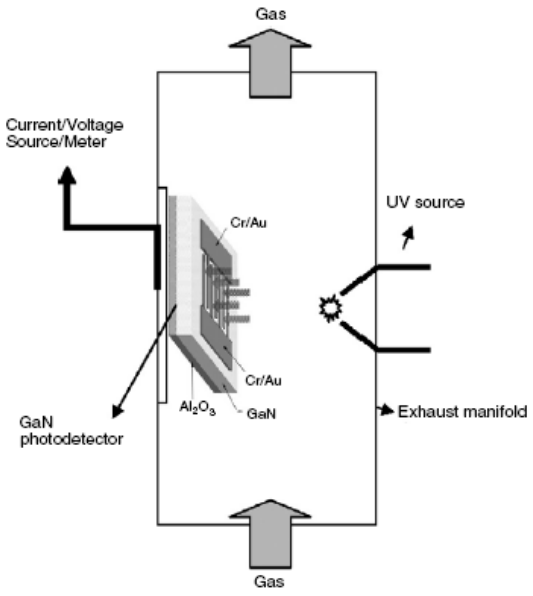

Figure 1-11: A schematic setup of GaN based UV photodetector based gas sensor for auoto-exhaust such as NO_x and CO at temperature up to 550 °C.[54]

1.5.2: β-Ga_2O_3 Properties and Based Solid State Gas Sensor

The basic information of β–Ga_2O_3, such as structure or electric properties, will be introduced in this section. Ga_2O_3 is a polymorphism material that can be presented in several different phases, including α–($R\bar{3}m$, a=4.979Å and c= 13.429Å), β–($C\frac{2}{m}$, a=12.23Å, b=3.04Å, c=5.80Å and β=103.7°), γ–Ga_2O_3($Fd\bar{3}m$, a=8.22Å)[57, 58] β–Ga_2O_3 is

the most stable phase of all those phases and it's an important functional material as being an insulating barrier for spin-dependent tunneling junction,[56] electroluminescence phosphor,[57,58] sensor,[59, 60] coating in solar cells,[61,62] power electronic devices, deep-ultraviolet transparent conductive oxide or photodiodes,[63] etc. **Figure 1-12** shows the unit cell of β–Ga_2O_3 and it's the base-centered monoclinic structure with 20 atoms per unit cell. β–Ga_2O_3 possesses two inequivalent Ga sites: Ga(I), Ga(II) and three inequivalent O-sites: O(I), O(II) and O(III). The Ga(I) sites have tetrahedral coordination, and the Ga(II) sites have octahedral coordination.[65]

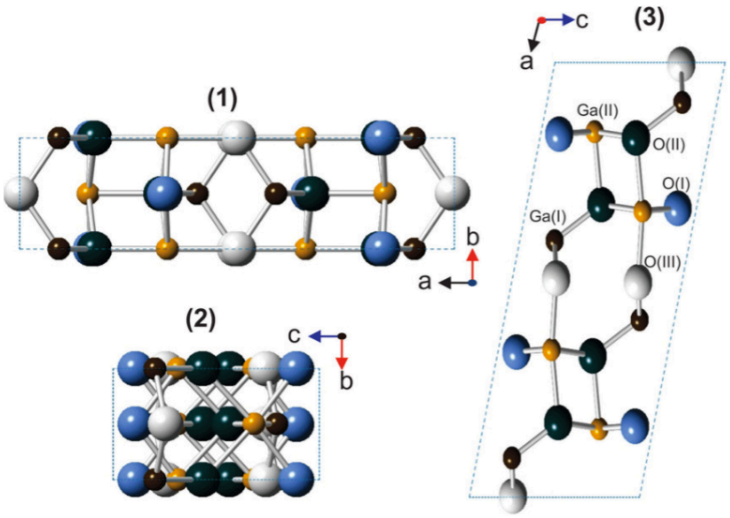

Figure 1-12: Unit cell of β-Ga_2O_3 and the projection of the unit cell of β-Ga_2O_3 along the c-, a- and b-axis is depicted in (1), (2) respectively.[65]

A wide band gap semiconductor (~4.9 eV), β–Ga_2O_3 has been intensively studied lately as a new candidate material for high temperature gas sensors. Fleischer and Meixner studied an oxygen sensor based on a sputtered Ga_2O_3 thin film that could be applied at temperatures over 500 °C. This type of thin film sensor was also sensitive to reducing gases such as hydrogen. However, the thin film configured sensor has a

relatively low stability at high temperature due to the severer sintering effect that can degrade the sensing film integrity and functions. On the other hand, the sensor device signal response such as current could be low due to intrinsically low specific surface area exposed to gaseous analytes.

Besides the thin film form devices, nanowire based β-Ga_2O_3 photodetector and field-effect transistors have been demonstrated. With a large surface-to-volume ratio, nanowire-based gas sensors were demonstrated to provide a much larger sensitivity than thin film-based gas sensors.[60] Sensing properties of β-Ga_2O_3 thin film on O_2, CO and H_2 gas have been reported at a temperature range of 600-1000 °C.[47, 50, 67]

In addition, β-Ga_2O_3 nanowires are reported to be able to detect volatile organic compounds (VOCs) such as acetone, nitromethane and triethylamine. Lately, β-Ga_2O_3 has been tapped as a promising ultrahigh temperature sensing material due to its high thermal stability that can allow its safe operation at temperatures up to 1000 °C. However, in terms of detection of NO_2 and CO, there are few reports about β-Ga_2O_3 test at high temperature above 500 °C.

In terms of gas sensor performance, sensitivity is one of the most important figures of merit that also include selectivity and stability. The sensitivity of a resistor-type metal oxide semiconductor sensor is determined by measuring the change of resistance or current when target gas molecules interact with the sensor surface. However, resistor-type gas sensor tends to show lower sensitivity in high temperature due to the usually unfavorable surface chemistry at high temperature. Therefore, the sensor materials selection and architecture design are very critical in order to achieve sensors with high sensitivity at high temperatures such as 800 °C.

1.5.3: Perovskite Based High Temperature Materials

Perovskite based oxides have drawn much attention due to their potential applications as sensors, solid electrolytes, oxygen ion and proton conductors, fuel cells, and hydrogen membranes. The ABO_3 perovskite structures can display various types of transport properties ranging from ionic conduction to electronic conduction, which are respectively suitable for potentiometric and resistor-type gas sensors.[69-73]

Perovskite oxides are particularly attractive for high-temperature applications due to three-fold reasons. First, high melting and/or decomposition temperatures; second, high structural stability to improve reliability and long-term sensor performance; third, in ABO_3 perovskite structures, a number of A-site and B-site cations can be accommodated, giving the ABO_3 system flexible doping ability in terms of controlling the transport and catalytic properties to optimize sensor performance. In this work, we adopt two types of La-based perovskite nanoparticles as the modification layer on top of the b-Ga_2O_3 nanowire arrays, i.e., (La, Sr)CoO_3 (LSCO), (La, Sr)FeO_3 (LSFO), and (La, Sr)MnO_3 (LSMO). These selective perovskite nanoparticles have proved to enhance the overcoated nanowire sensors toward high stability, sensitivity and selectivity.

1.6: Dissertation Objectives

In this work, three objectives are pursued to:

(1) Design and synthesize β-Ga_2O_3 based (i.e., β-Ga_2O_3, β-Ga_2O_3/LSCO, β-Ga_2O_3/LSFO) nanorod array on Si substrate using a hydrothermal method and radio frequency sputtering method, in conjunction with post thermal annealing and H_2 treatment, also equipped with ultraviolet light source to illuminate the sensor device;

(2) Characterize the structure and morphology of β-Ga_2O_3 based nanorod array using various electron microscopy (SEM, TEM, etc.) and spectroscopy (EDS) tools;

(3) Investigate the gas sensing performance of β-Ga_2O_3 based nanorod array under oxidizing atmosphere (e.g. O_2, NO_2) and reducing atmosphere (e.g. CO and H_2) and understand the sensing mechanisms.

Reference

1. Wilson, D. M.; Hoyt, S.; Janata, J.; Booksh, K.; Obando, L., Chemical Sensors for Portable Handheld Field Instruments. *IEEE Sens. J.* 2001, 1, 256-274.
2. Burrell, G. A., The Composition of Some Mine Gases and a Description of a Simple Methane Apparatus. *J. Ind. Eng. Chem.* 1912, 4, 96-100.
3. Burrell, G. A., Notes on Mine Gas Problems. *J. Ind. Eng. Chem.* 1913, 5, 181-186.
4. Rooney, R. P., Humphry Davy: The romantic chemist. *J. Chem. Educ.* 1986, 63, 739-740.
5. Chiang, Y.-J.; Pan, F.-M., PdO Nanoflake Thin Films for CO Gas Sensing at Low Temperatures. *J. Phys. Chem. C* 2013, 117, 15593-15601.
6. Gerblinger, J. L., W.; Lampe, U.; Meixner, H., High Temperature Oxygen Sensor Based on Sputtered Cerium Oxide. *Sens. Actuators, B* 1995, 26, 93-96.
7. Hjiri, M.; El Mir, L.; Leonardi, S. G.; Pistone, A.; Mavilia, L.; Neri, G., Al-Doped ZnO for Highly Sensitive CO Gas Sensors. *Sens. Actuators, B* 2014, 196, 413-420.
8. Moos, R.; Izu, N.; Rettig, F.; Reiss, S.; Shin, W.; Matsubara, I., Resistive Oxygen Gas Sensors for Harsh Environments. *Sensors* 2011, 11, 3439.
9. Khodakarami, J.; Ghobadi, P., Urban Pollution and Solar Radiation Impacts. *Renewable Sustainable Energy Rev.* 2016, 57, 965-976.
10. Gönüllü, Y.; Haidry, A. A.; Saruhan, B., Nanotubular Cr-Doped TiO_2 for Use as High-Temperature NO_2 Gas Sensor. *Sens. Actuators, B* 2015, 217, 78-87.
11. Kumar, A.; Kim, H.; Hancke, G. P., Environmental Monitoring Systems : A Review. *IEEE Sens. J.* 2013, 13, 1329-1339.
12. Sun, Y. F.; Liu, S. B.; Meng, F. L.; Liu, J. Y.; Jin, Z.; Kong, L. T.; Liu, J. H., Metal Oxide Nanostructures and Their Gas Sensing Properties: A Review. *Sensors* 2012, 12, 2610-2631.
13. Wang, C.; Yin, L.; Zhang, L.; Xiang, D.; Gao, R., Metal Oxide Gas Sensors: Sensitivity and Influencing Factors. *Sensors* 2010, 10, 2088-2106.
14. Huang, J.; Wan, Q., Gas Sensors Based on Semiconducting Metal Oxide One-Dimensional Nanostructures. *Sensors* 2009, 9, 9903-9924.
15. Schweizer-Berberich, M.; Strathmann, S.; Go¨pel, W.; Shrma, R.; Peyre-Lavigne, A., Filters for Tin Dioxide CO Gas Sensors to Pass The Ul2034 Standard. *Sens. Actuators, B* 2000, 66, 34-36.

16. Zakrzewski, J.; Domanski, W.; Chaitas, P.; Laopoulos, T., Improving Sensitivity and Selectivity of SnO_2 Gas Sensors by Temperature Variation. *IEEE Trans. Instrum. Meas.* 2006, 55, 14-20.
17. Chiu, S.-W.; Tang, K.-T., Towards a Chemiresistive Sensor-Integrated Electronic Nose: A Review. *Sensors* 2013, 13, 14214-47.
18. Sysoev, V. V.; Goschnick, J.; Schneider, T.; Strelcov, E.; Kolmakov, A., A Gradient Microarray Electronic Nose Based on Percolating SnO_2 Nanowire Sensing Elements. *Nano Lett.* 2007, 7, 3182-3188.
19. Fergus, J. W., Materials for High Temperature Electrochemical NO_x Gas Sensors. *Sens. Actuators, B* 2007, 121, 652.
20. Szabo, N.; Lee, C.; Trimboli, J.; Figueroa, O.; Ramamoorthy, R., Ceramic-Based Chemical Sensors, Probes and Field-Tests in Automobile Engines. *J. Mater. Sci.* 2003, 38, 4239-4245.
21. Akbar, S.; Dutta, P.; Lee, C., High-Temperature Ceramic Gas Sensors: A Review. *Int. J. Appl. Ceram. Technol.* 2006, 3, 302.
22. Jamison, K.; Eisenhauer, J.; Rash, J.; Greenman, M.; Levine, E., Glass Industry Technology Roadmap. *DOE Report* 2002.
23. Bene, R. P., Z.; Perczel, I.V.; Fleischer, M.; Reti, F., High-Temperature Semiconductor Gas Sensors. *Vacuum* 2001, 61, 275-278.
24. Tuller, H. L., Materials for High Temperature Electrochemical Applications-Automotive Sensors, Catalysts and Traps. *The 14th International Meeting on Chemical Sensors* 2012.
25. Lin, H.-J. G., H.Y.; Gao, P.X., Nanowire Based Sensors for Extreme Environment 2016.
26. Gao, P. X.; Shimpi, P.; Liu, C. H.; Guo, Y. B.; Cai, W. J.; Liao, K.-T.; Wrobel, G.; Zhang, Z. H.; Ren, Z.; Lin, H.-J., Multifunctional Composite Nanostructures for Energy and Environmental Application. *Int. J. Mol. Sci.* 2012, 13, 7393-7423.
27. Bogue, R., Sensors for extreme environments. *Sensor Review* 2012, 32, 267-272.
28. Tuller, H. L., Ionic Conduction in Nanocrystalline Materials. *Solid State Ionics* 2000, 131, 143-157.
29. Fergus, J. W., Sensing Mechanism of Non-Equilibrium Solid-Electrolyte-Based Chemical Sensors. *J. Solid State Electrochem.* 2010, 15, 971-984.
30. Pasierb, P.; Rekas, M., Solid-State Potentiometric Gas Sensors—Current Status and Future Trends. *J. Solid State Electrochem.* 2008, 13, 3-25.
31. Matsumoto, H.; Kuribayashi, M.; Katahira, K.; Iwahara, H., Double-Cell Carbon Dioxide Sensor Based on Li-K Molten Carbonate with Electrochemically-Supplied CO_2-O_2 Reference. *Sens. Actuators, B* 2001, 73, 157-162.
32. Miura, N.; Sato, T.; Anggraini, S. A.; Ikeda, H.; Zhuiykov, S., A Review of Mixed-Potential Type Zirconia-Based Gas Sensors. *Ionics* 2014, 20, 901-925.
33. Jasinski, P., Solid-State Electrochemical Gas Sensor. *Mater. Sci.-Pol.* 2006, 2, 269-278.
34. Xu, S.; Wang, Z. L., One-Dimensional ZnO Nanostructures: Solution Growth and Functional Properties. *Nano Res.* 2011, 4, 1013-1098.
35. Hamelers, H. V. M.; Schaetzle, O.; Paz-García, J. M.; Biesheuvel, P. M.; Buisman, C. J. N., Harvesting Energy from CO_2 Emissions. *Environ. Sci. Technol. Lett.* 2014, 1, 31-35.

36. Ramgir, N. S.; Yang, Y.; Zacharias, M., Nanowire-Based Sensors. *Small* 2010, 6, 1705-1722.
37. Bullis, K., Easy-to-Make Nanosensors *MIT Technology Review* 2007.
38. Shin, H. S.; Yu, J.; Song, J. Y., Size-Dependent Thermal Instability and Melting Behavior of Sn Nanowires. *Appl. Phys. Lett.* 2007, 91, 173106-3.
39. Murphy, C. J.; Gole, A. M.; Hunyadi, S. E.; Stone, J. W.; Sisco, P. N.; Alkilany, A.; Kinard, B. E.; Hankins, P., Chemical Sensing and Imaging with Metallic Nanorods. *Chem. Commun.* 2008, 544-57.
40. Wang, X. W.; Fei, G. T.; Zheng, K.; Jin, Z.; De Zhang, L., Size-Dependent Melting Behavior of Zn Nanowire Arrays. *Appl. Phys. Lett.* 2006, 88, 173114-3.
41. Wu, B.; Heidelberg, A.; Boland, J. J., Mechanical Properties of Ultrahigh-Strength Gold Nanowires. *Nat. Mater.* 2005, 4, 525-529.
42. Wang, J.; Chen, X.; Wang, G.; Wang, B.; Lu, W.; Zhao, J., Melting Behavior in Ultrathin Metallic Nanowires. *Phys. Rev. B* 2002, 66, 085408.
43. Wang, Z. L.; Gao, R. P.; Pan, Z. W.; Dai, Z. R., Nano-Scale Mechanics of Nanotubes, Nanowires, and Nanobelts. *Adv. Funct. Mater.* 2001, 3, 657-661.
44. Zhou, H.; Wong, S. S., A Facile and Mild Synthesis of 1-D ZnO, CuO, and Alpha-Fe_2O_3 Nanostructures and Nanostructured Arrays. *ACS Nano* 2008, 2, 944-958.
45. Zhang, P.; Lee, C.; Verweij, H.; Akbar, S. A.; Hunter, G.; Dutta, P. K., High Temperature Sensor Array for Simultaneous Determination of O_2, CO, and CO_2 with Kernel Ridge Regression Data Analysis. *Sens. Actuators, B* 2007, 123, 950-963.
46. Fergus, J. W., Perovskite Oxides for Semiconductor-Based Gas Sensors. *Sens. Actuators, B* 2007, 123, 1169.
47. Fleischer, M., Advances in Application Potential of Adsorptive-Type Solid State Gas Sensors: High-Temperature Semiconducting Oxides and Ambient Temperature Gasfet Devices. *Meas. Sci. Technol.* 2008, 19, 042001.
48. Fleischer, M. M., H., Selectivity in High-Temperature Operated Semiconductor Gas-Sensors. *Sens. Actuators, B* 1998, 52, 179-187.
49. Fleischer, M.; Kornely, S.; Weh, T.; Frank, J.; Meixner, H., Selective Gas Detection with High-Temperature Operated Metal Oxides Using Catalytic Filters. *Sens. Actuators, B* 2000, 69, 205-210.
50. Fleischer, M. S., M.; Kohl, C.-D.; Mexiner, H., A Study of Surface Modification at Semiconducting Ga_2O_3 Thin Film Sensors for Enhancement of the Sensitivity and Selectivity *Sens. Actuators, B* 1996, 36, 290-296.
51. Leyer, B. S., H.; Gobel, H.; Meixner, H.; Scherg, T.; Knozinger, H., Preparation of $AlVO_4$-Films for Sensor Application via A Sol-Gel/Spin-Coating Technique. *Thin Solid Films* 1997, 310, 228-233.
52. Lin, H.-J. G., P.X., UV-Enhanced CO Sensing Using Ga_2O_3-Based Nanorod Array at Elevated Temperature. 2016.
53. Zhou, J.; Gu, Y.; Hu, Y.; Mai, W.; Yeh, P. H.; Bao, G.; Sood, A. K.; Polla, D. L.; Wang, Z. L., Gigantic Enhancement in Response and Reset Time of ZnO UV Nanosensor by Utilizing Schottky Contact and Surface Functionalization. *Appl. Phys. Lett.* 2009, 94, 191103.
54. Mello, M.; Potì, B.; Risi, A. d.; Passaseo, A.; Lomascolo, M.; Vittorio, M. D., GaN Optical System for CO and NO Gas Detection in the Exhaust Manifold of Combustion Engines. *J. Opt. A: Pure Appl. Opt.* 2006, 8, S545.

55. Dai, Z. R.; Pan, Z. W.; Wang, Z. L., Gallium Oxide Nanoribbons and Nanosheets. *J. Phys. Chem. B* 2002, 106, 902-904.
56. Li, Z.; Groot, C. d.; Hoodera, J. H., Gallium Oxide as An Insulating Barrier for Spin-Dependent Tunneling Junctions. *Appl. Phys. Lett.* 2000, 77, 3630-3632.
57. López, I.; Utrilla, A. D.; Nogales, E.; Méndez, B.; Piqueras, J.; Peche, A.; Ramírez-Castellanos, J.; González-Calbet, J. M., In-Doped Gallium Oxide Micro- and Nanostructures: Morphology, Structure, and Luminescence Properties. *J. Phys. Chem. C* 2012, 116, 3935-3943.
58. Wu, X. C.; Song, W. H.; Huang, W. D.; Pu, M. H.; Zhao, B.; Sun, Y. P.; Du, J. J., Crystalline Gallium Oxide Nanowires: Intensive Blue Light Emitters. *Chem. Phys. Lett.* 2000, 328, 5-9.
59. Kim, H.; Jin, C.; An, S.; Lee, C., Fabrication and CO Gas-Sensing Properties of Pt-Functionalized Ga_2O_3 Nanowires. *Ceram. Int.* 2012, 38, 3563-3567.
60. Liu, Z.; Yamazaki, T.; Shen, Y.; Kikuta, T.; Nakatani, N.; Li, Y., O_2 and CO Sensing of Ga_2O_3 Multiple Nanowire Gas Sensors. *Sens. Actuators, B* 2008, 129, 666-670.
61. Minami, T.; Nishi, Y.; Miyata, T., High-Efficiency Cu_2O-Based Heterojunction Solar Cells Fabricated Using a Ga_2O_3 Thin Film as N-Type Layer. *Appl. Phys. Express* 2013, 6, 044101-4.
62. Shin, T. I.; Lee, H. J.; Song, W. Y.; Kim, S.-W.; Park, M. H.; Yang, C. W.; Yoon, D. H., A Homojunction of Single-Crystalline β-Ga_2O_3 Nanowires and Nanocrystals. *Nanotechnology* 2007, 18, 345305.
63. Orita, M.; Ohta, H.; Hirano, M.; Hosono, H., Deep-Ultraviolet Transparent Conductive β-Ga_2O_3 Thin Films. *Appl. Phys. Lett.* 2000, 77, 4166-4168.
64. Li, Y.; Tokizono, T.; Liao, M.; Zhong, M.; Koide, Y.; Yamada, I.; Delaunay, J.-J., Efficient Assembly of Bridged β-Ga2O3 Nanowires for Solar-Blind Photodetection. *Adv. Funct. Mater.* 2010, 20, 3972-3978.
65. Janowitz, C.; Scherer, V.; Mohamed, M.; Krapf, A.; Dwelk, H.; Manzke, R.; Galazka, Z.; Uecker, R.; Irmscher, K.; Fornari, R.; Michling, M.; Schmeißer, D.; Weber, J. R.; Varley, J. B.; Walle, C. G. V. d., Experimental Electronic Structure of $In_2O_3$and Ga_2O_3. *New J. Phys.* 2011, 13, 085014.
66. Fleischer, M. H., L.; Born, E.; Meixner, H., Evidence for a Phase Transition of β-Gallium Oxide at Very Low Oxygen Pressures. *J. Am. Ceram. Soc.* 1997, 80, 2121-2125.
67. Fleischer, M.; Meixner, H., Thin-Film Gas Sensors Based on High-Temperature-Operated Metal Oxides. *J. Vac. Sci. Technol., A* 1999, 17, 1866-1872.
68. Arafat, M. M.; Dinan, B.; Akbar, S. A.; Haseeb, A. S., Gas Sensors Based on One Dimensional Nanostructured Metal-Oxides: A Review. *Sensors* 2012, 12, 7207-58.
69. Huang, K.; Lee, H. Y.; Goodenough, J. B., Sr- and Ni-Doped $LaCoO_3$ and $LaFeO_3$ Perovskites: New Cathod Materials for Solid-Oxide Feul Cells. *J. Electrochem. Soc.* 1998, 145, 3220-3227.
70. Lin, H.-J. G., H.Y.; Gao, P.X., Perovskite Nanoparticle Sensitized Ga_2O_3 Nanorod Arrays For Highly Selective NO_2 Detection Over O_2 At 800°C 2016.
71. Lin, H.-J.; Baltrus, J. P.; Gao, H.; Ding, Y.; Nam, C.-Y.; Ohodnicki, P.; Gao, P.-X., Perovskite Nanoparticle-Sensitized Ga_2O_3 Nanorod Arrays for CO Detection at High Temperature. *ACS Appl. Mater. Interfaces* 2016, 8, 8880-8887.

72. Fan, K.; Qin, H.; Wang, L.; Ju, L.; Hu, J., CO_2 Gas Sensors Based on $La_{1-x}Sr_xFeO_3$ Nanocrystalline Powders. *Sens. Actuators, B* 2013, 177, 265-269.
73. Thirumalairajan, S.; Girija, K.; Mastelaro, V. R.; Ponpandian, N., Surface Morphology-Dependent Room-Temperature $LaFeO_3$ Nanostructure Thin Films as Selective NO_2 Gas Sensor Prepared by Radio Frequency Magnetron Sputtering. *ACS Appl. Mater. Interfaces* 2014, 6, 13917-13927.

CHAPTER 2

Experiment and Characterization Techniques

Nanostructured materials have become one of the hottest topics across multiple research fields in the last two decades as being the fundamental knowledge of nano-science and it has also triggered much interest in fundamental and industrial researches. Normally, nanostructures are defined as the structures with at least one dimension less than 100 nm. Under the nano-scale dimension, the properties of nanostructures are different from those of bulk parts even though they have the same chemical compositions. In nanostructured materials, quantum confinement effect plays an important role in every aspect of properties. With the combination of quantum effects and multi-body interaction, nanostructured materials may possess novel mechanical, electrical, optical, and chemical properties.[3-5]

Here in this thesis work, we successfully synthesized large scale β-Ga_2O_3 nanorod arrays (NRAs) on Si substrates using a cost-effective hydrothermal deposition process followed by high temperature annealing. Based on these 3-D β-Ga_2O_3 NRAs, we design and investigate three material and sensor design strategies in order to improve the new sensor materials architecture and sensing mechanism.

In this chapter, the detail of experimental set-up, structure and property characterizations techniques will be discussed in the following subsections.

2.1: Experimental Set-up

In the aspect of material synthesis, hydrothermal synthesis and radio-frequency (RF) magnetron sputtering are two most frequently used methods in this dissertation. In order to fabricate 3-D nanorod array structures, a thin seed layer via RF magnetron sputtering is necessary before hydrothermal growth.

Here we introduce the precursor chemicals in the first place, followed by the introduction of fabrication methods, i.e. hydrothermal synthesis and RF magnetron sputtering.

2.1.1: Precursor, Substrate and Sputtering Target Chemicals

(I) Gallium(III) nitrate hydrate ($Ga(NO_3)_3 \cdot 9H_2O$, 99.9998%): the gallium salt of nitric acid with molecular weight 417.88 was purchased from Acros Organics. It is a white, slightly hygroscopic and crystal powder with good solubility in water. It is used as the precursor of hydrothermal synthesis in this work.

(II) Tin dioxide (SnO_2, >99.9%): the inorganic compound target with diameter 2" and 0.25" in thickness was purchased from Stanford Advanced Materials. The white circular target with molecular weight 150.71 was used as the seed layer for further hydrothermal synthesis.

(III) Lanthanum Strontium Cobalt Oxide ($La_{0.8}Sr_{0.2}CoO_3$, >99.9%): the odorless black target is insoluble in water. It's ordered from Broker. It's used as the surface modification via RF magnetron sputter technique.

(IV) Lanthanum Strontium Ferrite Oxide ($La_{0.8}Sr_{0.2}FeO_3$, >99.9%): the odorless black target was ordered from Broker.

(V) Chloroplatinic acid (H_2PtCl_6): the reddish brown solid is highly soluble in water. It's used as the precursor for platinum (Pt) nanoparticles.

(VI) Silicon (Si, (100)): substrates (boron doped, p-type, 1~10 ohm-cm, 100 mm in diameters, 500 mm in thickness, single flat, single side polish) topped with 1mm silicon dioxide (SiO_2) were purchased from University Wafer.

(VII) Deionized Water (DI Water): it's used as solvent for hydrothermal method and to clean the sample after the growth process.

2.1.2: Hydrothermal Synthesis

Through the whole dissertation work, hydrothermal method is extensively used to prepared 3-D aligned nanorod arrays on Si substrates. Hydrothermal synthesis is a method to fabricate single crystals that depends on the solubility in hot water and high pressure. The apparatus that can perform hydrothermal methods is usually named autoclave which usually consists of inner and outside parts. On the outside parts, there're thick-walled stainless steel cylinders which can withstand high temperature and high pressure for prolong period of time. In the inner parts, the vessel is put in the middle of the autoclave and must be inert material with respect to different solvents, however, the vessels are made of Teflon in our lab. The cross-section view of the autoclave is shown in **Figure 2-1**. It is worth to mention that there're stainless steel glands between the stainless steel kettle and Teflon vessel and the whole autoclave should close tightly before hydrothermal synthesis. In addition, the substrates should be stocked into the Teflon bar holder and keep seed layer upside down.

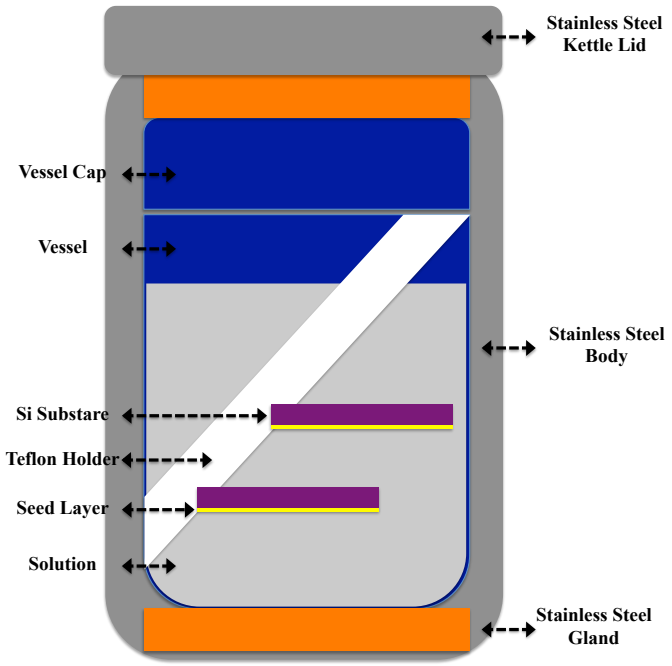

Figure 2-1: Schematic diagram of autoclave set-up for the growth GaOOH nanorod arrays on Si substrates.

2.1.3: Radio-Frequency Magnetron Sputtering

Magnetron sputter is one kind of physical vapor deposition processes that can eject materials out of the target source to deposit on. The basic component of magnetron sputtering system is shown in **Figure 2-2**. The target (Pt, SnO_2, LSFO or LSCO, ect.) and the substrates should be placed into the chamber in the first place, followed by turning on the mechanical (rotary) pump for 10 to 20 minutes untill the pressure of the chamber reaches ~$1x10^{-1}$ torrs. Then turbomolecular pump is turn on although it can be operated under atmosphere, it would be better to turn on at low pressure in order to avoid some big dust to hit the blades of the turbomolecular pump. Waiting for another 30 to 40 minutes, the pressure of the chamber would down to $5x10^{-5}$ torr. A controlled flow of an inert gas, Ar, is introduced at 20 standard cubic centimeters per minute (sccm) and the pressure of vacuum chamber raises to 10^{-2} to 10^{-3} torr. With the high electromagnetic fields, the Ar

molecule will be ionized and create plasma which contains electrons, positive and negative particles. In addition, the first ionized Ar molecule will generate one electron and then it would speed up to hit another Ar molecule to create more Ar^+ and e^-, more and more electrons and Ar^+ ions will be present immediately, called electron avalanche effect.

A negative voltage attracts positive ions (Ar^+) will hit to the target surface with speed and energy. Surface atoms become sputtered and though transportation in high vacuum, the sputtered matters will reach and deposit on top of the substrates in high vacuum.[1, 6, 7] However, due to the conductivity issue, if the target is semiconductor or insulator, the bombarded Ar^+ ion will neutralize the potential with the negative electrode and less Ar^+ ions will be attracted to the negative electrode and decrease the sputtering efficiency. Therefore, radio-frequency electron gun is needed, the positive or negative voltage will applied on the electron gun alternately and attract e^- or Ar^+, respectively. Hence, RF apparatus would keep the electrode with appropriate negative potential, attract Ar^+ ions to bombard the target and keep semiconductor or insulator target sputter with good sputtering rate.

Besides, since the turbomolecular pump and electron gun will generate lots of heat, therefore, chilling water should be keep it running through the whole sputter process. After sputtering, the chamber should be kept in low vacuum after taking out the sample and therefore, avoiding water molecules or dust attach on the inner wall of the chamber. And it should be paid attention that the sequence of turning on valve. The rotary pump should be turn on first and then open the valve later in order to avoid back stream of oil which is used in the rotary pump due to the pressure difference between chamber and the atmosphere.

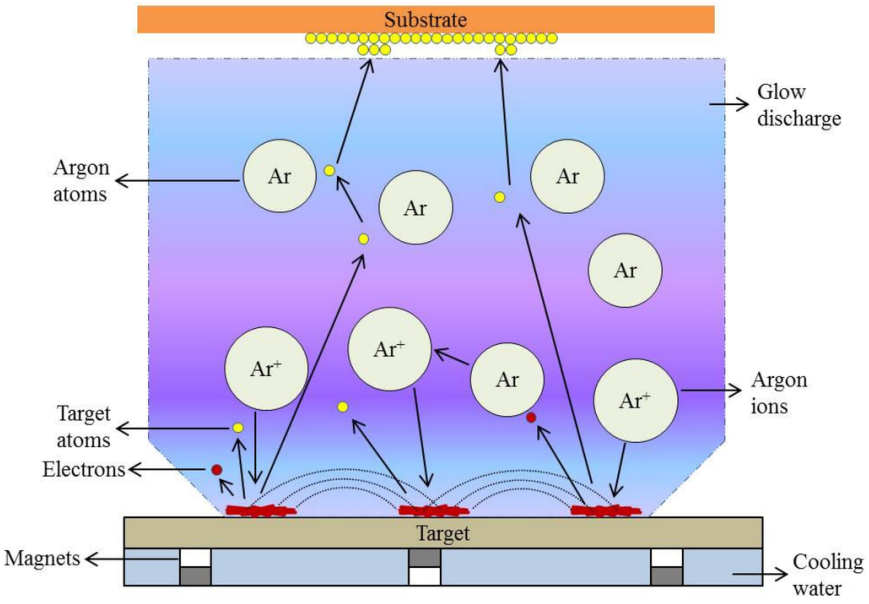

Figure 2-2: Schematic diagram illustrating the basic components of a magnetron sputtering system.[1]

2.2: Structure Characterization

In this section, methods used to characterize the materials and understand the basic crystal structures and chemical composition will be discussed.

2.2.1: X-Ray Diffraction

X-ray diffraction (XRD) is a common tool used to determine and identify the crystal structure of a material. See things from atoms' points of view, crystals are made of arrays of atoms, and X-rays can be considered as electromagnetic waves. Atoms and atoms' electrons would scatter X-ray waves. The scattered waves in a few specific directions would add constructively, i.e. the path length between the scattered X-ray from different (hkl) is an integer times the wavelength, those planes can be determined by Bragg's Law:

$$2d_{hkl} \sin\theta = n\lambda$$

where d_{hkl} is the spacing between diffracting planes, θ is the incident angle, n is any integer and λ is the wavelength of the incident beam, shown in **Figure 2-3**.[2]

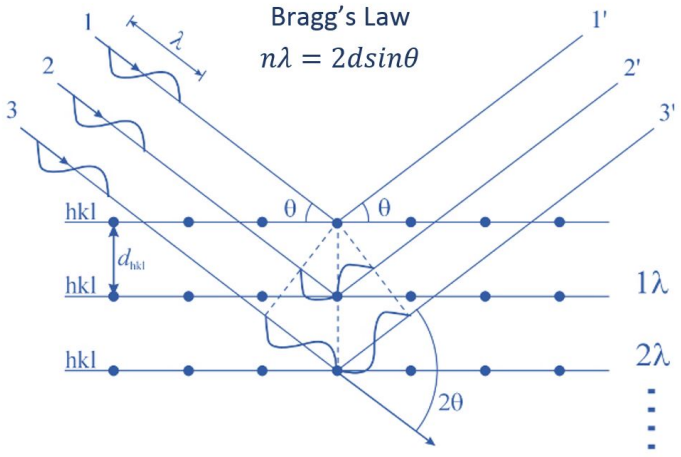

Figure 2-3: Bragg's Law, X-ray incidents at the plane (hkl).[2, 3]

Therefore, XRD pattern, measured by θ-2θ scan, can be used to determine the crystal structure. Additionally, the particle size of the material can also be determined by using Scherrer equation as the following:

$$\tau = \frac{K\lambda}{\beta cos\theta}$$

where τ is the mean size of the crystalline domains, K is a dimensionless shape factor and it has a typical value of about 0.9, but varies with the actual shape of the crystalline, λ is the wavelength of the X-ray, β is the line broadening at half the maximum intensity (FWHM) in radius and θ is the Bragg angle.

In Institute of Materials Science at University of Connecticut, Bruker D2 Phaser with Cu Kα radiation (λ=1.540598 is frequently used to study the crystalline structure in this research work.

2.2.2: Scanning Electron Microscope

Scanning electron microscope (SEM) is one kind of electron microscope and commonly used to detect the morphology of the material by scanning it with a focused beam of electrons. Secondary electron (SE) and back-scattered electrons (BSE) are the most common two types of signals used in SEM facilities, shown in **Figure 2-4**.

Secondary electrons (SE) are emitted from very close to the specimen surface and thus, SE mode is good for observation of topography.[8] As for back-scattered electrons, they are bean electrons reflected from the sample by elastic scattering. However, BSE signal is strongly related to the atomic number (Z) of the specimen and thus, BSE can be very useful for the observation of the distribution of different elements in the specimen.

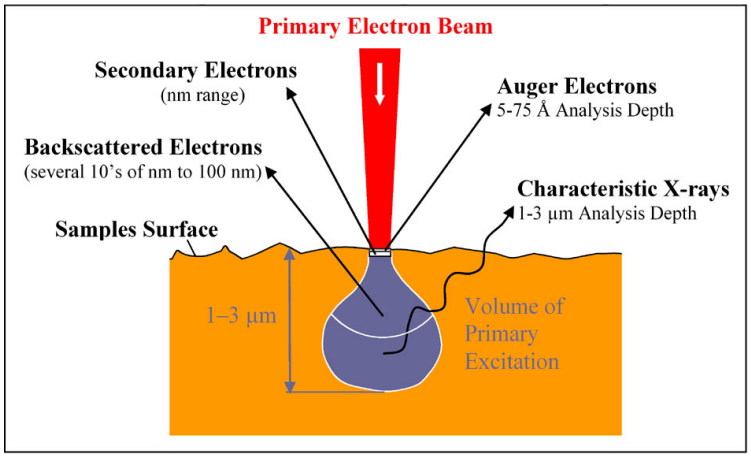

Figure 2-4: Primary electron beams and other types of electrons.

Besides, SEM always equipped with energy dispersive X-ray spectroscopy (EDXS or EDX) which is a powerful tool for the elemental analysis of a specimen. The working mechanism of EDXS is that the incident beam may excite an electron in an inner shell

and create an electron hole. Following by an electron from an outer, higher-energy shell would fill the hole created by the incident beam. Therefore, the energy difference between the outer, higher-energy shell and inner, lower-energy shell may be released in the form of X-ray, shown in **Figure 2-5**. This set of characteristic X-rays is element-dependent and therefore can be differentiated on the EDXS spectrum.[9]

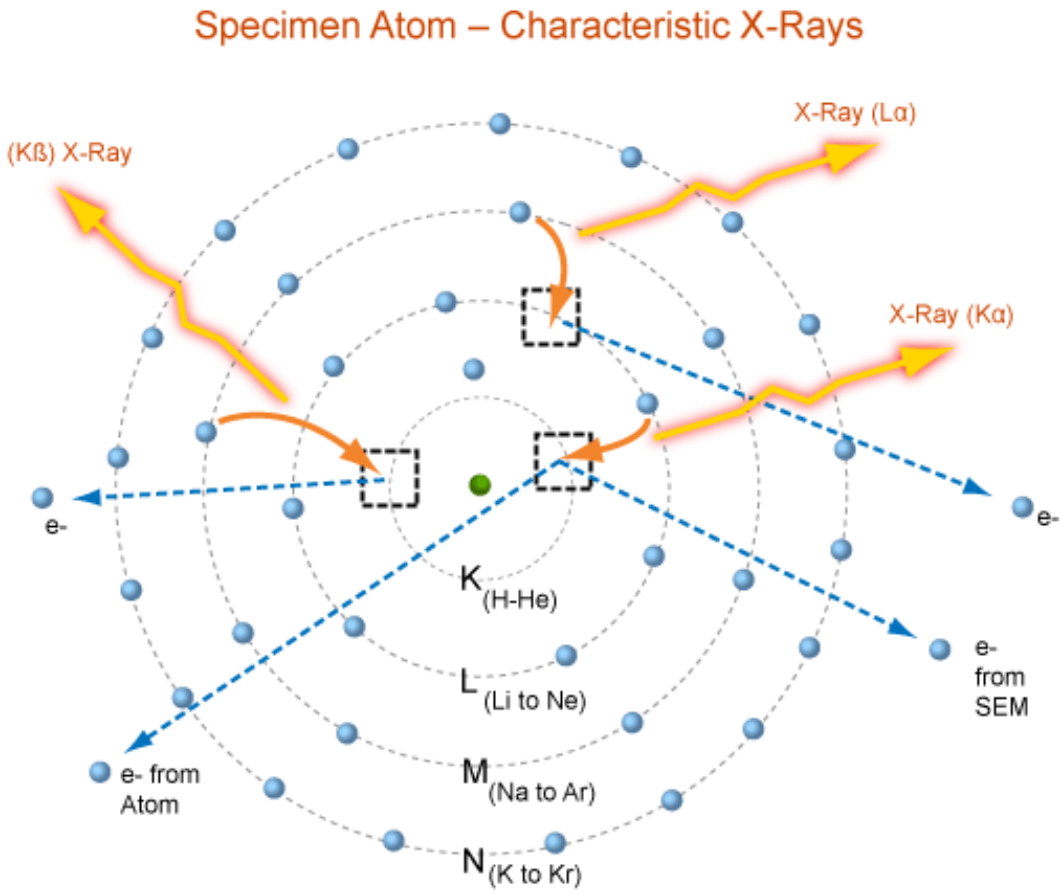

Figure 2-5: Formation of characteristic X-ray.

In the Institute of Materials Science at University of Connecticut, a field emission scanning electron microscope (FESEM, JEOL 6335F) equipped with EDXS is mostly used for the topography observation.

2.2.3: Transmission Electron Microscope

Transmission electron microscopy[10] is another powerful tool which can provide different important information, such as bright field image, dark field image, select area diffraction pattern, chemical composition or high resolution lattice image.

For images, the contrast formation in the TEM depends on the mode of operation. The most common mode is bright field imaging mode, for example, if the region is thicker or the area with a higher atomic number, the bright field image would show dark since the electrons are absorbed in the area. However, for the diffraction contrast mode, also known as dark field imaging mode, the image will appear bright wherever scattering happens.

Diffraction pattern can also be present. For example, single crystal specimen can produce a pattern of dots, polycrystalline specimen can generate a ring pattern (which is a combination of lots of single dots). More specific, the diffraction pattern is dependent upon the orientation of the specimen and the electron beam. By calculation, the plane or the orientation of the specimen can be determined through diffraction patterns.

In Institute of Material Science at University of Connecticut, Tecnai T12, JEOL 2010, Talos F200X are used for TEM microstructure analysis in this work.

2.2.4: X-ray Photoelectron Spectroscopy

X-ray photoelectron spectroscopy (XPS) is an established method to determine the elemental composition and the chemical state of solid surface. Using X-ray as the energy source to excite electrons from the core levels of the atoms of the solid into the vacuum.

Thus, XPS explores the electronic structure of matter with elemental sensitivity and chemical state specificity.[11]

When a solid is struck with X-ray photons, the entire incident photon energy ($\hbar\omega$) can be transferred to the electron with binding energy E_B below the vacuum level and then promoted to an unoccupied state above the vacuum level. As a result, the electron is ejected into the vacuum with kinetic energy:

$$E_{kin} = \hbar\omega - E_B$$

and can be detected by an electron energy analyzer.

However, conventionally the binding energy of the solid surface is measured with respect to the Fermi level rather than to the vacuum level. Therefore, the relationship can be re-written as the following:

$$E_{kin} = \hbar\omega - E_B - \Phi_\omega$$

Φ_ω is the work function of the material and represents the minimum energy required to remove an electron from the solid and it can be seem as an energy barrier that electrons need to overcome in order to escape from the surface into the vacuum. The schematic view of photoemission process is shown in **Figure 2-6**.

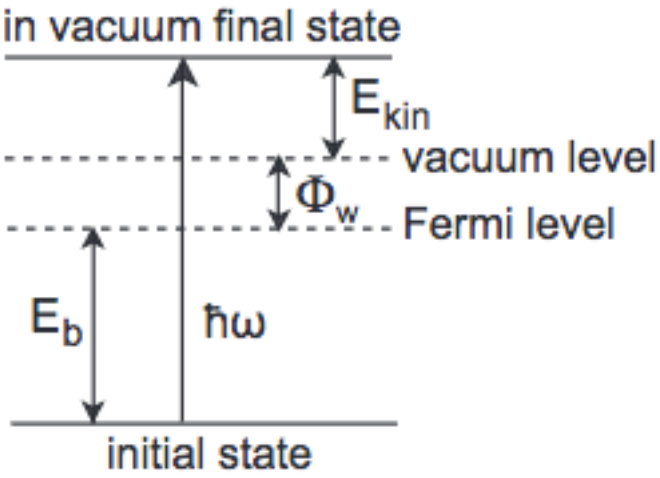

Figure 2-6: Photoemission process and the relationship of corresponding energies.

By recording the number of photoelectrons as a function of the kinetic energy at a given photon energy, a typical XPS spectrum is obtained. It can also be plotted as a function of the binding energy. XPS spectrum consists of a succession of distinct lines, however, the binding energies of core levels are different for each chemical element. Thus, XPS spectrum can serve as fingerprint for each element.

Binding energy depends on the chemical environment of the atoms and the energy shift may occur when inquivalent atoms of the same elemental species are present. The shift is called chemical shift. Basically, electrons emitted from atoms in a higher positive oxidation state demonstrate high binding energy because of the high Coulomb interaction with the ion core upon withdrawal of valence charge due to chemical bonding. By comparison with the database, the binding energy shifts can be used to determine oxidation states which were influenced by surrounding atoms.

2.3: Gas Sensing Property Characterization

The high temperature gas sensing properties of β-Ga_2O_3 nanorod arrays were tested by monitoring the potentiostatic current response of the β-Ga_2O_3 nanorod array device to target gas exposure in a high temperature tube furnace equipped with an alumina tube, electrical feedthroughs (Ni/Cr lead wires), and a gas injection system. Pt wires (10 mm diameter) were used to connect the nanorod gas sensor placed in the center position of the tube to Ni/Cr lead wires, which were externally connected to an electrochemical work station (CHI 601C). The nanorod sensor was subjected to a fixed 1 volt direct current (DC) bias while being heated from room temperature to 500 or 800 °C in air with a heating rate of 20 °C/min. The responses of the nanorod sensor to target gases were evaluated by measuring the magnitude of current change upon the exposure to various concentrations of target gases under a dynamic gas flow condition with a constant flow rate of 1.5 L/min (high purity N_2 as carrier gas), which was regulated by a computer-controlled gas mixing system (S-4000, Environics Inc., USA). The desired concentrations of the target gas can be achieved by the gas cylinder connected to one port of the system and diluted by another pure nitrogen cylinder connected in another port of the gas mixing system.

Reference

1. Maurya, D. K.; Sardarinejad, A.; Alameh, K., Recent Developments in R.F. Magnetron Sputtered Thin Films for pH Sensing Applications—An Overview. *Coatings* 2014, 4, 756-771.
2. Illinois, U. o., Development of X-Ray Crystallography. http://publish.illinois.edu/x-raycrystallography/ 2014.
3. Xia, Y.; Yang, P.; Sun, Y.; Wu, Y.; Mayers, B.; Gates, B.; Yin, Y.; Kim, F.; Yan, H., One-Dimensional Nanostructure. *Adv. Mater.* 2003, 15, 353-389.

4. Xu, S.; Wang, Z. L., One-Dimensional ZnO Nanostructures: Solution Growth and Functional Properties. *Nano Res.* 2011, 4, 1013-1098.
5. Wang, Z. L.; Gao, R. P.; Pan, Z. W.; Dai, Z. R., Nano-Scale Mechanics of Nanotubes, Nanowires, and Nanobelts. *Adv. Funct. Mater.* 2001, 3, 657-661.
6. Kelly, P. J.; Arnell, R. D., Magnetron Sputtering: A Review of Recent Developments and Applications. *Vacuum* 2000, 56, 159-172.
7. Mattox, D. M., Particle Bombardment Effects on Thin-Film Deposition: A Review. *J. Vac. Sci. Technol., A* 1989, 7, 1105-1114.
8. Seiler, H., Secondary Electron Emission in the Scanning Electron Microscope. *J. Appl. Phys.* 1983, 54, R1.
9. Characteristic X-rays. *Australian Microscopy & Microanalysis Research Facility* http://www.ammrf.org.au/myscope/analysis/eds/xraygeneration/characteristic/.
10. Kolmakov, A.; Klenov, D. O.; Lilach, Y.; Stemmer, S.; Moskovits, M., Enhanced Gas Sensing by Individual SnO_2 Nanowires and Nanobelts Functionalized with Pd Catalyst Particles. *Nano Lett.* 2005, 5, 667-673.
11. Turner, N. H.; Dunlap, B. I.; Colton, R. J., Surface Analysis X-ray Photoelectron Spectroscopy Auger Electron Spectroscopy and Secondary Ion Mass Spectrometry. *Anal. Chem.* 1984, 56, 373R-416R.

CHAPTER 3

Preparation of GaOOH / β-Ga_2O_3 Nanorod Arrays

Single-crystalline gallium oxide hydroxide (GaOOH)[1] nanorod arrays (NRAs) with preferential orientation were successfully fabricated on silicon (Si) (100) substrates through hydrothermal synthetic method using simply gallium nitrate as the precursor acts as a gallium source in deionized water and without any other surfactant. The diagonal length of the diamond tip of GaOOH nanorods is around 175~350 nm and the length of the nanorod is about 1-2 μm. Gallium oxide (β-Ga_2O_3) NRAs can then be obtained after annealing at 1000°C for 4 hours. Basic material characterizations, such as X-Ray diffraction (XRD), scanning electron microscope (SEM) and transmission electron microscope were used to understand the structural information of GaOOH and β-Ga_2O_3 NRAs. Possible mechanisms for the formation of diamond tip were also discussed in this chapter. Based on these 3-dimentional (3-D) β-Ga_2O_3 NRAs, we design and investigate the high temperature sensing performance in the following chapters.

3.1: Introduction

Nowadays, one-dimensional (1-D) nanostructured materials in the form of nanowires, nanorods, nanotubes or nanobelts have aroused attentions of materials chemistry scientists for pass few decades due to novel properties associated with a typically large surface-to-volume ratio (S/V) and finite or quantum size effects, which could lead to become potential candidates in future applications.

Metal oxide hydroxides are of considerable significant in the various fields, such as catalysis, fluorescence material and so on. Among these metal oxide hydroxides, GaOOH has been reported to be a good photocatalytic material. Besides, it is an important starting precursor for the direct synthesis of wide-band-gap β-Ga_2O_3 (4.2~4.9 eV) or GaN by simple heat treatment.[2-4] Generally speaking, GaOOH can be transformed into various phases (α, β and γ) of Ga_2O_3 after dehydration at suitable temperature.[5-7] Therefore, lots of efforts have been paid to the synthesis of GaOOH and its transformation into various Ga_2O_3 phases.

It has been illustrated that synthesis of Ga_2O_3 nanomaterials can be achieved through simple heat treatment of GaOOH, which is easy, feasible and efficient. The size and morphology of Ga_2O_3 may be controlled indirectly by controlling the size and morphology of GaOOH precursor. In the past few decades, several researchers have reported the transformation between GaOOH and Ga_2O_3. Tas *et al.* found GaOOH starts to transform into rhombohedral polymorph of Ga_2O_3 (α-Ga_2O_3) at 500°C, monoclinic polymorph of Ga_2O_3 (β-Ga_2O_3) at 750~1200 °C.[8] Sun *et al.* reported GaOOH nanorods can be synthesized from $Ga(NO_3)_3$ by microwave hydrothermal method.[9] Zhao *et al.* demonstrated β-Ga_2O_3 can be obtained from GaOOH by calcination at 900 °C.[10]

However, gallium oxide has been successfully synthesized by thermal decomposition, thermal oxidation, carbothermal reduction, vapor-liquid-solid process, homogeneous precipitation, etc.[11-15] However, the methodologies mentioned above hardly provide well control over structural, morphological, or compositional properties. In addition, many of the preparation methods have involved complicated procedures and precursors, which would lead to suffer from high production cost, low yield or low purity. Among the

numerous methods developed for the preparation of 1-D inorganic nanomaterials so far, the chemical solution routes seem to offer a more promising direction in terms of cost or potential for large-scale production.

However, for the purpose of fabricating three-dimensional (3-D) nanorod arrays, many researchers used templates, such as anodic aluminum oxide (AAO) membranes to grow different metals or metal oxides nanorod arrays.[16] Undoubtedly, the extra templates or other surfactant would help synthesize 3-D nanostructured materials but at the same time, they would also cause a higher cost and a more complicated purification procedure or higher level of pollution to the product and environment.

Recently, an increasing interests and emphases on the green synthesis topic, which the goal of fabrication process is to eliminate the procedure steps and minimize generated waste. The merits of green synthesis strategy also include non-toxic reactants and produce none unwanted by-products. Thus, in this work, we report a complete green method to synthesize 3-D GaOOH nanorod arrays without any surfactant or template via hydrothermal synthesis method and further heat treatment to fully convert to β-Ga_2O_3 nanorod arrays.

3.2: Experimental

To prepare the GaOOH and β-Ga_2O_3 nanorod arrays, all the chemicals, substrates needed in the whole hydrothermal synthesis process were listed here.

3.2.1: Precursor and Substrate

(I) Gallium(III) nitrate hydrate ($Ga(NO_3)_3 \cdot 9H_2O$, 99.9998%): the gallium salt of nitric acid was purchased from Acros Organics. It's a white, slightly hygroscopic and crystal powder with good solubility in water. It's used as the precursor of hydrothermal synthesis in this work.

(II) Tin dioxide (SnO_2, >99.9%): the inorganic compound target with diameter 2" and 0.25" in thickness was purchased from Stanford Advanced Materials. The white circular target with molecular weight 150.71 was used as the seed layer for further hydrothermal synthesis.

(III) Silicon (Si, (100)): substrates (boron doped, p-type, 1~10 ohm-cm, 100 mm in diameters, 500 mm in thickness, single flat, single side polish) topped with 1mm silicon dioxide (SiO_2) were purchased from University Wafer.

(IV) Deionized Water (DI Water): it's used as solvent for hydrothermal method and to clean the sample after the growth process.

3.2.2: Preparation of GaOOH Nanorod Arrays

In the first place, Si substrates should be cleaned by sonication in acetone solution for 5 minutes and rinsed for another 5 minutes by deionized (DI) water to remove surface grease and organic deposits. Repeat twice and then hold Si substrates tilt and use high purity N_2 to purge the surface in one direction from high to low to remove the residual water on each side of the surface of Si substrates. Then put Si substrates on the hot plate, keep at 80 °C. In the next step, a seed layer used to help synthesize 3-D nanorod arrays was prepared by sputtering SnO_2 with 50 nm thickness on Si substrates and followed by

ambient post-annealing at 900 °C for 2 hours to make it crystalline. Afterwards, gallium hydroxide (GaOOH) nanoroad arrays were fabricated on Si/SiO_2 substrates through hydrothermal method. By dissolving 0.6g $Ga(NO_3)_3 \cdot 9H_2O$ in 40 ml deionized (DI) water and stirred for 10 minutes, a $Ga(NO_3)_3$ solution with the pH value controlled at around 2 was prepared. Pour the prepared solution into the Teflon bottle and fix the SnO_2-sputtered Si substrates on Teflon bar, vertical GaOOH nanorod arrays were then grown on SnO_2 seed layer of the Si substrates incubated in the precursor solution at 150 °C for 12 hours for the hydrothermal growth.

Besides, the following description shows how to split the Si substrate, shown in **Figure 3-1**. The Si substrates, topped with 50 nm SnO_2 as seed layers were cut and split by the diamond pen. First, put the substrates on the clean wipers upside down and press the substrates with one hand in glove to hold the substrate. Then, use the diamond pen to create one tiny notch on the edge of the substrate, and hold the Si substrates with two flat head tweezers by the side of the notch. Press the two flat head tweezers and the substrate will be split along the cleavage plane due to the stress concentration on the notch.

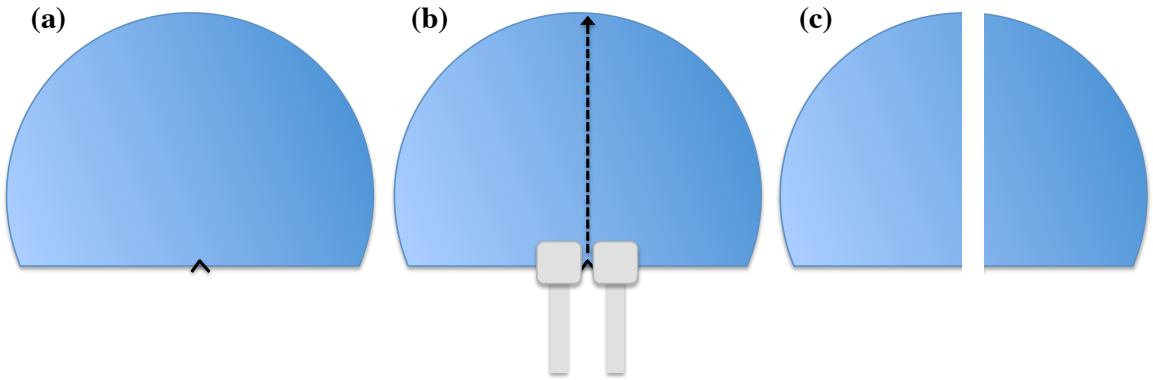

Figure 3-1: Steps to cut Si substrates, (a) create a notch on the edge, (b) hold the substrate with two flat head tweezers, (c) press and split.

3.2.3: Preparation of β-Ga_2O_3 Nanorod Arrays

β-Ga_2O_3 nanorod arrays can be transformed from GaOOH nanord arrays. After the hydrothermal growth process, the fabricated GaOOH nanorod arrays samples were then washed by DI water couple times and dried at 80 °C in the ambient atmosphere, and put samples in the oven, annealed at 1000°C for 4 hours to convert into pure β-Ga_2O_3 nanorod arrays completely.

3.3: Results and Discussion

The weight and two dimensions, width and length, of each rectangle Si substrate covered with 50 nm SnO_2 seed layer (shown in **Figure 3-2(a)**) were measured.

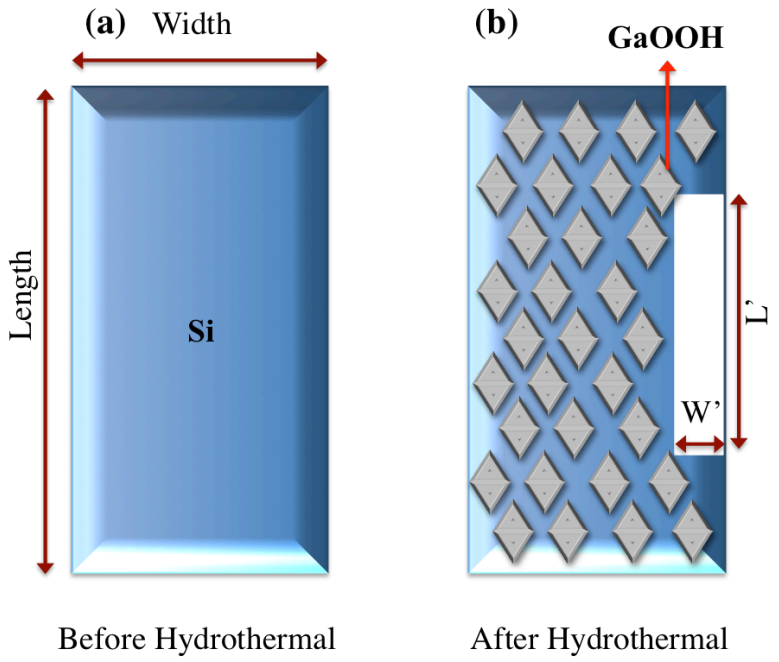

Figure 3-2: Top view of the configurations of the samples (a) before hydrothermal synthesis process, (b) after growth. W', L' represent the area inserted into the Teflon bar.

In the first place, we try to find the correlation between the weight and unit volume of the Si substrate. Since the thickness of the Si substrate is 500 μm, we can simply measure the length and width and measure the weight of different samples to find out weight per volume of the Si substrate. **Table 3-1** records weight, length, width, corresponding area and weight per area of each sample. And the relationship between weight and area of the substrates was plot in **Figure 3-3**. The slope in the figure represents the weight per area ($\frac{g}{cm^2}$) and it's around 0.1152 from the fitting line, which means the weight of the square Si substrate with 1 cm^2 area (1cm x 1cm), topped with SnO_2 as seed layer is about 115.2 mg.

Table 3-1: Dimensions, area and weights of Si substrates with seed layers.

Sample	Length (cm)	Width (cm)	Area (cm^2)	Weight of the Substrate (g)	Weight/Area (g/cm^2)
1	1.7	0.5	0.85	0.1064	0.125176471
2	2	0.7	1.4	0.1777	0.126928571
3	2	1.15	2.3	0.2702	0.117478261
4	2.05	1.37	2.8085	0.3252	0.115791348

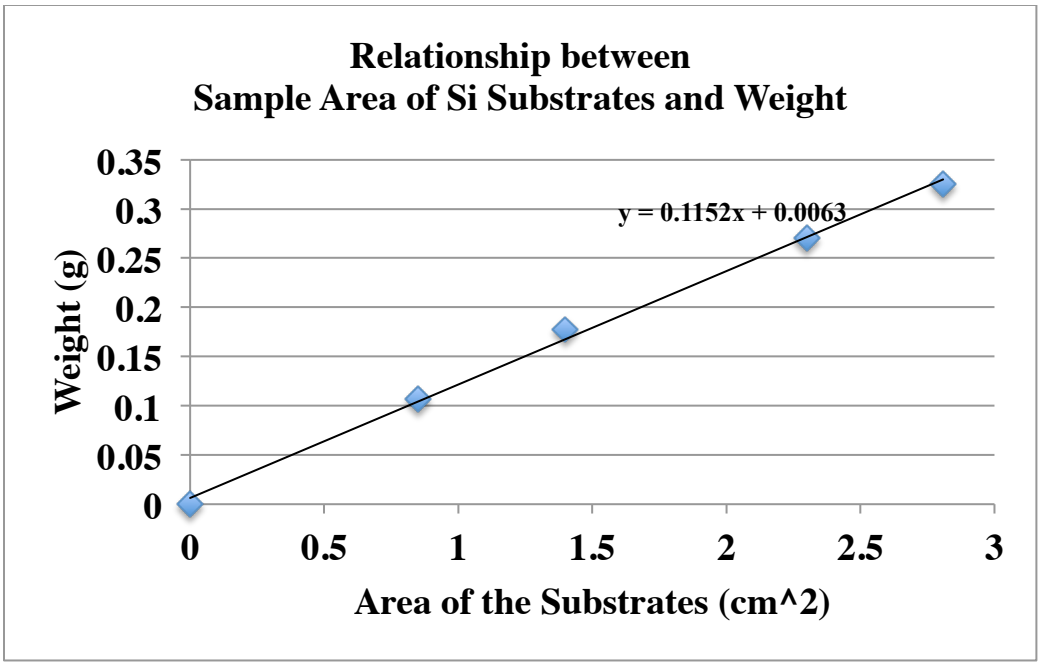

Figure 3-3: The correlation between the weight and area of the Si substrates. The thickness of the Si substrates is 500 μm.

In order to understand how much weight GaOOH nanorod arrays were grown on the substrates, after the hydrothermal synthesize process at 150 °C for 12 hours, the weight of grown GaOOH can be measured as well. However, it should be noticed that the active area for hydrothermal growth is smaller than original area of Si substrate because of the insertion part of the Si substrate, which will be blocked by the Teflon bar, shown in **Figure 3-2(b)**.

Therefore, the length and width of the insertion area, represented by L' and W' accordingly, were recorded and thus the active area for hydrothermal process can be modified. The net weight of GaOOH nanorods can also be calculated by simply deduce the weight of the substrate from that of the sample after hydrothermal growth. Finally, the

net weight of GaOOH nanorods per unit area can be calculated from the slop of **Figure 3-4**, and it's around 1.1 ($\frac{mg}{cm^2}$).

Table 3-2: Dimensions, area and weights of samples after hydrothermal synthesis process.

Sample	Insert Bar Length (cm)	Insert Bar Width (cm)	Insert Bar Area (cm^2)	Active Area (cm^2)	Weight_After Hydrothermal (g)	Weight_Net _GaOOH (g)	(Weight_Net_GaOOH) / (Active Area) ($\frac{g}{cm^2}$)
1	1.15	0.19	0.2185	0.6315	0.1069	0.0005	0.000791766
2	1.15	0.18	0.207	1.193	0.179	0.0013	0.00108969
3	1.09	0.15	0.1635	2.1365	0.2723	0.0021	0.000982916
4	1.17	0.14	0.1638	2.6447	0.3282	0.003	0.001134344

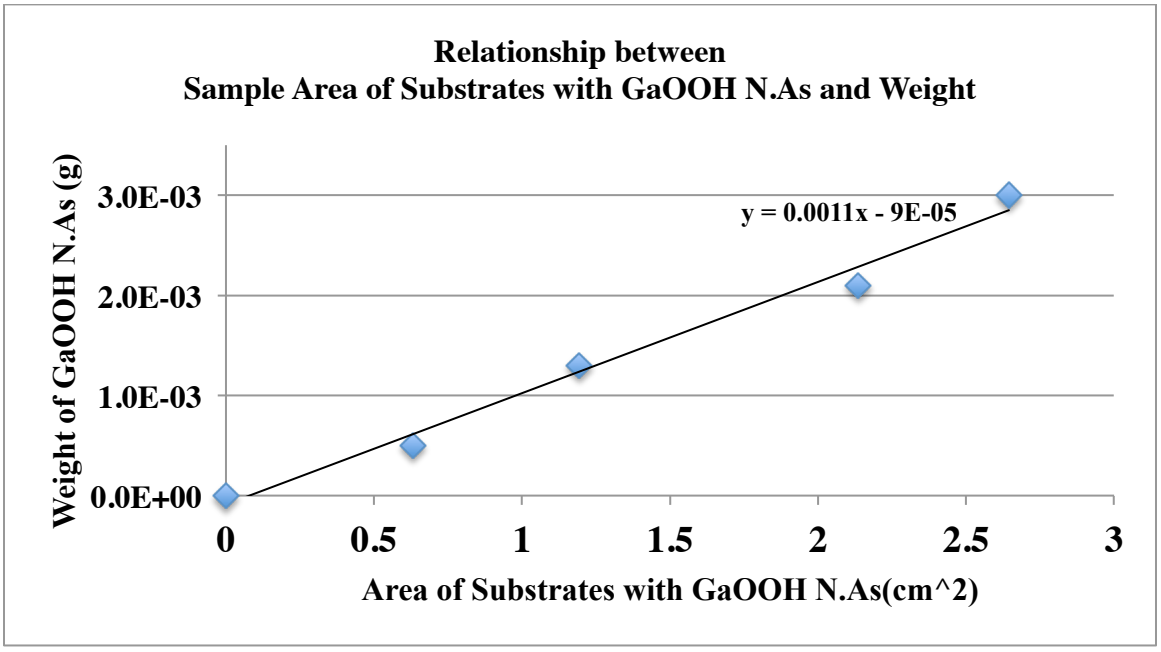

Figure 3-4: After hydrothermal synthesis, the correlation between the net weight of GaOOH nanorods and unit area of the substrates.

3.3.1: Material Characterization

XRD: X-ray diffraction pattern shown in **Figure 3-5(c)** reveals that the obtained nanorods are identified as single-phase GaOOH, referring to Joint Committee on Powder Diffraction Standards (JCPDS, file number 06-0180)(**Figure 3-5(a)**).

The formation of GaOOH in the aqueous gallium nitrate solution is considered to follow the equation:

$$Ga^{3+} + 2H_2O \rightarrow GaOOH + 3H^+$$

The thermohydrolysis of metal cations in aqueous solutions and its kinetics are usually influenced by temperature. However, at high temperature, water acts effectively as a reactant in hydrolysis because of the decreased dielectric constant, the decreased viscosity and the increased ionic product of water. Generally, solubility of solute can change as a result of chemical reactions in solutions. Solid particles are formed through nucleation and crystal growth when the solution undergoes super-saturation. The growth tends to carry on along the c-axis [001] direction, therefore, the rod-like structure morphology is observed on GaOOH which is fabricated by hydrothermal synthesis process. Besides, additional base (OH^-) would tend to promote the growth along the [110] or [010] direction and lower the aspect ration of the nanorods.[8]

$$2\ GaOOH \rightarrow Ga_2O_3 + H_2O$$

Figure 3-5(d) depicted an XRD pattern of the sample annealed at 1000 °C for 4 hours and it reveals that the single phase β-Ga_2O_3 (JCPDS, file number 41-1103)(**Figure 3-5(b)**) can be fully transformed from GaOOH.

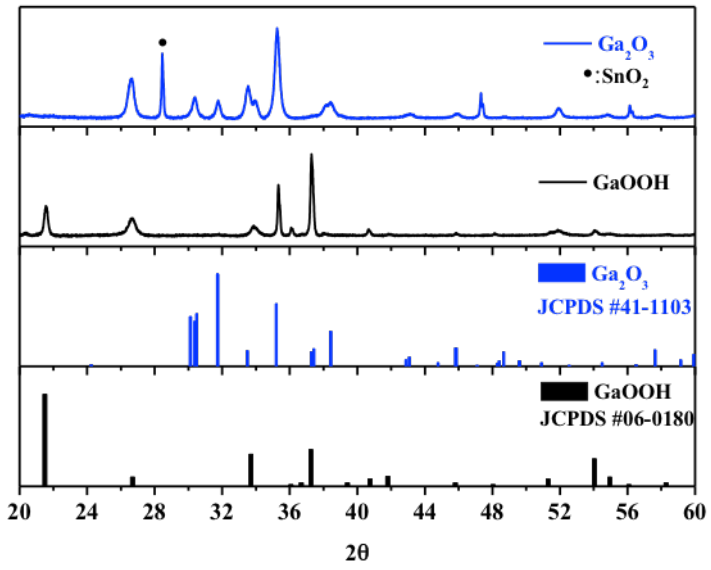

Figure 3-5:(a) JCPDS card of GaOOH, (b) JCPDS card of Ga_2O_3. X-ray diffraction patterns of (c) GaOOH nanorod arrays and (d) Ga_2O_3 nanorod arrays.

Besides, different annealing temperatures were also examined. Based on the literatures, Zhao *et. al.* reported β-Ga_2O_3 materials could be obtained from GaOOH precursors by calcination at 900 °C.[10] Tas *et al.* demonstrated that calcinated GaOOH materials started to transform into β-Ga_2O_3 in air at temperature higher than 500 °C.[8] Laubengayer and Engle discussed the transformation of GaOOH and β-Ga_2O_3 polymorphs in the temperature range of 110 – 1000 °C.[17] Shi *et. al.* reported calcination of GaOOH materials at middle temperature (500~570 °C) would lead to the mixture of α-Ga_2O_3 and β-Ga_2O_3 and pure β-Ga_2O_3 phase could be obtained after calcination at 800 °C. Therefore, we calcinate GaOOH nanorod arrays at 850 and 1000 °C and compare the XRD patterns, shown in **Figure 3-6**. GaOOH nanorod arrays were fully transformed into β-Ga_2O_3 phase at 850 °C. However, compare with the peak of (111), the peak from Ga_2O_3 obtained at 850 °C was more broadening than 1000 °C. It might due to the

coarsening of the structure or the improvement of the crystallinity. Therefore, all the β-Ga_2O_3 nanorod arrays used in this thesis were obtained at 1000 °C for 4 hours.

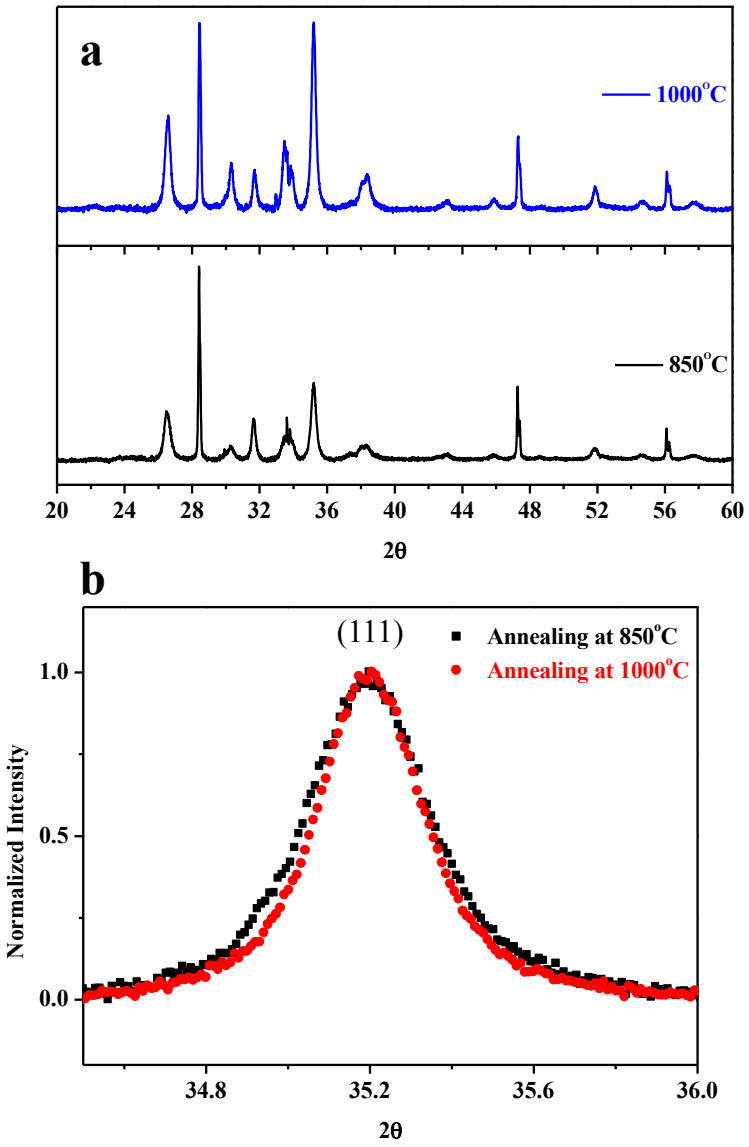

Figure 3-6: (a) XRD of Ga_2O_3 annealing at 850 and 1000 °C, (b) comparison of peak (111).

The surface morphology images of GaOOH and Ga_2O_3 nanorod arrays were shown in **Figure 3-7**. The tip of the GaOOH nanorods is diamond-like shape with the diagonal length is around 170~350 nm. After annealing at 1000 °C for 4 hours, the morphology

remains the same with similar diamond-like shaped tips due to the high melting point of Ga_2O_3, which could resist high temperature.

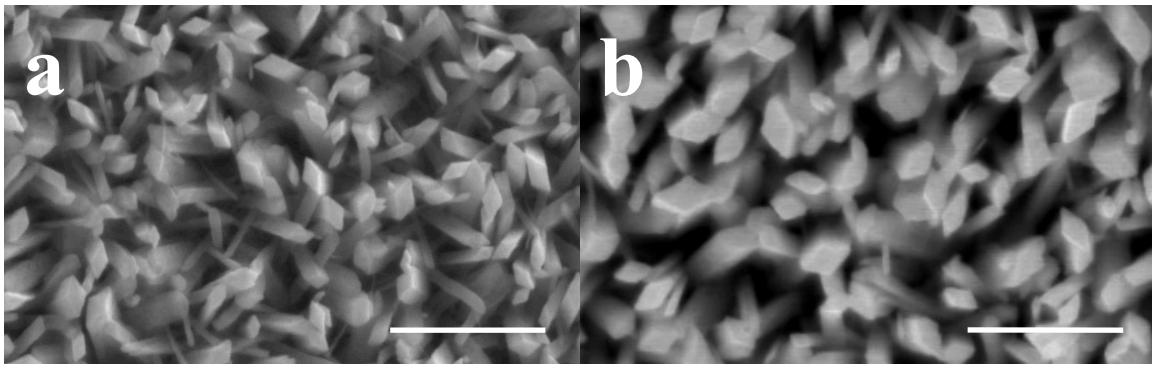

Figure 3-7: SEM top view images of (a) GaOOH and (b) Ga_2O_3 nanorod arrays. The scale bar in this figure is 1 μm.

3.3.2: Growth Mechanism

Rod-shaped GaOOH was usually made and prepared by homogeneous nucleation from chemical solutions in powder form.[6, 9, 18] However, it's essential to grow vertically aligned GaOOH nanorod arrays on substrates for practical device applications. It's found the vertically aligned GaOOH nanorod arrays can be grown on stiff substrates by chemical deposition using different seed layers, such as SnO_2 and MgO.[19] The most possible reason should be due to low lattice mismatch of SnO_2 or MgO with GaOOH for *a*-axis, which the detail crystal information of GaOOH, SnO_2 and MgO is shown in **Table 3-3**.

Table 3-3: Crystal information of GaOOH, SnO_2 and MgO

Material	GaOOH	SnO_2	MgO
ICDD Number	06-0180	77-0450	45-0946
Crystal Structure	Orthorhombic	Tetragonal	Cubic
a (Å)	4.58	4.745	4.211
b (Å)	9.8	4.745	4.211
c (Å)	2.97	3.193	4.211
α (°)	90	90	90
β (°)	90	90	90
γ (°)	90	90	90

The key role of fabricating nanorod arrays on firm substrates was to choose the suitable seed layers and then heterogeneous nucleation occurred on the seed layer of the substrates. Based on the theory of classical thermodynamic, the relationship between the critical energy barrier of heterogeneous and homogeneous nucleation is determined by the equation:

$$\Delta G_c^* = f(\theta)\Delta G_c$$

where ΔG_c^* represents the critical energy barrier for heterogeneous nucleation, ΔG_c represents the critical energy barrier for homogeneous nucleation and $f(\theta)$ is a factor defined by:

$$f(\theta) = \frac{(2 + cos\theta)(1 - cos\theta)^2}{4}$$

The range of $f(\theta)$ is $0 \leq f(\theta) \leq 1$ and therefore, $0 \leq \Delta G_c^* \leq \Delta G_c$.

Besides,

$$cos\theta = \frac{\gamma_s - \gamma_{sn}}{\gamma_n}$$

where γ_s, γ_n, γ_{sn} represent the surface energy of the substrate, nucleus and the interfacial energy between them at solid-solid interface, respectively. In the condition of $\gamma_s = \gamma_n$ and $\gamma_{sn} = 0$, that leads to $cos\theta = 1$, $f(\theta) = 0$ and therefore, $\Delta G_c^* = 0$ for the epitaxial systems. On the other hand, in the condition of $\gamma_{sn} = \gamma_s + \gamma_n$, which leads to $\Delta G_c^* = \Delta G_c$ in the case of homogeneous nucleation without the influence of the substrate. Therefore, due to the heterogeneous nucleation, the nucleus of GaOOH is first induced by SnO_2 seed layer.

As for the growth of GaOOH nanocrystals, Zhang *et al*. proposed solution-solid process,[20] which happens when the temperature and pressure of the hydrothermal system increase, the nanocrystalline Ga_2O_3 molecules gradually dissolve in the water and hydroxylate to GaOOH ($Ga_2O_3 + H_2O \rightarrow 2$ GaOOH or $Ga_2O_3 \cdot H_2O$). As the concentration of GaOOH increases to supersaturation, the oxyhydroxide recrystallizes into 1D nanorods probably due to the inducement effect from the inherent crystal structure of GaOOH.[8] Avivi *et al.* proposed bubble-liquid interface growth mechanism,[21] the formation of the oxide occurs at the solution-bubble interface and it's related to the collapse of the bubble which GaOOH is formed as a layer surrounding the collapsing bubble in the sonochemical reaction. However, the two growth mechanisms described above are based on powder precursor and sonochemical reaction. Chen *et al.* proposed the growth mechanism in the hydrothermal synthesis process,[22] the growth of a GaOOH nanorod relied on its crystal structure, orthorhombic, and the possible growth processes can be described as the following:

1. GaOOH nanoparticles are formed in the first place, followed by the crystal nuclei are assembled to form the trunk of rods.

2. Since the lattice constant *a* (4.58Å) is about half of *b* (9.8Å), and the diagonal length ratio of diamond-like top is around 2:1, which are formed by homogeneous growth of lattice planes {110}, along [410], [4-10], [-410] and [-4-10] directions of orthorhombic GaOOH, shown in **Figure 3-8**.

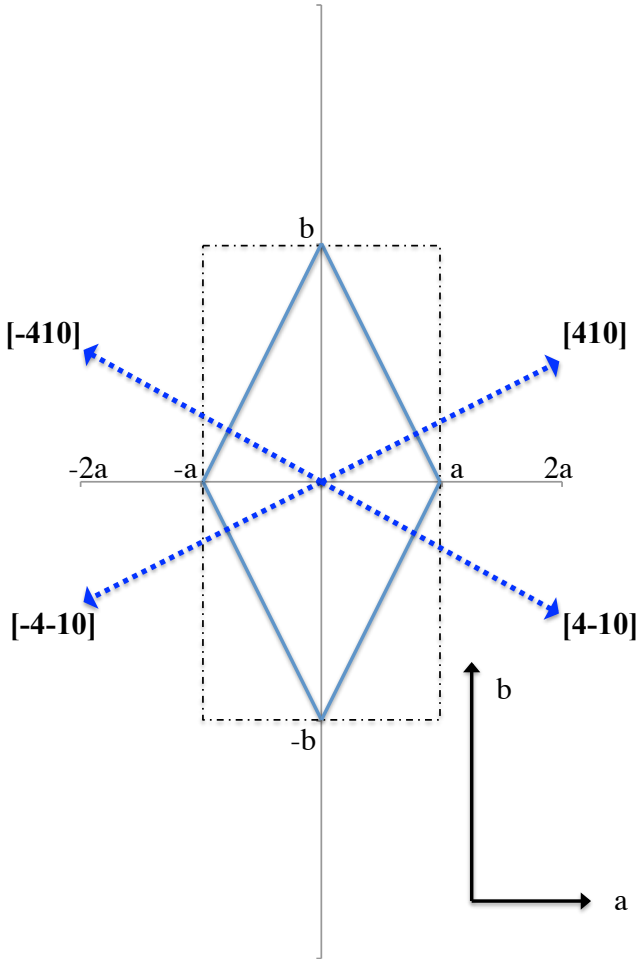

Figure 3-8: The cross-sectional view of the orthorhombic GaOOH along c-axis.

3.4: Conclusions

In this chapter, the preparation and growth mechanism of GaOOH were discussed. The results showed that the seed layer with suitable lattice parameters which are close to that of GaOOH would lead to an epitaxial growth perpendicular to the substrate. Therefore,

less lattice mismatch between the seed layer and the nanorod would lead to nanorod arrays for the hydrothermal synthesis process.

Besides, after annealing at high temperature, GaOOH nanorod array can fully transform into β-Ga_2O_3 nanorod array. However, the morphologies of GaOOH and β-Ga_2O_3 are similar, which the top of the rod is still diamond shape.

Reference

1. Chun, H. J.; Choi, Y. S.; Bae, S. Y.; Seo, H. W.; Hong, S. J.; Park, J.; Yang, H., Controlled Structure of Gallium Oxide Nanowires. *J. Phys. Chem. B* 2003, 107, 9042-9046.
2. Liu, G.; Duan, X.; Li, H.; Liang, D., Preparation and Photoluminescence Properties of Eu-Doped Ga_2O_3 Nanorods. *Mater. Chem. Phys.* 2008, 110, 206-211.
3. Zhang, J.; Liu, Z.; Lin, C.; Lin, J., A Simple Method to Synthesize β-Ga_2O_3 Nanorods and Their Photoluminescence Properties. *J. Cryst. Growth* 2005, 280, 99-106.
4. Ding, S.; Lu, P.; Zheng, J.-G.; Yang, X.; Zhao, F.; Chen, J.; Wu, H.; Wu, M., Textured Tubular Nanoparticle Structures: Precursor-Templated Synthesis of GaN Sub-Micrometer Sized Tubes. *Adv. Funct. Mater.* 2007, 17, 1879-1886.
5. Yan, S.; Wan, L.; Li, Z.; Zhou, Y.; Zou, Z., Synthesis of A Mesoporous Single Crystal Ga_2O_3 Nanoplate with Improved Photoluminescence and High Sensitivity in Detecting CO. *Chem. Commun.* 2010, 46, 6388-6390.
6. Huang, C.-C.; Yeh, C.-S., GaOOH, and β- and γ-Ga_2O_3 Nanowires: Preparation and Photoluminescence. *New J. Chem.* 2010, 34, 103-107.
7. Qian, H.-S.; Gunawan, P.; Zhang, Y.-X.; Lin, G.-F.; Zheng, J.-W.; Xu, R., Template-Free Synthesis of Highly Uniform α-GaOOH Spindles and Conversion to α-Ga_2O_3 and β-Ga_2O_3. *Cryst. Growth Des.* 2008, 8, 1282-1287.
8. Tas, A. C.; Majewski, P. J.; Aldinger, F., Synthesis of Gallium Oxide Hydroxide Crystals in Aqueous Solutions with or without Urea and Their Calcination Behavior. *J. Am. Ceram. Soc.* 2002, 85, 1421-1429.
9. Sun, M.; Li, D.; Zhang, W.; Fu, X.; Shao, Y.; Li, W.; Xiao, G.; He, Y., Rapid Microwave Hydrothermal Synthesis of GaOOH Nanorods with Photocatalytic Activity toward Aromatic Compounds. *Nanotechnology* 2010, 21, 355601.
10. Zhao, Y.; Frost, R. L.; Martens, W. N., Synthesis and Characterization of Gallium Oxide Nanostructures via aSoft-Chemistry Route. *J. Phys. Chem. C* 2007, 111, 16290-16299.
11. Sun, X.; Li, Y., Ga_2O_3 and GaN Semiconductor Hollow Spheres. *Angew. Chem.* 2004, 116, 3915-3919.
12. Michorczyk, P.; Ogonowski, J., Dehydrogenation of Propane to Propane over Gallium Oxide in the Presence of CO_2. *Appl. Catal., A* 2003, 251, 425-433.

13. Gundiah, G.; Govindaraj, A.; Rao, C. N. R., Nanowires, Nanobelts and Related Nanostructures of Ga_2O_3. *Chem. Phys. Lett.* 2002, 351, 189-194.
14. Dai, Z. R.; Pan, Z. W.; Wang, Z. L., Gallium Oxide Nanoribbons and Nanosheets. *J. Phys. Chem. B* 2002, 106, 902-904.
15. Yada, M.; Ohya, M.; Machida, M.; Kijima, T., Mesoporous Gallium Oxide Structurally Stabilized by Yttrium Oxide. *Langmuir* 2000, 16, 4752-4755.
16. Lee, W.; Park, S.-J., Porous Anodic Aluminum Oxide: Anodization and Templated Synthesis of Functional Nanostructures. *Chem. Rev.* 2014, 114, 7487-7556.
17. Laubengayer, A. W.; Eagle, H. R., The Sesquioxide and Hydroxides of Gallium. *J. Am. Chem. Soc.* 1939, 61, 1210-1214.
18. Quan, Y.; Fang, D.; Zhang, X.; Liu, S.; Huang, K., Synthesis and Characterization of Gallium Oxide Nanowires via A Hydrothermal Method. *Mater. Chem. Phys.* 2010, 121, 142-146.
19. Fujihara, S.; Shibata, Y.; Hosono, E., Chemical Deposition of Rodlike GaOOH and β-Ga_2O_3 Films Using Simple Aqueous Solutions. *J. Electrochem. Soc.* 2005, 152, C764-C768.
20. Zhang, Y. C.; Wu, X.; Hu, X. Y.; Shi, Q. F., A Green Hydrothermal Route to GaOOH Nanorods. *Mater. Lett.* 2007, 61, 1497-1499.
21. Avivi, S.; Mastai, Y.; Gedanken, A., Sonochemical Hydrolysis of Ga^{3+} Ions Synthesis of Scroll-like Cylindrical Nanoparticles of Gallium Oxide Hydroxide. *J. Am. Chem. Soc.* 1999, 121, 4196-4199.
22. Chen, S. G.; Luo, S. M.; Zhou, Y.; Chen, Y.; Liu, Y. Q.; Long, C. G., A Simple Hydrothermal Route to GaOOH Intersecting-Rods with Regular Diamond-Like Cross Section. *Mater. Lett.* 2008, 62, 4566-4569.

CHAPTER 4

Perovskite Nanoparticle Sensitized Effects on Ga_2O_3-Based Sensors for CO Detection at High Temperature

Noble metal nanoparticles are extensively used for sensitizing metal oxide chemical sensors through the catalytic spillover mechanism. However, due to earth-scarcity and high cost of noble metals, finding replacements presents a great economic benefit. Besides, high temperature and harsh environment sensor applications demand material stability under conditions approaching thermal and chemical stability limits of noble metals. In this study, we employed thermally stable perovskite-type $La_{0.8}Sr_{0.2}FeO_3$ (LSFO) nanoparticle surface decoration on Ga_2O_3 nanorod array gas sensors and discovered an order of magnitude enhanced sensitivity to carbon monoxide at 500 °C. The observed performance of LSFO nanoparticle catalysts was comparable to that achieved by Pt-decoration, with over three times the weight loading of LSFO. Detailed electron microscopy and X-ray photoelectron spectroscopy studies suggested the LSFO nanoparticle sensitization effect is attributed to a spillover like effect associated with the gas-LSFO-Ga_2O_3 triple-interfaces that spread the negatively charged surface oxygen ions from LSFO nanoparticles surfaces over to β-Ga_2O_3 nanorod surfaces with faster surface CO oxidation reactions.

4.1: Introduction

According to U.S. Department of Energy, harsh environment sensors are predicted to save 0.25 quadrillion BTU/year of energy across all energy-consuming industries if successfully employed.[1, 2] In both automotive and stationary energy industries,

monitoring and controlling combustion-related emissions are top priorities for enhancing energy and environmental sustainability. However, commercially available sensor technologies for harsh environments are extremely limited due to the stringent requirements for sensor materials' high sensitivity as well as stability in structure and performance under harsh operating conditions. Therefore, there is an urgent need to develop new sensor materials meeting such performance criteria in sensitivity and robustness, which are preferentially combined with low cost.

Traditionally, metal oxides have been used as basic senor materials, and, in particular, a wide band gap β-Ga_2O_3 (~4.9 eV)[3] is promising for high temperature gas sensing, owing to its high thermal and chemical stabilities.[4-6] Ga_2O_3 thin-film-based gas sensors have been proven as promising oxygen sensors at high temperature of 600-1000°C. It also can detect reducing gases such as H_2, CO, CH_4, etc., at elevated temperature.[7] Meanwhile, with decreased size and increased surface-to-volume ratio, metal oxide nanorods have shown good potential for chemical sensors.[8, 9] In order to further improve the sensor performance, various strategies can be used to directly control and enhance the fundamental material properties affecting sensing characteristics, such as doping,[10, 11] surface functionalization,[12-14] and heterojunction design.[15, 16] Kim et al. demonstrated that the response of multiple-networked Ga_2O_3 nanowire sensors was enhanced ~17-fold by surface decoration of Pt nanoparticles.[17] Park et al. synthesized Ga_2O_3-core / GaN-shell nanowires by directly nitriding the surface of Ga_2O_3 nanowire and the results showed the CO sensing performance can be enhanced at 150°C by the created heteojunction.[18]

Among these approaches described above, the decoration of catalytically active noble metal on sensor material surfaces or interfaces has been one of the most effective and

widely used techniques in practice that resulted in substantial improvements in the sensor performance through the catalytic spillover mechanism.[13] However, due to the earth-scarcity, the concern over high cost of noble metals is an ongoing issue, and therefore, reduction or complete elimination of noble metal usage in the catalysts and related catalytic sensors would promise benefits not only to the relevant industries at large but also for addressing overarching concerns over global energy and environmental issues.[19] Therefore, finding replacements of noble metals presents a great economic benefit with a significant opportunity for enhancing material and manufacturing sustainability.

On the other hand, the significantly decreased melting points of noble metal nanoparticles (for example, the melting point of Pt nanoparticles could be reduced to ~600°C) due to a size effect coupled with inherent chemical instabilities also hinder their usage at elevated temperatures as sensitizers for harsh environment chemical sensors.[20-22] Tietz et al. reported perovskite material $La_{0.8}Sr_{0.2}FeO_3$ shows good thermal stability at high temperature. After sintering at 900-1300°C for 6 hours, the crystalline phases essentially keep the same.[23]

Herein, we report a new discovery in which trace amounts of alternative perovskite oxide nanoparticles dramatically sensitize metal oxide nanorod gas sensors at high temperature. Rare-earth-based perovskite oxides, an important class of high temperature stable functional materials having a number of remarkable physical and chemical properties, have shown their potentials for catalytic and functional applications as in our recent demonstrations of the improved performance of various metal oxide nanowire arrays via the application of thin film perovskites.[24-29] In the present work, we conducted a comparative study on the sensing properties of pristine, Pt-nanoparticle-, and

$La_{0.8}Sr_{0.2}FeO_3$(LSFO)-nanoparticle-sensitize Ga_2O_3 nanorod arrays and clearly show that the perovskite-nanoparticle decoration can enhance the gas sensitivity by an order of magnitude at high temperature with excellent dynamic gas sensing response characteristics, which overall rivals the performance of Pt sensitizing effects.

4.2: Experimental

To fabricate β-Ga_2O_3-based nanorod arrays for high temperature gas sensing, all the precursors, chemicals, substrates, etc., needed in the whole synthesis process and the procedures to fabricate the nanorod arrays gas sensors were listed here.

4.2.1: Precursor, Substrate and Sputtering Target Chemicals

(I) Gallium(III) nitrate hydrate ($Ga(NO_3)_3 \cdot 9H_2O$, 99.9998%): the gallium salt of nitric acid was purchased from Acros Organics. It's a white, slightly hygroscopic and crystal powder with good solubility in water. It's used as the precursor of hydrothermal synthesis in this work.

(II) Tin dioxide (SnO_2, >99.9%): the inorganic compound target with diameter 2" and 0.25" in thickness was purchased from Stanford Advanced Materials. The white circular target was used as the seed layer for further hydrothermal synthesis.

(III) Silicon (Si, (100)): substrates (boron doped, p-type, 1~10 ohm-cm, 100 mm in diameters, 500 μm in thickness, single flat, single side polish) topped with 1μm silicon dioxide (SiO_2) were purchased from University Wafer.

(IV) Dihydrogen hexachloroplatinate(IV) hydrate ($H_2PtCl_6 \cdot 6H_2O$, 99.99%): The red-brown crystalline powder was used as a precursor of the Pt nanoparticles and purchased from Alfa Aesar.

(V) Sodium hydroxide (NaOH, >97.0%): The white solid pellets were used to tune the pH value of glycol solution for the preparation of Pt nanoparticle and bought from Fisher Scientific.

(VI) Ethylene glycol ($C_2H_6O_2$, certified): The transparent and colorless solution was used for the preparation of Pt nanoparticles and purchased from Fisher Scientific.

(VII) Lanthanum strontium iron oxide ($La_{0.8}Sr_{0.2}FeO_3$, 99.99%): This perovskite material was used as the target of radio-frequency magnetron sputtering to decorate the surface of β-Ga_2O_3 nanorods and purchased from Kurt J. Lesker Co..

(VIII) Deionized Water (DI Water): it's used as solvent for hydrothermal method and to clean the sample after the growth process.

(IX) Wipers: Kimwipes were used as the wipers and purchased from Kimberly-Clark.

4.2.2: Preparation of Ga_2O_3 Nanorod Arrays and Surface Decoration of Pt & $La_{0.8}Sr_{0.2}FeO_3$ Nanoparticles

First we grow β-Ga_2O_3 nanorod arrays by combining a hydrothermal method and high temperature calcination. A Si (100) wafer with 1 μm SiO_2 insulator layer is used as a substrate. To remove surface grease and organic deposits, the Si/SiO_2 substrates were immersed in acetone solution and sonicated for 5 minutes. A 50 nm thick tin dioxide (SnO_2) film was sputter-coated as a seed layer followed by post-deposition ambient-annealing at 900 °C for 2 hours in order to make it crystalline. A $Ga(NO_3)_3$ solution was

prepared by dissolving 0.6 g $Ga(NO_3)_3 \cdot 9H_2O$ in 40 mL deionized (DI) water, with the pH of solution controlled at ~2. The SnO_2-coated substrates were then incubated in $Ga(NO_3)_3$ solution at 150 °C for 12 hours for the hydrothermal growth of the intermediate products, vertically aligned gallium hydroxide (GaOOH) nanorod arrays. After the growth, GaOOH nanorod arrays were washed by DI water, dried overnight in air at 80 °C, and finally subjected to annealing at 1000 °C for 4 hours to be converted into pure β-Ga_2O_3 nanorod arrays. To prepare Pt nanoparticles, a glycol solution of NaOH (50 mL, 0.5M) was added into a glycol solution of $H_2PtCl_6 \cdot 6H_2O$ (1.0 g, 1.93 mmol in 50 mL) via stirring to obtain a transparent yellow platinum hydroxide or oxide colloidal solution. The solution was then heated at 160 °C for 3 hours, with a N_2 flow passing through the reaction system to take away water and organic byproducts, finally yielding a transparent dark-brown homogeneous colloidal solution of the Pt metal nanocluster without any precipitates. Pt nanoparticles were dip-coated with a control of ~3.0 wt. % loading on the β-Ga_2O_3 nanorod arrays, followed by a post heat-treatment at 450 °C for 2 hours in order to remove the surface residual glycol ligands. The decoration of LSFO nanoparticles on Ga_2O_3 nanorod arrays was achieved by depositing LSFO (nominal thickness of 5-10 nm, monitored by a quartz microbalance) on β-Ga_2O_3 nanorod arrays by radio-frequency (RF) magnetron sputtering followed by post-annealing to improve the crystallinity of LSFO nanoparticles.

4.2.3: Gas Sensing Test Setup and Installation of the Device

The resistor-type β-Ga_2O_3-based nanorod arrays were installed on an Al_2O_3 ceramic holder, shown in **Figure 4-1**. Two Pt wires, with the thickness of 10 mm, were used as

two electrodes and Pt wires were tightly tied into the substrate holder which consists of upper and down bulk Al_2O_3 ceramics. The β-Ga_2O_3-based nanorod arrays were kept in the center of the ceramic holder and exposure area with size dimensions of 1 centimeter x 0.5 centimeter is acted as sensing area.

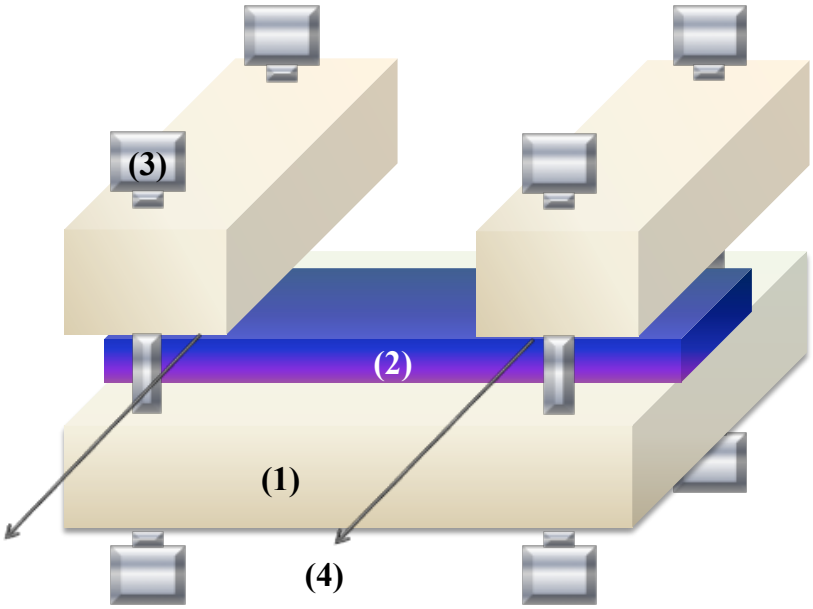

Figure 4-1: Schematic illustration of a typical Ga_2O_3 nanorod array sensor testing setup. (1) Alumina holder, (2) Ga_2O_3-based nanorod array gas sensor fabricated on Si substrate. 3) ceramic screw and (4) platinum wires.

The sensor device placed in the center of a tube furnace equipped with a temperature controller was connected to a CHI 660D electrochemical analyzer (CH Instruments Inc., USA) through two long Ni-Cr alloy wires which acts and electrodes and were embedded into a alumina tube to conduct *in-situ* temperature gas sensing tests.

The high-temperature gas sensing properties of β-Ga_2O_3 nanorod arrays were then tested by monitoring the potentiostatic current response of the β-Ga_2O_3 nanorod array device to carbon monoxide (CO) exposure in a high temperature tube furnace equipped with an

alumina tube, electrical feedthroughs (Ni/Cr lead wires), and a gas injection system, shown in **Figure 4-2**.

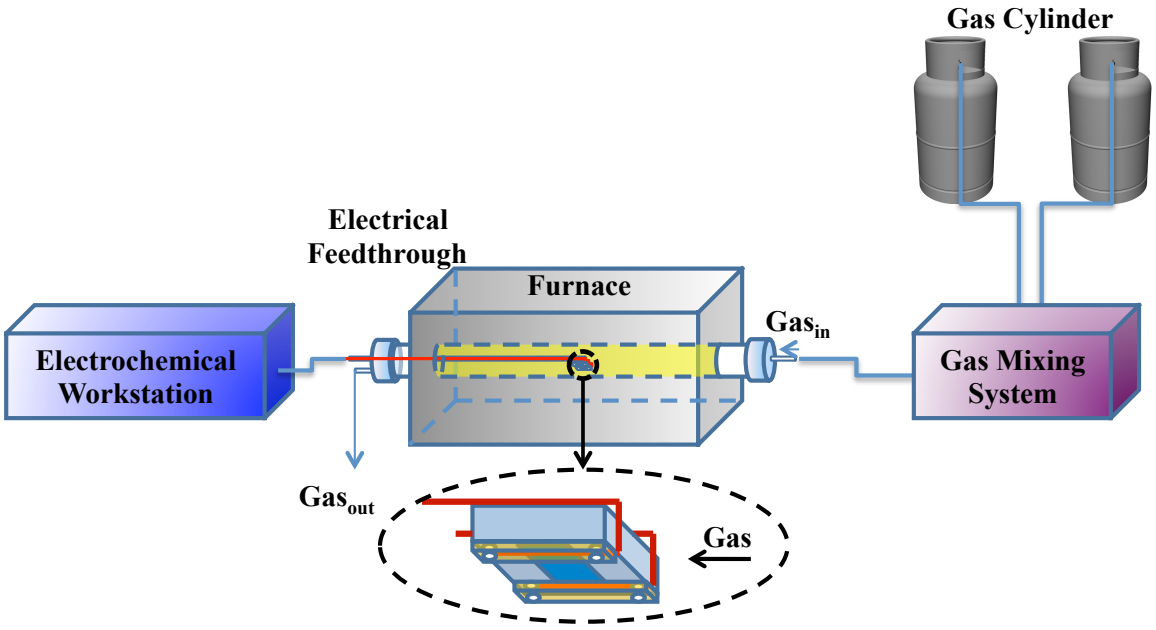

Figure 4-2: The setup of gas sensing test system, including gas cylinders, gas mixing system, furnace, gas inlet/outlet, sample holder and electrochemical workstation.

The nanorod sensor was subjected to a fixed 1 volt direct current (DC) bias while being heated from room temperature to 500 °C in air with a ramp rate of 20 °C/min. Gas sensing tests were then performed at 500 °C under varying concentration of CO (N_2 balance; from 20, 50, 80, to 100 ppm; total chamber pressure 1 atmosphere). The responses of the nanorod sensor to CO were evaluated by measuring the magnitude of current change upon the exposure to various concentrations of CO under a dynamic gas flow condition with a constant flow rate of 1.5 L/min (with high purity N_2 as carrier gas), which was regulated by a computer-controlled gas mixing system (S-4000, Environics Inc., USA). The desired CO concentrations can be achieved by a 2 % CO cylinder connected to one port of the system and diluted by a pure N_2 cylinder connected in

another port of the gas mixing system. In detail, the nanorod sensor device was first exposed to CO/N_2 mixture for 16 min, followed by high purity N_2 purge for 24 minutes (i.e., one gas exposure cycle) to recover the sensor, and then multiple exposure cycles were repeated. We define the device gas sensitivity as: (R_0/R_{CO}) -1, where R_{CO} is the resistance under CO/N_2 mixture and R_0 is the resistance under high purity N_2. The response time is defined as 'the time duration required for gas sensitivity to reach 90 % upon exposure of a sensor to CO', and recovery is defined as 'the time duration required for the gas sensitivity to decrease to 10 % of the sensitivity upon the termination of CO injection'.

4.3: Results and Discussion

X-ray diffraction (XRD) analysis successfully resolved the crystal phases of intermediate GaOOH and final β-Ga_2O_3 nanorods before and after Pt or LSFO nanoparticle surface decoration (**Figure 4-3**). As shown in **Figure 4-3(a)**, most of the peaks in the GaOOH XRD spectrum are assigned to orthorhombic GaOOH phase (JCPDS #06-0180), with a preferred growth orientation perpendicular to (111) plane, instead of (110) plane typically observed in GaOOH powder.[30, 31] Strongly *c*-axis-oriented GaOOH nanorods were deposited by the hydrothermal method. Heterogeneous nucleation of GaOOH was efficiently induced on crystalline SnO_2 seed layers and further annealing converted the GaOOH nanorods to Ga_2O_3 nanorods without structural disintegration.[32] Minor peaks present in the spectrum are originating from the underlying SnO_2 seed layer. After postgrowth annealing at 1000 °C for 4 hours, the GaOOH phase is completely converted to monoclinic β-Ga_2O_3 (JCPDS # 41-1103) as shown in **Figure 4-**

3(b). These β-Ga_2O_3 nanorod arrays have a preferred growth orientation perpendicular to (111) plane of the monoclinic structure. The XRD spectrum of Pt-coated β-Ga_2O_3 (**Figure 4-3(c)**) displays no clear peaks corresponding to Pt due to its much smaller amount than Ga_2O_3. Similarly, the LSFO-nanoparticle-decorated β-Ga_2O_3 nanorod array does not display peaks corresponding to the LSFO perovskite, other than apparent Ga_2O_3 peaks (**Figure 4-3(d)**).

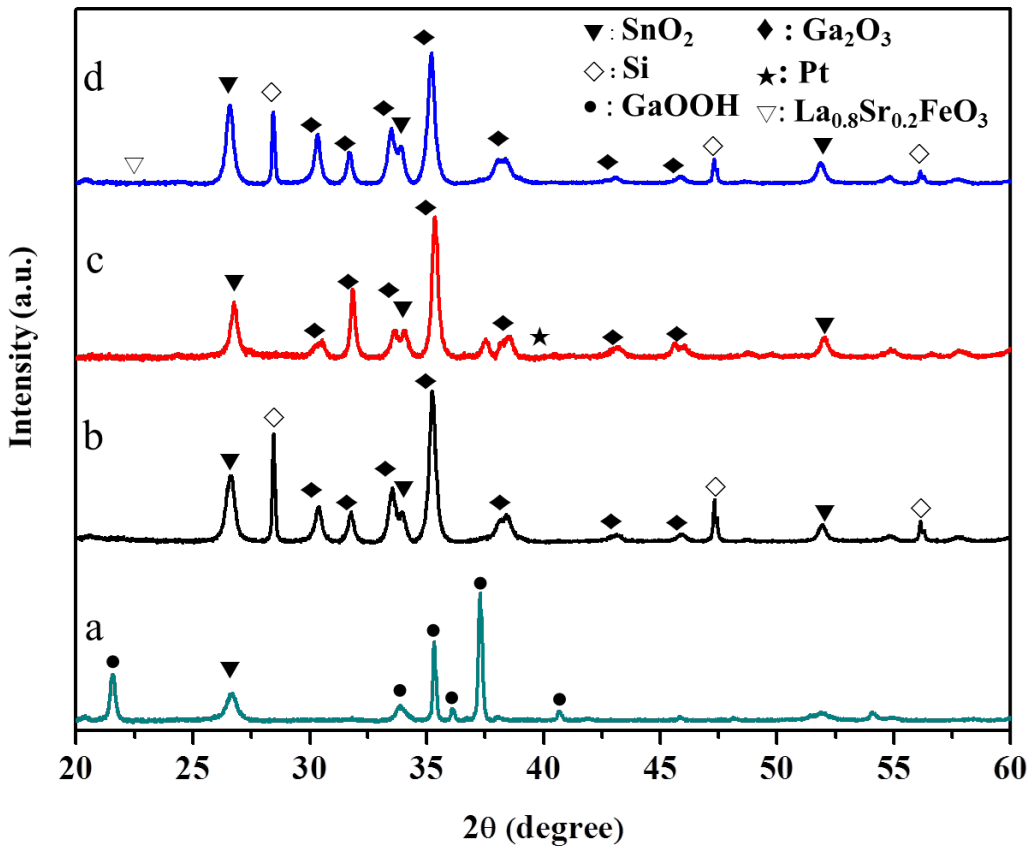

Figure 4-3: X-ray diffraction (XRD) patterns of (a) GaOOH nanorod arrays, (b) β-Ga_2O_3 nanorod arrays, (c) β-Ga_2O_3/Pt particles nanorod arrays, (d) β-Ga_2O_3/LSFO nanorod arrays.

From SEM, we find that the grown vertical nanorod arrays have diameters of ~100-300 nm and lengths up to ~2 μm. **Figure 4-4(a)** shows a representative top-view SEM

micrograph of as-synthesized GaOOH nanorods grown on the Si(100) substrate.. The 45°-tilted view of as-grown GaOOH nanorod arrays (**Figure 4-4(b)**) shows a well aligned vertical structure, while the energy dispersive X-ray spectra (EDXS) confirm the presence of Ga and O from the nanorods and Si from the underlying Si substrate (**Figure 4-4(c)**). From the cross-sectional view of growth substrate (**Figure 4-4(d)**), the length of vertical GaOOH nanorod arrays was determined to be ~1.8 μm. After thermal annealing at 1000 °C for 4 hours, the converted pure Ga_2O_3 phase retained the diamond-shaped tips, which were not affected by the following Pt or LSFO nanoparticle decoration (**Figures 4-4(f)** and **(g)**).

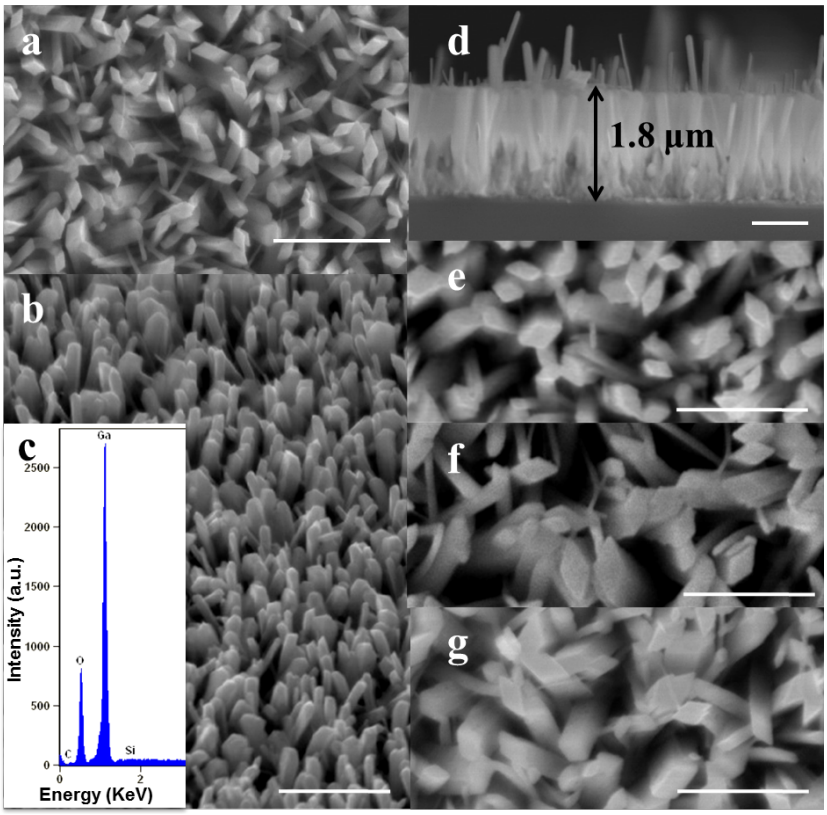

Figure 4-4: Top view (a) and 45° tilt view (b) SEM images of GaOOH nanowires grown at 150°C. (c) the corresponding GaOOH Energy-dispersive X-ray (EDX) spectrum. (d) A cross-sectional view SEM image of GaOOH nanorod array. (e) A top view SEM image of the β-Ga_2O_3 nanorods from GaOOH nanorods annealed at 1000 °C for 4hrs, and coated with LSFO (f) and with Pt particles (g). All scale bars are 1 µm.

The tips of the nanorods reveal diamond-shaped cross sections with diagonal lengths of 150~350 nm, the ratio of short diagonal length to long diagonal length is about 0.5, originating from its orthorhombic crystal symmetry discussed in Chapter 3. In addition, the average diagonal length of each sample is similar, which is shown in **Figure 4-5**.

We randomly choose twenty nanorods of β-Ga_2O_3, LSFO/Ga_2O_3 and Pt/Ga_2O_3 with diamond tip up and record the short/long diagonal lengths, shown in **Figure 4-5(b)**, **(c)** and **(d)** respectively. Compare with all three samples, the short diagonal lengths of the

diamond shape tip top of β-Ga_2O_3, LSFO/Ga_2O_3 and Pt/Ga_2O_3 nanorods are around 173.75 ± 21.09, 173.33 ± 21.09, and 181.58 ±17.61 nm, respectively; the long diagonal lengths of β-Ga_2O_3, LSFO/Ga_2O_3 and Pt/Ga_2O_3 nanorods are around 320.22 ± 34.2, 328.67 ± 24.24, and 331 ± 28.3 nm, respectively. **Figure 4-5(a)** and **(e)** shows the comparison of short and long diagonal lengths of each type and the difference of short and long diagonal lengths of each type are small. Therefore, for the sensing performance which will be discussed in the next section, the diameter or the diagonal length of the nanorods doesn't influence much.

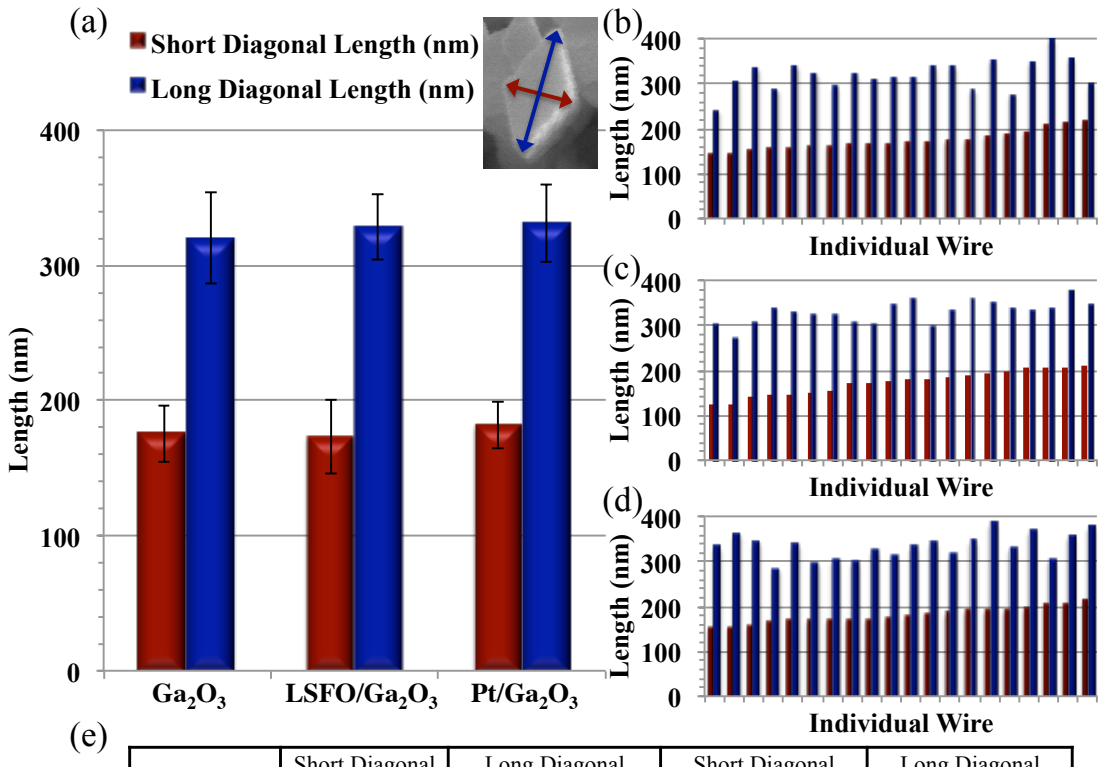

(e)

	Short Diagonal Length (nm)	Long Diagonal Length (nm)	Short Diagonal Length S.D.(nm)	Long Diagonal Length S.D.(nm)
Ga_2O_3	175.75	320.22	21.09	34.2
LSFO/Ga_2O_3	173.33	328.67	27.76	24.24
Pt/Ga_2O_3	181.58	331	17.61	28.3

Figure 4-5: (a) Comparison of short and long diagonal lengths of the diamond shape tips of β-Ga_2O_3, LSFO/Ga_2O_3 and Pt/Ga_2O_3 nanorod arrays and the corresponding detail lengths of randomly picked nanorods were shown in (b), (c) and (d), respectively. (d) The table of the calculated short and long lengths of each type. The inset in (a) reveals a diamond-shape of a GaOOH nanorod tip.

The composition analyses were also conducted from ICP. **Figure 4-6** shows the results that the Pt nanoparticles was of a loading of ~3.39 wt. % on β-Ga_2O_3 nanorod arrays (**Figure 4-6(a)**), while 5 nm LSFO nanoparticle decoration led to ~0.61 wt.% loading on β-Ga_2O_3 nanorod arrays (**Figure 4-6(b)**), which suggested 10 nm LSFO nanoparticle decoration would result in ~1.22 wt. % loading, ~30 % of Pt loading amount. Besides, the weight composition of LSFO is La: 55.17 %, Sr: 6.89 % and Fe 37.93 %, very close to

the original comparative composition of $La_{0.8}Sr_{0.2}FeO_3$, La: 60.23 %, Sr: 9.49 % and Fe: 30.27 %.

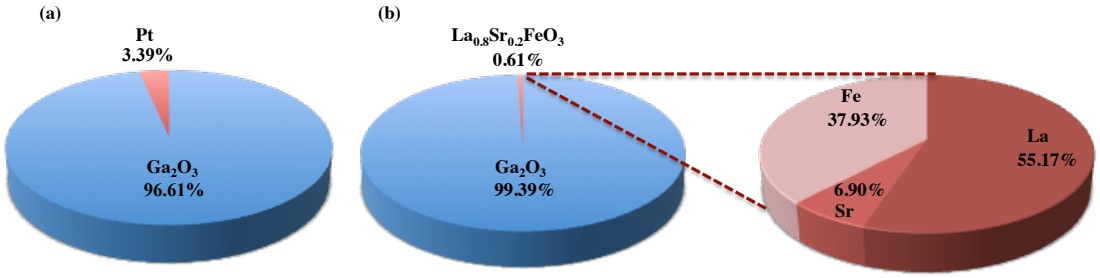

Figure 4-6: The ICP-MS composition analyses results of (a) 2 wt. % Pt on Ga_2O_3 nanorod arrays, (b) 5 nm LSFO/Ga_2O_3 nanorod arrays.

The low-magnification bright-field TEM combined with SAED analysis provide further structural details of grown nanorods and nanoparticle surface decoration. The as-synthesized GaOOH nanorod, with smooth side walls, has single-crystalline orthorhombic crystal structure (lattice constants a = 4.58 Å, b = 9.8 Å, c = 2.97Å; α = 90°, β = 90°, γ = 90°) and growth orientation perpendicular to the (111) plane (**Figure 4-7(a)**). The Ga_2O_3 nanorod converted from GaOOH on the other hand has seemingly roughened surfaces as the bright-field TEM micrograph features local variation in contrast, which is generally resulting from the density variation (**Figure 4-7(b)**). The porous β-Ga_2O_3 nanorod is however textured with monoclinic structure (a = 12.22 Å; b = 3.038 Å; c = 5.807 Å; α = 90°, β = 103.82°, γ = 90°) with a growth orientation normal to (001) plane as confirmed by SAED analysis (**Figure 4-7(b)** inset). The perovskite LSFO-nanoparticle decoration by sputter deposition yields sparsely distributed LSFO

nanoparticles of <10 nm size on the surface of β-Ga_2O_3 nanorod (**Figure 4-7(c)**; no diffraction peaks of LSFO was revealed in the SAED pattern due to its small quantity. Pt nanoparticle decoration on the β-Ga_2O_3 nanorod surface has a more uniform spatial distribution of Pt nanoparticles, which have a mean diameter of ~4 nm (**Figure 4-7(d)**).

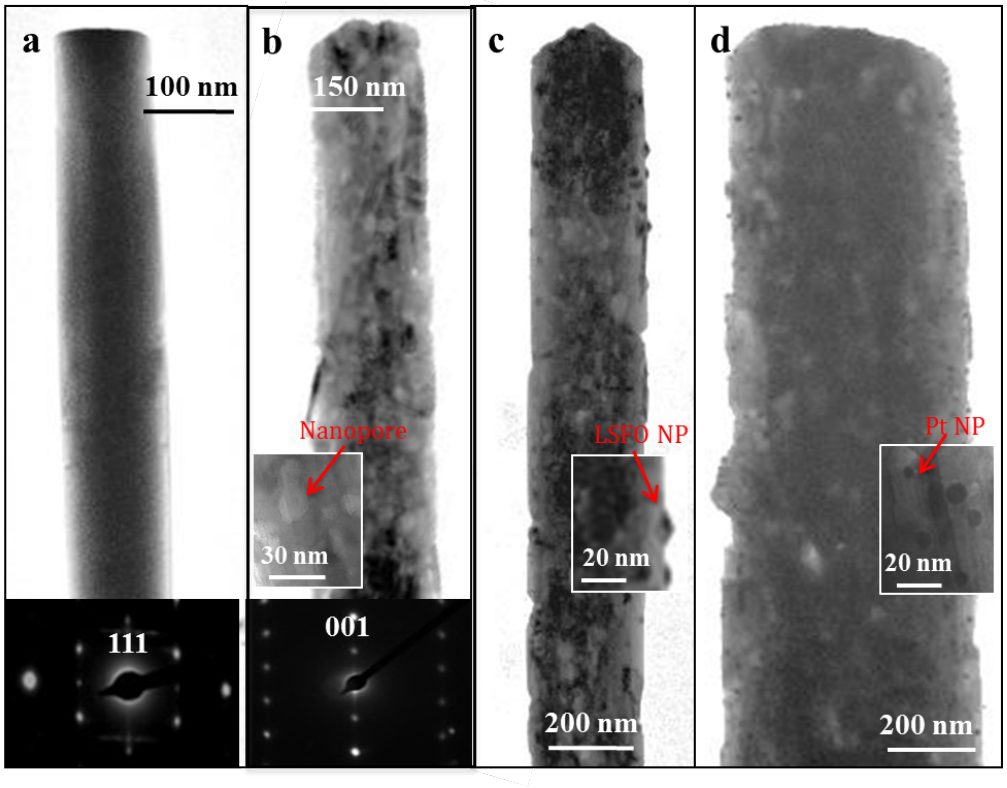

Figure 4-7: (a) TEM image of a GaOOH nanorod grown at 150 °C, and the inset is the corresponding electron diffraction pattern indicating the GaOOH nanorod growth plane is parallel to (111). (b) TEM image of a β-Ga_2O_3 nanorod annealed at 1000 °C for 4 hours, and the inset is the corresponding electron diffraction pattern indicating the growth plane is parallel to (001). (c) TEM image of postannealing β-Ga_2O_3 coated with LSFO 5 nm, and inset is the electron diffraction pattern corresponding to the nanowire in (c), which shows the preferred growth plane of β-Ga_2O_3 nanorod is (001). (d) TEM image of postannealing β-Ga_2O_3 coated with Pt particles.

A more detailed examination by STEM reveals that the contrast variation was in fact caused by the porous structure of β-Ga_2O_3 nanorod and the more detailed distribution of LSFO nanoparticles were both provided in **Figure 4-8**.

Based on the results of high-angle annular dark field (HAADF) scanning transmission electron microscope images, the point and line scan of X-ray energy dispersive spectroscopy (EDS) were gained on the high contrast (i.e. bright) position. In modified **Figure 4-8**, **(a)**,**(c)**, and **(e)** present the typical HAADF STEM images of LSFO decorated porous β-Ga_2O_3 nanorods and their corresponding EDS spectra were shown in **(b)**,**(d)**, and **(f)**, respectively. The point probing EDS spectrum revealed the existence of LSFO on β-Ga_2O_3 nanord and line scanning EDS spectra show the uneven distribution of LSFO across β-Ga_2O_3 nanorod due to the sputtering shadow effect (**Figures 4-8 (d)** and **(f)**).

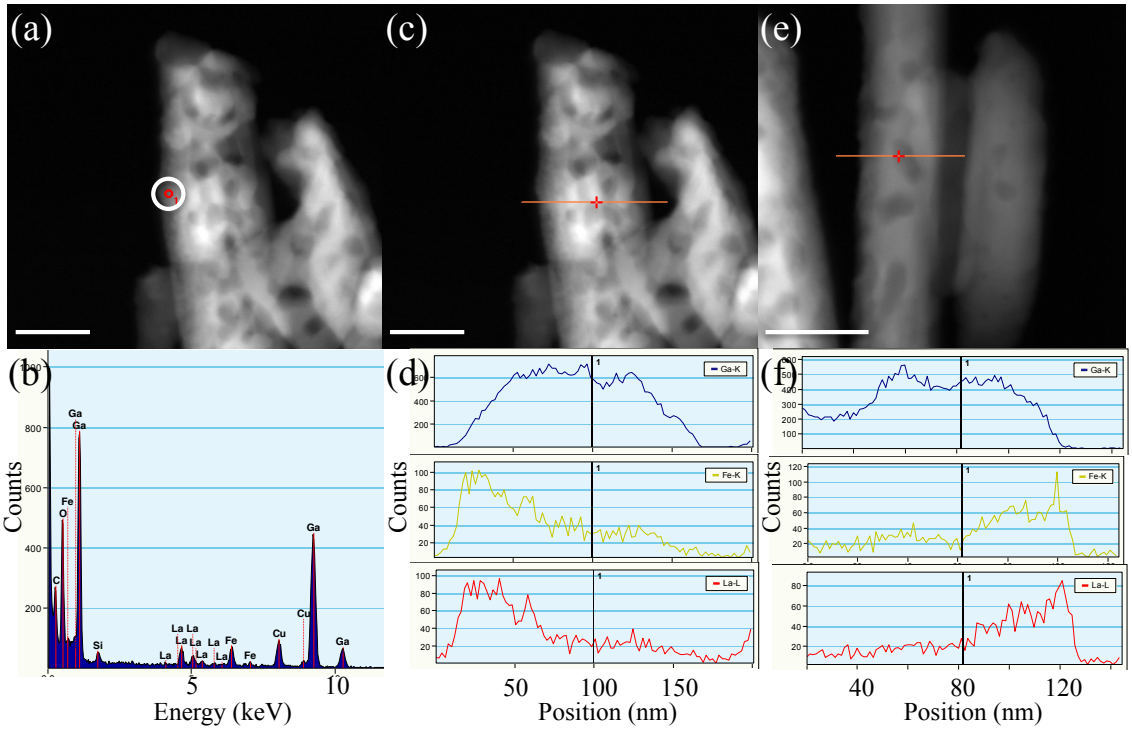

Figure 4-8: (a), (c), and (e) Typical HAADF STEM images of LSFO decorated β-Ga_2O_3 nanorods showing their porous structure; the corresponding EDS spectra from (b) point scanning, (d) and (e) line scanning revealing the existence and distribution of LSFO composition on β-Ga_2O_3 nanorods. The scale bar is 100 nm.

We find that the LSFO nanoparticle decoration has an excellent gas sensing catalytic performance on β-Ga_2O_3 nanorods, comparable to that of Pt nanoparticle decoration. We tested the high-temperature (500 °C) CO gas sensing properties of β-Ga_2O_3 nanord arrays with three different surface conditions: pristine, Pt-nanoparticle-decorated, and LSFO-nanoparticle-decorated (5 nm or 10 nm nominal film thicknesses). **Figure 4-9(a)** shows the dynamic sensing characteristics of the above materials to four different CO gas concentrations (20, 50, 80, and 100 ppm in N_2 balance), where CO sensitivity in general increases for higher CO concentrations, regardless of the type of sample. While the pristine Ga_2O_3 nanorod array shows a base sensitivity ~8 at 100 ppm of CO exposure, the

sensitivity of 10 nm-LSFO-nanoparticle-decorated sample exceeds ~70 at the same CO concentration. This is approaching the sensitivity performance of Pt-nanoparticle-decorated Ga_2O_3 nanorod (sensitivity ~95 at 100 ppm CO). In fact, at lower CO concentrations, sensing performances of 10 nm LSFO and Pt nanoparticles are nearly identical (**Figure 4-9(b)**). Meanwhile, 5 nm LSFO nanoparticle decoration has a decreased sensitivity by < ~30 % compared with 10 nm LSFO nanoparticle decoration, which most likely results from smaller nanoparticle surface coverage, as seen in **Figure 4-8**, which revealed the sparse distribution of LSFO nanoparticles on Ga_2O_3 nanorods.

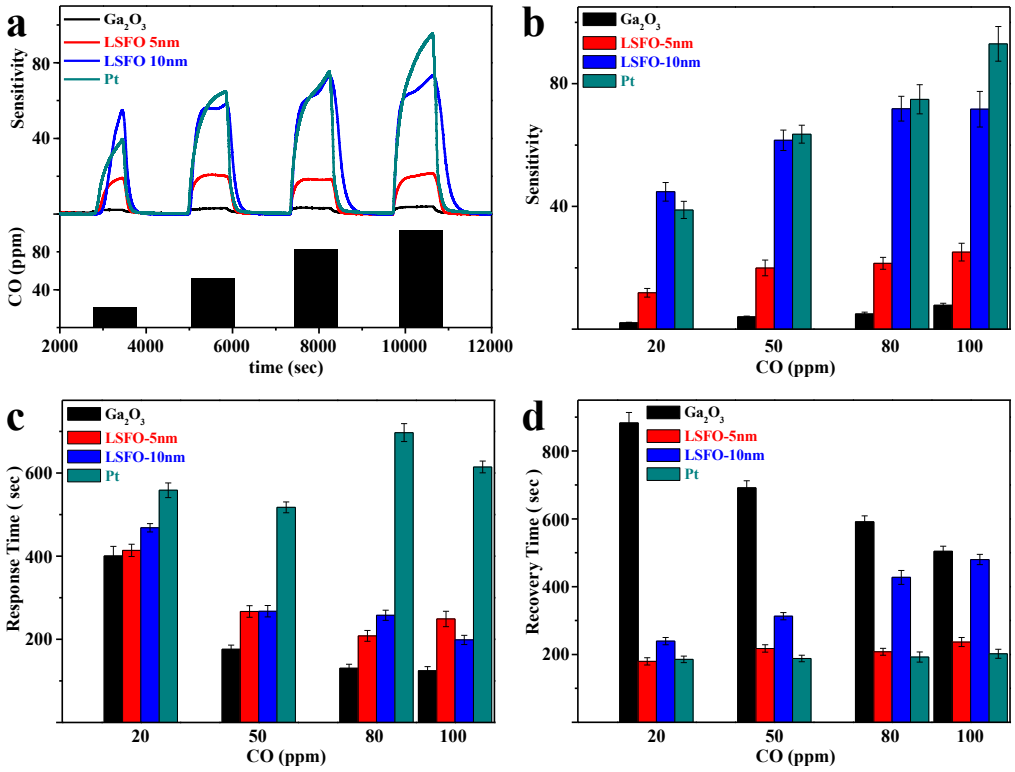

Figure 4-9: Carbon monoxide gas sensing test results: (a) Current-time characteristics of β-Ga_2O_3; β-Ga_2O_3/LSFO 5 nm; β-Ga_2O_3/LSFO 10 nm; β-Ga_2O_3/Pt composite nanorod tested at 500 °C with N_2 as background atmosphere; (b) Sensitivity versus CO concentrations characteristics of β-Ga_2O_3; β-Ga_2O_3/LSFO; β-Ga_2O_3/Pt composite nanorod tested at 500 °C; (c) Response Time versus CO concentrations characteristics of β-Ga_2O_3; β-Ga_2O_3/LSFO; β-Ga_2O_3/Pt composite nanorod tested at 500 °C; (d) Recovery Time versus CO concentrations characteristics of β-Ga_2O_3; β-Ga_2O_3/LSFO; β-Ga_2O_3/Pt composite nanorod tested at 500 °C.

In addition to the excellent CO sensitivity, the LSFO-nanoparticle-decorated Ga_2O_3 nanorod array has a faster response time to a given CO exposure than Pt-nanoparticle decoration. For all the examined CO concentrations, the LSFO-nanoparticle decoration has shorter response time than Pt-nanoparticle decoration, while having comparable or slightly longer response times compared with pristine Ga_2O_3 nanorods (**Figure 4-9(c)**). In particular, at the highest CO concentration (100 ppm), LSFO nanoparticle decoration has

a response time of ~200 seconds, ~400 seconds shorter than that for Pt-nanoparticle decoration. Meanwhile, the recovery time of Ga_2O_3 nanorod sensors having LSFO nanoparticle decoration was either comparable or slower (especially for 10 nm-LSFO) than that of Pt nanoparticle decoration (**Figure 4-9(d)**), but faster than that of the pristine Ga_2O_3 sensor.

In order to identify potential mechanisms of high gas-sensing catalytic activity of LSFO nanoparticles, it is useful to examine the general gas sensing principles in Ga_2O_3 and Pt nanoparticle catalysts. Ga_2O_3, due to its wide band gap (4.9 eV), has a relatively high electrical resistance at room temperature. At a sufficiently elevated temperature (500 °C in this case), reactive oxygen species such as O^- and O^{2-} are known to be chemisorbed on the surface of the Ga_2O_3 and, importantly, to experience electron transfer with Ga_2O_3.[4-6] Specifically, these chemisorbed oxygen molecules trap mobile electrons from the conduction band of β-Ga_2O_3, creating charge carrier depletion at the surface. However, different oxygen species are dominant in several temperature ranges, usually O_2^- ions are adsorbed/desorbed at room temperature to ~ 200 °C, while in 200 °C to ~550 °C range O^- ions are dominant and O^{2-} ions exist above 550 °C. Under such a condition, when CO gas molecules are introduced to the Ga_2O_3 surface, CO molecules react with pre-adsorbed oxygen ions via the following reaction paths: [9, 17, 33-35]

$$CO\ (g) + O^-\ (ad) = CO_2(g) + e^-$$

$$CO + 2O^- = CO_3^{2-} = CO_2 + \tfrac{1}{2}O_2 + 2e^-$$

The result is then the release of mobile electrons back to Ga_2O_3, which induces the increase in carrier density in Ga_2O_3 (i.e., decrease in depletion depth) and, ultimately, the apparent current response of the sensor. The process is reversed when CO exposure is

terminated as residual ambient oxygen molecules are rechemisorbed on the surface, resulting in the decrease of current response in Ga_2O_3 back to the original base level (i.e., recovery).

It is worth pointing out that residual ambient oxygen molecules were verified by the residual gas analysis to exist in both ultrahigh purity nitrogen and CO/N_2 flows used in the experiment (**Figure 4-10**). Based on the results of residual gas analysis, we test dynamic partial pressure of CO, N_2 and O_2 in vacuum which in the chamber of RGA, 2 % CO cylinder balance with N_2 and ultra-high purity N_2 cylinder. Partial pressures from CO and N_2 can't be differentiated due to the same molecular weight of CO and N_2. It can be seen partial pressure of CO, N_2 increased when switching to 2 % CO cylinder and keep the same in the ultrahigh purity N_2 cylinder. But drop to low partial pressure when switching back to vacuum. As for oxygen partial pressure, using vacuum created by turbo pump in the test chamber of RGA as a standard, we found the oxygen partial pressure increased in 2 % CO cylinder and increased more in ultrahigh purity N_2 cylinder, shown in **Figure 4-10(a)**. Besides, the spikes in transition I, II came from pressure differences when switching the valve. **Figure 4-10(b)** presents the oxygen partial pressure in vacuum chamber of RGA, CO Cylinder and ultrahigh purity N_2 cylinder, respectively.

Therefore, it can be verified that few oxygen molecules exist in 2% CO cylinder and more oxygen molecules in ultrahigh purity N_2 cylinder. Thus, the residual oxygen molecules would keep provide oxygen anions to the surface of the gas sensor, and lead to the recovery of the sensor.

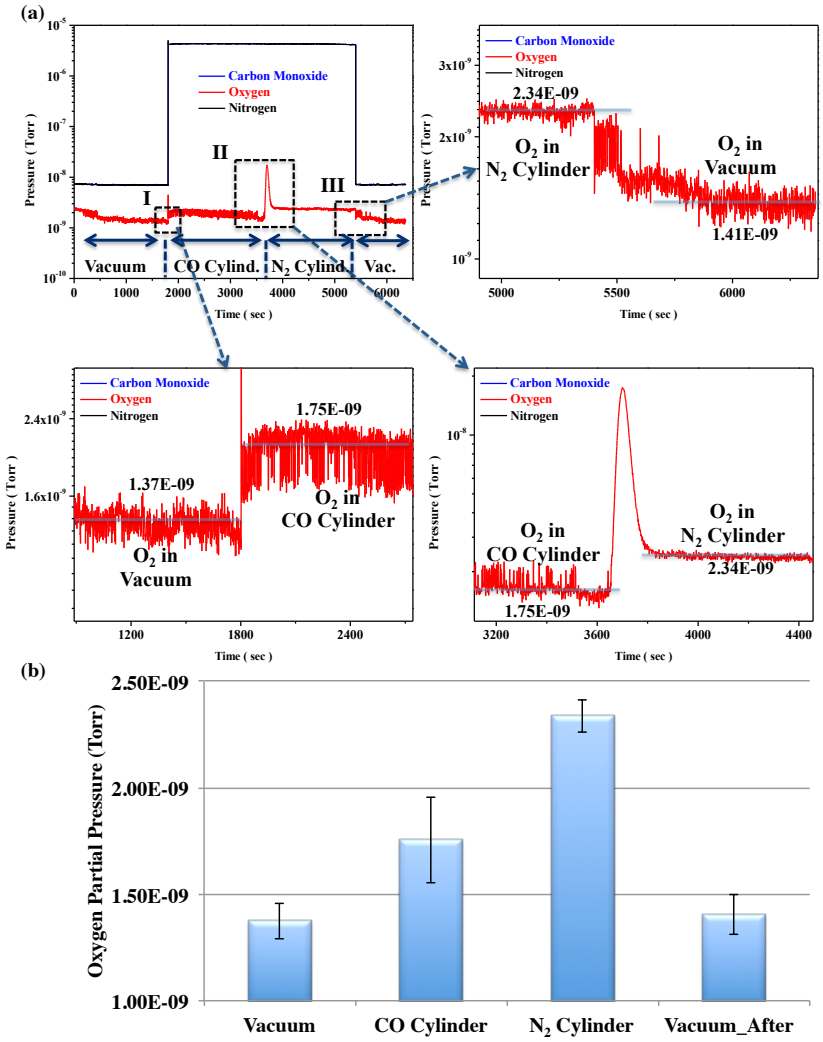

Figure 4-10: Residual gas analysis of (a) dynamic partial pressure of CO, N_2 and O_2 in a sequence of vacuum in the Residual Gas Analyzer chamber, 2 % CO balanced with N_2 and ultra-high purity N_2 cylinder, with each duration time of first three steps ~30 minutes. The index I, II and III depict the transition between vacuum to CO cylinder, CO cylinder to N_2 cylinder and N_2 cylinder to vacuum, respectively. (b) Oxygen partial pressure measured in vacuum, CO/N_2, and ultra-high purity N_2 flow. The spikes in transition I, II came from the transient pressure rises when switching the gas valves.

Although the series of steps generally explain the gas sensing mechanism of the pristine Ga_2O_3 nanorod array, the enhancement of gas sensing performance by the Pt nanoparticle decoration is believed to be originating from, so-called, spillover effects.[17]

In the spillover process, CO molecules are first efficiently adsorbed on the Pt nanoparticles surface and react with preadsorbed oxygen species on the nanorods with reduced activation energy, resulting in an efficient electron back-feeding into the charge depletion layer of Ga_2O_3. In addition, the Pt electric sensitization effect is further enhancing the gas sensing: this is caused by the difference between work function of Pt (5.65 eV)[36] and Fermi level (approximately electron affinity, considering n-type characteristics) of Ga_2O_3 (4.9 eV)[37], which renders the electronic properties of the Ga_2O_3 surface further charge-depleted.

For the observed enhancement of CO sensing performance by LSFO nanoparticle decoration, we find that the spillover effect is one of the likely responsible mechanisms, as supported by XPS analysis of the LSFO-nanoparticle-decorated Ga_2O_3 nanorod array (**Figure 4-11**). XPS analyses performed on the LSFO-nanoparticle-decorated β-Ga_2O_3 nanorod array after 500 °C treatment in CO (20 minutes) show negligible differences in binding energies for Fe 2p, La 3d, and Sr 3d (not shown), compared with the control LSFO-nanoparticle-decorated Ga_2O_3 nanorods treated at 500 °C under pure N_2 (**Figure 4-11(a)**). The lack of evidence for a strong chemical interaction between LSFO nanoparticles and β-Ga_2O_3 nanorods is consistent with the good high-temperature sensing stability as well as the observed fast sensing response of LSFO-nanoparticle-decorated nanorods. Meanwhile, there is a small but nonzero broadening of the O 1s peak; a potential indication of change in electron distribution around oxygen on the LSFO surface upon CO treatment (**Figure 4-11(c)**) which points to the possibility of spillover effects operating on LSFO nanoparticles.

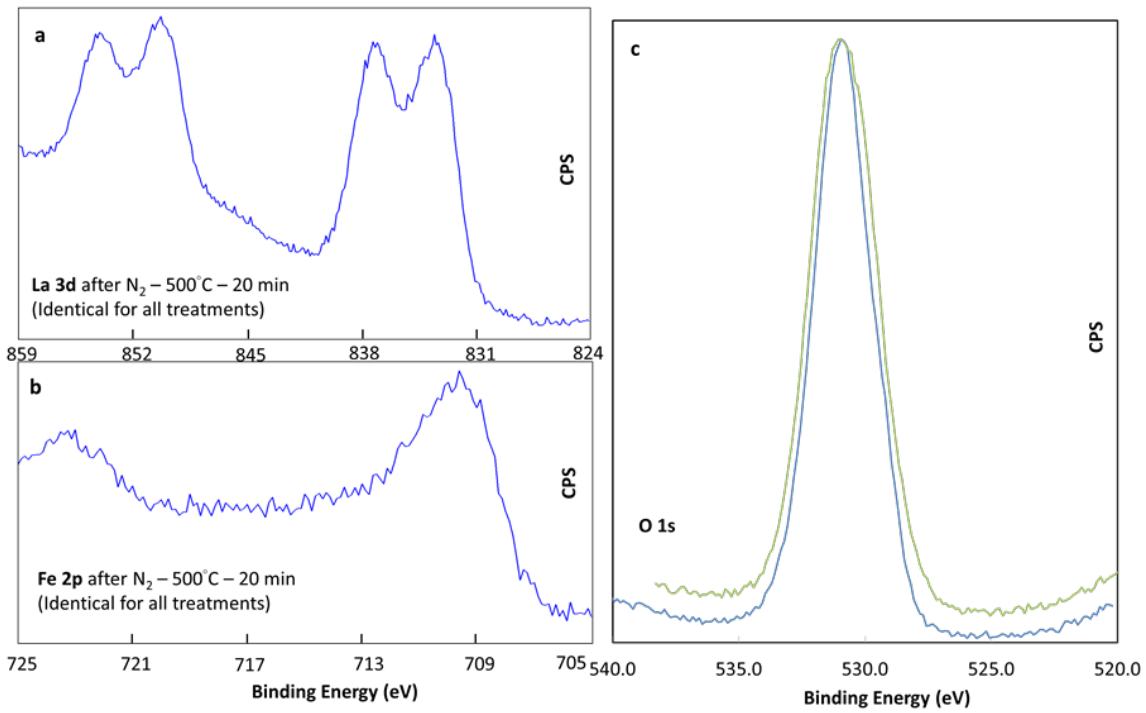

Figure 4-11: X-ray photoemission spectra of (a) La 3d; (b) Fe 2p, and (c) O 1s for LSFO/β-Ga_2O_3.

On the basis of an XPS analysis of Pt-nanoparticle-decorated Ga_2O_3 nanorod arrays exposed to different gas treatments, we believe that the sensing performance enhancement by Pt is related to typical spillover effects,[11-13] while the slow Pt-Ga_2O_3 sensor response we observed may be originating from varying oxidation states of Pt (**Figures 4-12** and **Figure 4-13**).

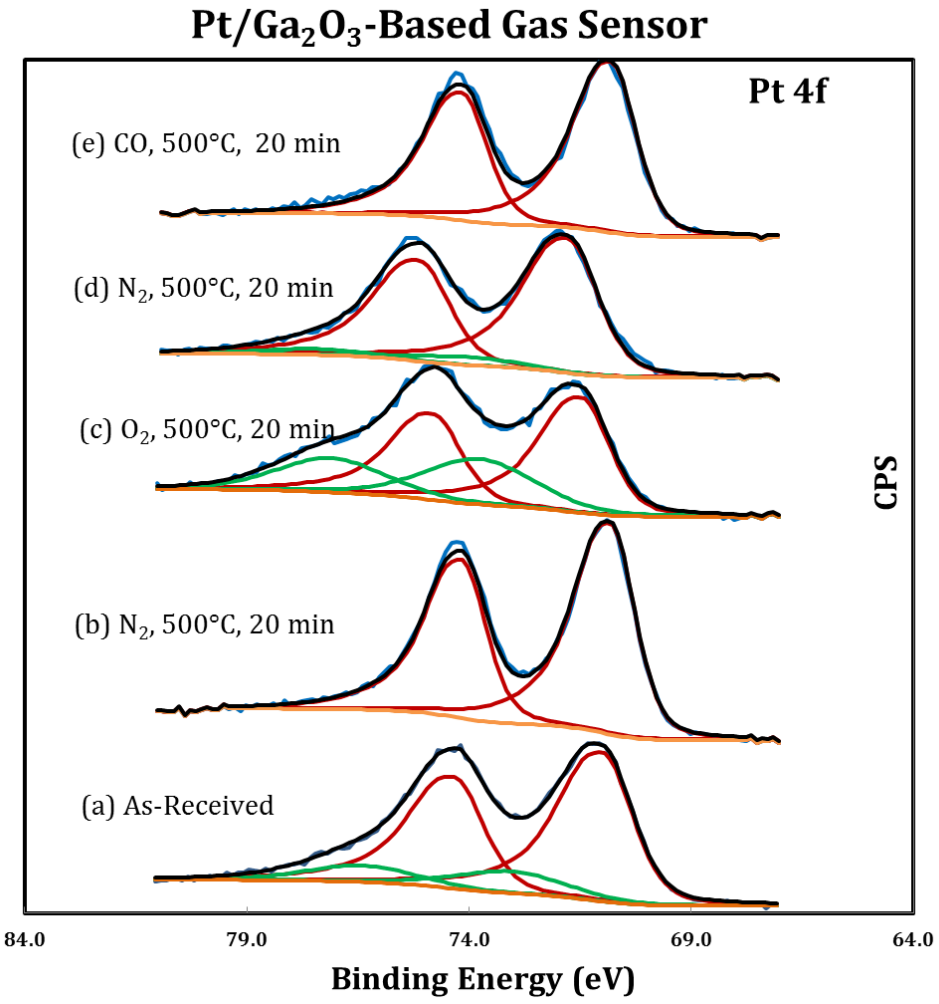

Figure 4-12: Curve-fitted X-ray photoelectron Pt 4f spectra of the Pt-decorated β-Ga_2O_3 samples under different atmospheric treatments. (a) the as-received Pt-decorated β-Ga_2O_3 nanorod array; (b) following pure N_2 treatment for 20 minutes at 500 °C; (c) further treatment with pure O_2 for 20 minutes at 500 °C; (d) N_2 treatment again for 20 minutes after oxygen treatment at 500 °C; (e) treatment with CO for 20 minutes at 500 °C as the last step.

Figure 4-12 depicted the curve-fitted X-ray photoelectron Pt 4f spectra of β-Ga_2O_3 nanorod arrays decorated with Pt nanoparticles under different atmospheric treatments in a sequence of (a) as-received, (b) pure N_2 treatment, (c) pure O_2 treatment, (d) another N_2 treatment and (e) CO treatment. The duration time for each treatment is 20 minutes and XPS was conducted at 500 °C. The binding energies of Pt $4f_{7/2}$ under various gas

treatments were recorded in **Figure 4-13**. The results verified different oxidation states of Pt can be found under different gas treatments at 500 °C.

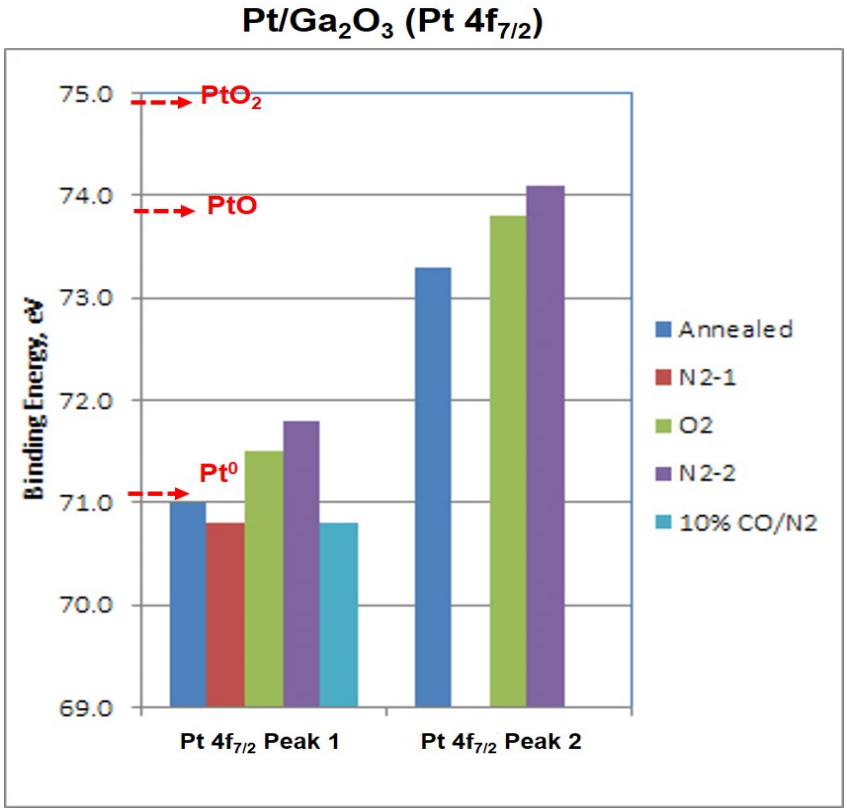

Figure 4-13: XPS Pt $4f_{7/2}$ binding energies of curve-fitted Pt 4f peak components (see Figure 4-12) for particles decorating β-Ga_2O_3 after various gas treatments. Reference binding energies are shown for various Pt compounds.

In addition to the spillover effect, the LSFO-nanoparticle sensitization may be also contributed to by the space-charge effect generally observed in metal oxide sensor systems.[35] Similar to the electric sensitization by Pt on Ga_2O_3, LSFO can generate a charge depletion layer on the Ga_2O_3 nanorod surface upon contact due to the difference in Fermi levels and resulting spontaneous charge transfer (**Figure 4-14(a)**). When a reducing CO gas is introduced, the surface depletion layer becomes thinner, increasing the overall electrical conductance of the nanorod (**Figure 4-14(b)**).

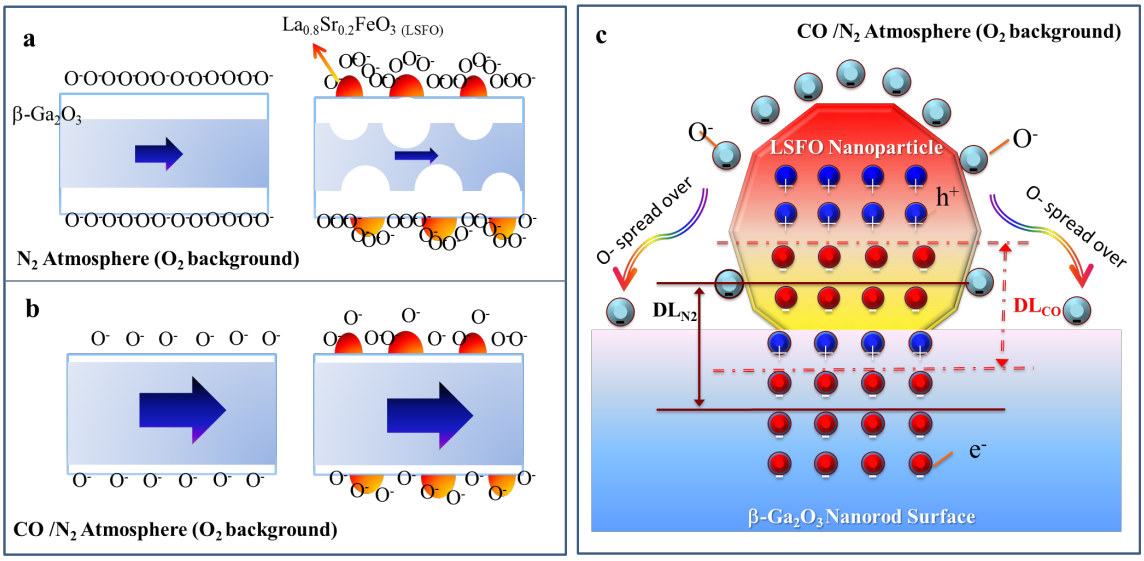

Figure 4-14: Gas sensing enhancing mechanism. (a) β-Ga_2O_3 and LSFO decorated β-Ga_2O_3 nanorods in N_2 atmosphere. (b) β-Ga_2O_3 and LSFO decorated β-Ga_2O_3 nanorods in CO/N_2 atmosphere. (c) spillover like effect model in LSFO nanoparticle decorated β-Ga_2O_3 nanorod surface in CO/N_2 atmosphere, DL: carrier depletion layer.

We note that there are many potential material properties that can also affect the observed sensitization, such as surface states, oxygen vacancies, and interfaces between LSFO nanoparticles and the Ga_2O_3 nanorod, which can act as adsorption sites for the CO gas molecules.[38, 39] Also, LSFO itself might have an active sensing functionality, but this possibility is thought to be minimal based upon the little or negligible CO sensing response at the 20-100 ppm CO concentration range we observe for continuous LSFO thin films (**Figure 4-15(a)**).

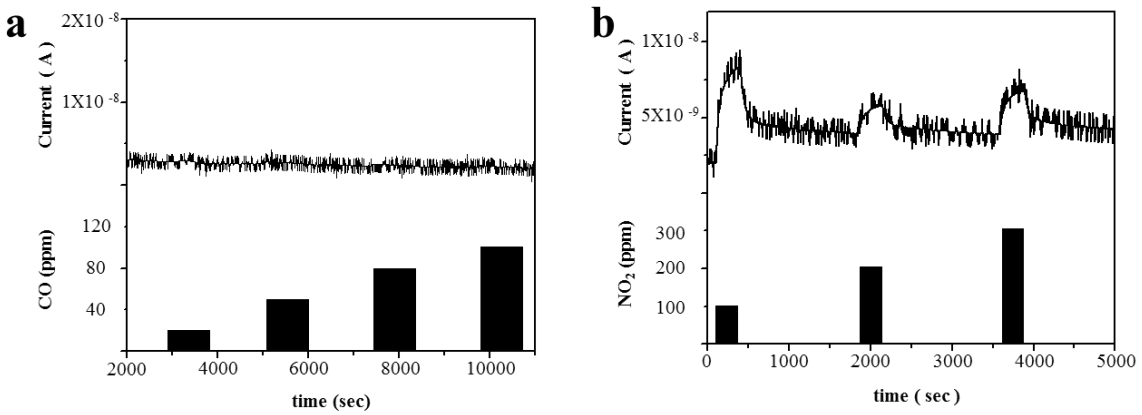

Figure 4-15: $La_{0.8}Sr_{0.2}FeO_3$ thin film gas sensing characteristics. (a) Current-time characteristic of CO gas sensing test results tested under a bias of 1 V at 500 °C with N_2 as background atmosphere; lower bar chart shows the gas concentration of CO/N_2; (b) Current-time characteristic of NO_2 gas sensing test results tested under a bias of 1 V at 500 °C with N_2 as background atmosphere; lower bar graph shows the gas concentration of NO_2/N_2.

Figure 4-15(b) revealed the good sensitivity of LSFO thin films for the oxidative gas NO_2 with increased current observed upon exposure, a *p*-type semiconductor characteristic. Therefore, a *p-n* junction is formed between LSFO and Ga_2O_3. Due to its surface dominant nature, it is possible the built-in-potential of this *p-n* junction may regulate the electrons and holes involved in surface conduction upon gas exposures. The gas-LSFO-Ga_2O_3 triple-interface may function as a sink that attracts negatively charged surface oxygen species such as O^- from the LSFO nanoparticle surface causing it to spread over to the Ga_2O_3 nanorod surface (**Figure 4-14(c)**) as indicated by the surface reactions described earlier. Meanwhile, the insensitive response of LSFO film upon CO exposure indicates the slow or negligible reactions between O^- and CO on LSFO surfaces, which enables the formation of a concentration gradient driving the spread of less-consumed LSFO surface oxygen ions toward the LSFO/Ga_2O_3 interfaces and Ga_2O_3 nanorod surfaces. On the other hand, the resulting populated oxygen dissociation events

and therefore surface oxygen species on LSFO nanoparticle surfaces may contribute to the shorter response time in LSFO-Ga_2O_3 nanorod sensors than Pt decorated ones, besides the possible effect associated with changing surface oxidation states of Pt as revealed in the XPS study. It is worth noting that perovskite-type ABO_3 materials have good lattice oxygen storage capability[38-42] at high temperature directly attributed to their tunable oxygen deficiency. This lattice oxygen may still add to the O^- distribution and the adsorbed residual O_2 species that can enhance recovery upon termination of CO from the gas stream, although at 500 °C bulk defects may play a secondary role on the surface reaction dynamics compared to the surface defects.

4.4: Conclusion

In summary, large scale LSFO-nanoparticle-modified Ga_2O_3 vertical nanorod arrays have been successfully fabricated using a two-step synthetic procedure. The structural and CO-sensing characteristics of the pristine, Pt-nanoparticle-, and LSFO-nanoparticle-modified β-Ga_2O_3 nanorod arrays show that 10 nm LSFO nanoparticle decoration greatly enhances the high-temperature (500 °C) CO sensitivity of pristine β-Ga_2O_3 nanorod arrays by an order of magnitude, rivaling the sensitizing performance of Pt noble metal nanoparticle catalysts. Further, the decorated LSFO nanoparticles are only accounted for ~10-30 % of that of Pt weight loading on β-Ga_2O_3 nanorod arrays. A 'catalytic spillover' effect is identified in LSFO-Ga_2O_3 nanorod sensors as regulated by the LSFO-Ga_2O_3 *p-n* semiconductor junction. Meanwhile, Pt oxidation state changes and surface oxygen ion populating sites of LSFO may help to enable the faster CO sensing response for LSFO decorated nanorod sensors than that for Pt decorated sensors. The demonstrated

perovskite LSFO-nanoparticle-modified Ga_2O_3 nanorod represents a promising candidate for high-performance sensor material for high-temperature gas detection.

Reference

1. Miura, N.; Lu, G.; Yamazoe, N., Progress in Mixed-Potential Type Devices Based on Solid Electrolyte for Sensing Redox Gases. *Solid State Ionics* 2000, 136-137, 533-542.
2. Akbar, S.; Dutta, P.; Lee, C., High-Temperature Ceramic Gas Sensors- A Review. *Int. J. Appl. Ceram. Technol.* 2006, 3, 302-311.
3. Shin, T. I.; Lee, H. J.; Song, W. Y.; Kim, S.-W.; Park, M. H.; Yang, C. W.; Yoon, D. H., A Homojunction of Single-Crystalline β-Ga_2O_3 Nanowires and Nanocrystals. *Nanotechnology* 2007, 18, 345305.
4. Bartic, M.; Toyoda, Y.; Baban, C.-I.; Ogita, M., Oxygen Sensitivity in Gallium Oxide Thin Films and Single Crystals at High Temperatures. *Jpn. J. Appl. Phys.* 2006, 45, 5186-5188.
5. Bartic, M.; Baban, C.-I.; Suzuki, H.; Ogita, M.; Isai, M., β-Gallium Oxide as Oxygen Gas Sensors at a High Temperature. *J. Am. Ceram. Soc.* 2007, 90, 2879-2884.
6. Baban, C.-I.; Toyoda, Y.; Ogita, M., High Temperature Oxygen Sensor Using a Pt–Ga_2O_3–Pt Sandwich Structure. *Jpn. J. Appl. Phys.* 2004, 43, 7213-7216.
7. Liu, Z.; Yamazaki, T.; Shen, Y.; Kikuta, T.; Nakatani, N.; Li, Y., O_2 and CO Sensing of Ga_2O_3 Multiple Nanowire Gas Sensors. *Sens. Actuators, B* 2008, 129, 666-670.
8. Huang, X.-J.; Choi, Y.-K., Chemical Sensors Based on Nanostructured Materials. *Sens. Actuators, B* 2007, 122, 659-671.
9. Kolmakov, A.; Zhang, Y.; Cheng, G.; Moskovits, M., Detection of CO and O_2 Using Tin Oxide Nanowire Sensors. *Adv. Mater.* 2003, 15, 997-1000.
10. Wan, Q.; Wang, T. H., Single-Crystalline Sb-Doped SnO_2 Nanowires: Synthesis and Gas Sensor Application. *Chem. Commun.* 2005, 3841-3843.
11. Huang, H.; Tian, S.; Xu, J.; Xie, Z.; Zeng, D.; Chen, D.; Shen, G., Needle-Like Zn-Doped SnO_2 Nanorods with Enhanced Photocatalytic and Gas Sensing Properties. *Nanotechnology* 2012, 23, 105502.
12. Kolmakov, A.; Klenov, D. O.; Lilach, Y.; Stemmer, S.; Moskovits, M., Enhanced Gas Sensing by Individual SnO_2 Nanowires and Nanobelts Functionalized with Pd Catalyst Particles. *Nano Lett.* 2005, 5, 667-673.
13. Jin, C.-H.; Park, S.-H.; Kim, H.-S.; An, S.-Y.; Lee, C.-M., CO Gas-Sensor Based on Pt-Functionalized Mg-Doped ZnO Nanowires. *Bull. Korean Chem. Soc.* 2012, 33, 1993-1997.
14. Daryakenari, A. A.; Apostoluk, A.; Delaunay, J.-J., Effect of Pt Decoration on the Gas Response of ZnO Nanoparticles. *Phys. Status Solidi C* 2013, 10, 1297-1300.
15. Wu, N.; Zhao, M.; Zheng, J.-G.; Jiang, C.; Myers, B.; Li, S.; Chyu, M.; Mao, S. X., Porous CuO–ZnO Nanocomposite for Sensing Electrode of High-Temperature CO Solid-State Electrochemical Sensor. *Nanotechnology* 2005, 16, 2878-2881.

16. Wang, J. X.; Sun, X. W.; Yang, Y.; Kyaw, K. K.; Huang, X. Y.; Yin, J. Z.; Wei, J.; Demir, H. V., Free-Standing ZnO-CuO Composite Nanowire Array Films and Their Gas Sensing Properties. *Nanotechnology* 2011, 22, 325704.
17. Kim, H.; Jin, C.; An, S.; Lee, C., Fabrication and CO Gas-Sensing Properties of Pt-Functionalized Ga_2O_3 Nanowires. *Ceram. Int.* 2012, 38, 3563-3567.
18. Park, S. H.; Kim, S. H.; Park, S. Y.; Lee, C., Synthesis and CO Gas Sensing Properties of Surface-Nitridated Ga_2O_3 Nanowires. *RSC Adv.* 2014, 4, 63402-63407.
19. Jamison, K.; Eisenhauer, J.; Rash, J.; Greenman, M.; Levine, E., Glass Industry Technology Roadmap. *DOE Report* 2002.
20. Garnett, E. C.; Liang, W.; Yang, P., Growth and Electrical Characteristics of Platinum-Nanoparticle-Catalyzed Silicon Nanowires. *Adv. Mater.* 2007, 19, 2946-2950.
21. Wang, Z. L.; Petroski, J. M.; Green, T. C.; El-Sayed, M. A., Shape Transformation and Surface Melting of Cubic and Tetrahedral Platinum Nanocrystals. *J. Phys. Chem. B* 1998, 102, 6145-6151.
22. Yu, R.; Song, H.; Zhang, X.-F.; Yang, P., Thermal Wetting of Platinum Nanocrystals on Silica Surface. *J. Phys. Chem. B* 2005, 109, 6940-6943.
23. Tietz, F.; Arulraj, I.; Zahid, M.; Stover, D., Electrical Conductivity and Thermal Expansion of $La_{0.8}Sr_{0.2}(Mn,Fe,Co)O_{3-\delta}$ Perovskites. *Solid State Ionics* 2006, 177, 1753-1756.
24. Staruch, M.; Gao, H.; Gao, P.-X.; Jain, M., Low-Field Magnetoresistance in $La_{0.67}Sr_{0.33}MnO_3$: ZnO Composite Film. *Adv. Funct. Mater.* 2012, 22, 3591-3595.
25. Guo, Y.; Zhang, Z.; Ren, Z.; Gao, H.; Gao, P.-X., Synthesis, Characterization and CO Oxidation of TiO_2/(La,Sr)MnO_3 Composite Nanorod Array. *Catal. Today* 2012, 184, 178-183.
26. Gao, P.-X.; Shimpi, P.; Gao, H.; Liu, C.; Guo, Y.; Cai, W.; Liao, K.-T.; Wrobel, G.; Zhang, Z.; Ren, Z.; Lin, H.-J., Hierarchical Assembly of Multifunctional Oxide-based Composite Nanostructures for Energy and Environmental Applications. *Int. J. Mol. Sci.* 2012, 13, 7393-7423.
27. Gao, H.; Staruch, M.; Jain, M.; Gao, P.-X.; Shimpi, P.; Guo, Y.; Cai, W.; Lin, H.-J., Structure and Magnetic Properties of Three-Dimensional (La,Sr)MnO_3 Nanofilms on ZnO Nanorod Arrays. *Appl. Phys. Lett.* 2011, 98, 123105.
28. Gao, H.; Cai, W.; Shimpi, P.; Lin, H.-J.; Gao, P.-X., (La,Sr)CoO_3/ZnO Nanofilm–Nanorod Diode Arrays for Photo-Responsive Moisture and Humidity Detection. *J. Phys. D: Appl. Phys.* 2010, 43.
29. Jian, D. L.; Gao, P. X.; Cai, W. J.; Allimi, B.; Alpay, S. P.; Ding, Y.; Wang, Z. L.; Brooks, C., Synthesis, Characterization, and Photocatalytic Properties of ZnO/(La,Sr)CoO_3 Composite Nanorod Arrays. *J. Mater. Chem.* 2009, 2009, 970-975.
30. Zhang, Y. C.; Wu, X.; Hu, X. Y.; Shi, Q. F., A Green Hydrothermal Route to GaOOH Nanorods. *Mater. Lett.* 2007, 61, 1497-1499.
31. Zhang, J.; Liu, Z.; Lin, C.; Lin, J., A Simple Method to Synthesize β-Ga_2O_3 Nanorods and Their Photoluminescence Properties. *J. Cryst. Growth* 2005, 280, 99-106.
32. Fujihara, S.; Shibata, Y.; Hosono, E., Chemical Deposition of Rodlike GaOOH and β-Ga_2O_3 Films Using Simple Aqueous Solutions. *J. Electrochem. Soc.* 2005, 152, C764-C768.
33. Jimenez-Cadena, G.; Riu, J.; Rius, F. X., Gas Sensors Based on Nanostructured Materials. *The Analyst* 2007, 132, 1083-1099.

34. Yamazoe, N.; Sakai, G.; Shimanoe, K., Oxide Semiconductor Gas Sensors. *Catal. Surv. Asia* 2003, 7, 63-75.
35. Barsan, N.; Wermar, U., Conduction Model of Metal Oxide Gas Sensors. *J. Electroceram.* 2001, 7, 143-167.
36. Michaelson, H. B., The Work Function of the Elements and Its Periodicity. *J. Appl. Phys.* 1977, 48, 4729-4723.
37. Cao, C.; Chen, Z.; An, X.; Zhu, H., Growth and Field Emission Properties of Cactus-like Gallium Oxide Nanostructures. *J. Phys. Chem. C* 2008, 112, 95-98.
38. Fan, K.; Qin, H.; Wang, L.; Ju, L.; Hu, J., CO_2 Gas Sensors Based on $La_{1-x}Sr_xFeO_3$ Nanocrystalline Powders. *Sens. Actuators, B* 2013, 177, 265-269.
39. Liu, X.; Hu, J.; Cheng, B.; Qin, H.; Zhao, M.; Yang, C., First-Principles Study of O_2 Adsorption on the $LaFeO_3$ (010) Surface. *Sens. Actuators, B* 2009, 139, 520-526.
40. Fergus, J. W., Perovskite Oxides for Semiconductor-Based Gas Sensors. *Sens. Actuators, B* 2007, 123, 1169.
41. Toan, N. N.; Saukko, S.; Lantto, V., Gas Sensing with Semiconducting Perovskite Oxide $LaFeO_3$. *Phys. B* 2003, 327, 279-282.
42. Lantto, V.; Saukko, S.; Toan, N. N.; Reyes, L. F.; Granqvist, C. G., Gas Sensing with Perovskite-like Oxides Having ABO_3 and BO_3 Structures. *J. Electroceram.* 2004, 13, 721-726.

CHAPTER 5

Perovskite-Nanoparticle-Sensitized Ga_2O_3 Nanorod Arrays for Highly Selective and Sensitive NO_2 Detection over O_2 at High Temperature

Amongst various gaseous pollutants, NO_2 is one of the major hazardous gases originating from fossil fuel combustion in vehicle engines and power plants at high temperature, where *in situ* and real-time gas detection and monitoring solutions are largely limited. In this section, a new type of perovskite-nanoparticle-decorated β-Ga_2O_3-nanorod-array-based high-temperature NO_2 gas sensors has been successfully fabricated. The demonstrated gas sensors are highly sensitive to NO_2 at 800 °C, with excellent reversible and reproducible response characteristics. Through the surface decoration of perovskite-type $La_{0.8}Sr_{0.2}CoO_3$ (LSCO) nanoparticles, the sensitivity of β-Ga_2O_3 nanorod array gas sensors is enhanced by nearly an order of magnitude, along with much faster temporal senor response dynamics. We also observe a remarkable selectivity toward oxidative gases as we demonstrate the differentiation of NO_2 over O_2, by virtue of the bi-fold enhancements in both sensitivity and response time.

5.1: Introduction

Atmospheric air pollution has become a severe environmental problem globally in recent years.[1-3] The main source of contamination is due to emissions of harmful gases from fuel combustion in automobile engines or industrial plants.[4] Suitable gas sensors are thus demanded at high temperature for monitoring combustion and emission processes.[5-8] Meanwhile, *in situ* and real-time gas detection of various forms of nitrous oxides (NO_x),

major pollutants from exhaust gases at temperatures above 600 °C, has been mainly based on either amperometric or mixed-potential type sensors.[9-15] The conductometric (conversely, resistor-type) NO_x sensors however remain very limited despite the advantages of device structure flexibility and operational ease.[16]

The detection and monitoring of NO and NO_2 are usually required in automotive engines and exhaust after-treatment systems.[17-19] The sensors in this case must be able to work at high temperatures above 500 °C considering the typical engine combustion process taking place at high temperatures. Several solid-state NO_x sensors have been reported at temperatures ranging from room temperature to 300 °C[20, 21], up to 500 °C[18, 22, 23]. These reported sensors displayed good NO_2 response at ~200-400 °C, but tend to lose sensitivity or become mal-functional at higher temperatures for monitoring automobile emission control. In addition, the selectivity of these sensors towards NO_2 is not well established. Meanwhile, various strategies can be applied to improve the performance of sensory material, such as doping,[24, 25] surface functionalization,[26-30] and heterojunction.[31-34]Among these, the surface decoration of catalytically active noble metal particles over the active sensor material has been one of the most effective techniques used widely in practice. However, the prohibitive nature of noble metals due to their scarcity as well as their limited high temperature stability are two ongoing hurdles for their utilization at high temperature.[35] Alternatively, perovskite oxide nanoparticles might be good candidates for replacing noble metals; recently we discovered that the surface decoration of perovskite nanoparticles could enhance the CO sensing performance of Ga_2O_3-nanorod-array-based conductometric gas sensors at 500 °C.[36] Perovskite oxides have been known as an important class of functional materials exhibiting a number of

remarkable physical and chemical properties as in high temperature superconductors,[37-39] colossal magneto-resistant manganites, and high/medium-temperature solid oxide fuel cells.[40, 41]

Recently, β-Ga_2O_3, a wide band gap (~4.9 eV) metal oxide semiconductor, has been tapped as a promising ultra-high temperature gas sensing material due to its high thermal and chemical stabilities that can allow a stable sensor operation at temperatures up to 1000 °C.[42-44] However, for the detection of nitrous oxides, there have been few reports that tested β-Ga_2O_3 at temperatures above 500 °C. In terms of gas sensor performance, sensitivity is one of the most important figures of merit beside selectivity and stability of sensors. The sensitivity of a conductometric-type metal oxide semiconductor sensor is determined by measuring the change of resistance (conversely conductance) or current when target gas molecules interact with the sensor surface.[45] However, this type of gas sensors generally show lower sensitivity at high temperature due to usually unfavorable surface chemistries at high temperature.[46] Therefore, rational selections of sensor material and architecture design are critical for achieving highly sensitive and selective sensors at high temperature.

In this work, we have successfully developed a sensitive, robust, and low-cost nanorod-based gas sensor designed for monitoring hazardous NO_2 at high temperature, by utilizing the perovskite oxide nanoparticle surface decoration, which resulted in a drastic sensor performance enhancement. Specifically, a comparative study is conducted on the sensing properties of pristine β-Ga_2O_3 nanorod arrays and $La_{0.8}Sr_{0.2}CoO_3$-nanoparticle-decorated β-Ga_2O_3 nanorod arrays, and we find that the perovskite nanoparticle decoration enhances the NO_2 sensitivity by an order of magnitude at 800 °C

while also enabling a remarkable NO_2 selectivity over O_2 through distinctively differentiated required for the synthesis of β-Ga_2O_3-based nanorod arrays applied for high temperature NO_2 gas sensors were list in this section.

5.2.1: Precursor, Substrate and Sputtering Target Chemicals

(I) Gallium(III) nitrate hydrate ($Ga(NO_3)_3 \cdot 9H_2O$, 99.9998%): the gallium salt of nitric acid was purchased from Acros Organics. It's a white, slightly hygroscopic and crystal powder with good solubility in water. It's used as the precursor of hydrothermal synthesis in this work.

(II) Tin dioxide (SnO_2, >99.9%): the inorganic compound target with diameter 2" and 0.25" in thickness was purchased from Stanford Advanced Materials. The white circular target was used as the seed layer for further hydrothermal synthesis.

(III) Silicon (Si, (100)): substrates (boron doped, p-type, 1~10 ohm-cm, 100 mm in diameters, 500 μm in thickness, single flat, single side polish) topped with 1μm silicon dioxide (SiO_2) were purchased from University Wafer.

(IV) Lanthanum strontium cobalt oxide ($La_{0.8}Sr_{0.2}CoO_3$, 99.99%): This perovskite material was used as the target of radio-frequency magnetron sputtering to decorate the surface of β-Ga_2O_3 nanorods and purchased from Kurt J. Lesker Co..

5.2.2: Preparation of $La_{0.8}Sr_{0.2}CoO_3$ / Ga_2O_3 Nanorod Arrays

Si wafers with (100) orientation and 1 μm SiO_2 insulator layer on top are chosen as substrates. Prior to the synthesis of Ga_2O_3 nanorods, the substrate was immersed in acetone solution and sonicated for 5 minutes, followed by sonication in deionized (DI)

water for 5 minutes, repeated twice to remove the surface grease and organic deposits. To purge and remove the residual water on the surface of Si wafers, high purity nitrogen (N_2) was used for blow-drying and followed by putting on the hot plates at 80 °C for complete dry. In order to grow aligned nanorod arrays by hydrothermal synthesis, 50 nm thick SnO_2 was used as a seed layer by radio frequency (R.F.) magnetron sputtering, followed by post annealing at 900 °C for 2 hours in ambient atmosphere to help crystalline. In the hydrothermal synthesis, 0.6 g of $Ga(NO_3)_3 \cdot 9H_2O$ was used as the precursor and dissolved in 40 ml deionized (DI) water, stirring for 10 minutes to fully dissolved. The prepared solution was pour into the Teflon bottle with SnO_2-coated substrates, sealed in the autoclave and keep the reaction temperature at 150 °C for 12 hours to grow vertically aligned GaOOH nanorod arrays. After hydrothermal growth, the samples were washed and rinsed by DI water and dried in air on hot plates at 80 °C overnight. After annealing at 1000 °C for 4 hours, the as-grown GaOOH nanorods were finally converted into pure β-Ga_2O_3 nanorods.

Nanoparticles of La-based perovskite oxide $LaSrCoO_3$ were decorated on β-Ga_2O_3 nanorod arrays by R.F. magnetron sputtering method with controlled nominal thickness of 3 or 8 nm as monitored by a quartz microbalance. Followed by the R.F. magnetron sputtering, the samples were annealed at 850 °C for 2 hours to crystallize perovskite nanoparticles of the surface decoration.

5.2.3: Gas Sensing Test Setup and Installation of the Device

The resistor-type β-Ga_2O_3 nanorod array device was fabricated and tested in a high temperature tube furnace using a flow-through configuration, shown in **Figure 4-2** in

Chapter 4. An alumina ceramic tube containing two through holes was used to hold and fix two Ni/Cr wires. As for the gas sensor device, the β-Ga_2O_3 –based gas sensor was fixed on the alumina holder with two 10 mm thick platinum (Pt) wires, which were used as the electrodes of the gas sensor device, shown in **Figure 4-1** in Chapter 4. The Pt wires were connected the nanorod array gas sensor device with Ni/Cr wires, which were connected to a CHI 601C electrochemical workstation for recording the signal outputs continuously. The sensor circuit was subjected to a fixed 1volt direct current (DC) bias. The device was heated from room temperature to 800 °C in air with a ramp rate of 20 °C/min. The sensor device was placed and tested at the furnace center. Gas sensing tests were performed under the exposure of nitrogen dioxide (NO_2) of varying concentration (100 parts per million (ppm), 200 ppm, and 300 ppm (with a balance of N_2)) at 1 atmosphere total pressure and 800 °C. The responses of the sensor to NO_2 were evaluated by measuring the current change upon exposure to NO_2 in a dynamic gas flow system under a gas flow rate of 1.5 L/min, which was regulated by a computer-controlled gas mixing system (S-4000, Environics Inc., USA) and high purity nitrogen was used as carrier gas. In the gas-sensing test, the device was first exposed to NO_2/ N_2 mixture for 3 minutes, followed by high purity N_2 for 24 minutes, and then the cycles was repeated. The sensitivity is defined by (R_{NO2}/R_0), where R_{NO2} is the measured resistance of Ga_2O_3 nanorod device under NO_2/N_2 mixture, and R_0 is the resistance under high-purity N_2. All experiments were carried out at 800 °C.

5.3: Results and Discussion

In order to fabricate Ga_2O_3-based gas sensor, the combination of hydrothermal synthesis process and post-annealing treatment is required. Therefore, GaOOH nanorod arrays should be fabricated on the stiff Si substrates in the first place. X-ray Diffraction (XRD) patterns confirm that the initial hydrothermal growth yielded orthorhombic GaOOH (**Figure 5-1(a)**, top), and the following post annealing at 1000 °C finally converted GaOOH to monoclininc β-Ga_2O_3 (**Figure 5-1(a)**, bottom). The synthesized GaOOH nanorod array has a preferred growth direction perpendicular to (111), therefore, the intensity of (111) in XRD is stronger, instead of (110) which is typically observed in GaOOH powders (JCPDS #06-0180). β-Ga_2O_3 nanorods meanwhile have preferential growth orientation perpendicular to (001).

Figure 5-1(b) is a typical energy dispersive x-ray spectroscopy (EDXS) spectrum of GaOOH nanorods with clearly revealed peaks of Ga and O from the nanorods and Si from the Si substrate. **Figure 5-1(c)** shows a typical cross-sectional SEM image of as-synthesized GaOOH nanorods grown perpendicular to the substrate with a length of ~1.8 μm. The top-view SEM images of the tips of GaOOH and Ga_2O_3 nanorods clearly display a uniform diamond shape with an average diagonal length of ~200 nm, as illustrated in **Figure 5-1(d)** and **(e)**.

Figure 5-1(f) shows a low-magnification TEM image of as-synthesized GaOOH with ~100 nm effective diameter. The corresponding selected area electron diffraction (SAED) pattern in the inset features a set of discrete diffraction spots, confirming the nanorod's single-crystalline nature with an orthorhombic structure (a = 4.58 Å, b = 9.8 Å, c = 2.97 Å). The GaOOH nanorod grows perpendicular to the (111) plane. **Figure 5-1(g)** depicts

an individual β-Ga_2O_3 nanorod (diagonal width ~200 nm), revealing its mesoporous structure with a pore size of ~20 nm. The corresponding SAED pattern of the β-Ga_2O_3 nanorod confirms the monoclinic structure of β-Ga_2O_3 nanorod and its growth orientation perpendicular to (001).

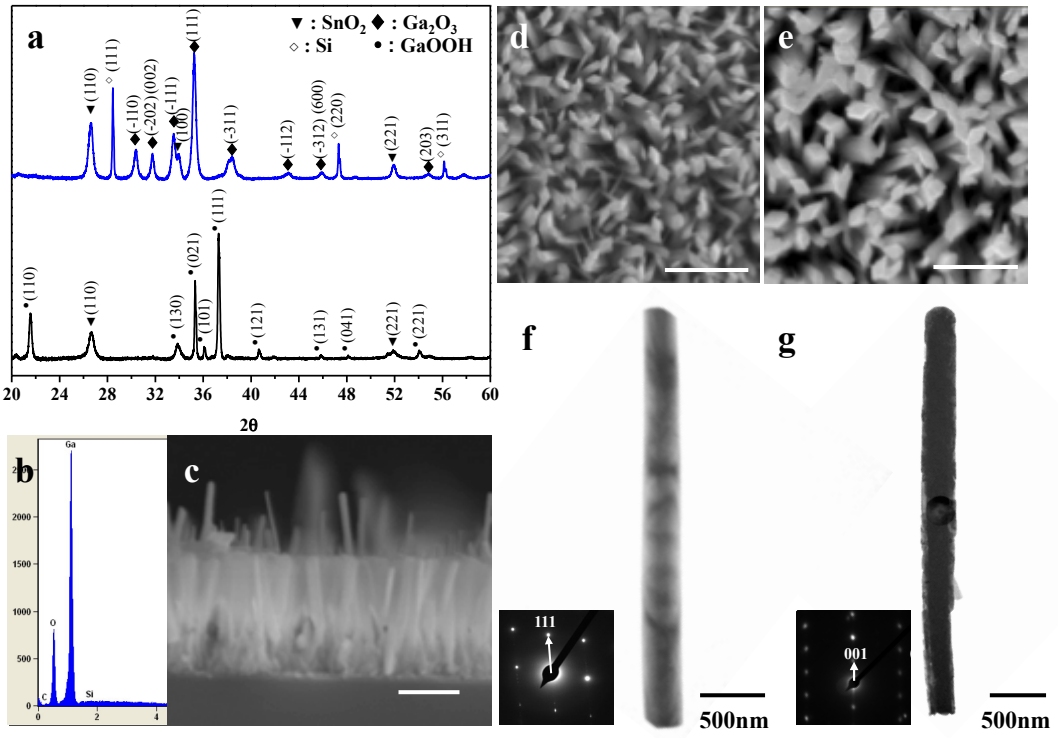

Figure 5-1: XRD patterns of (a) GaOOH nanorod arrays (top), β-Ga_2O_3nanorod arrays (bottom). (b) GaOOH energy dispersive X-ray (EDX) spectrum and (c) the corresponding cross-sectional view of GaOOH nanorod array. Top view SEM images of (d) GaOOH and (e) Ga_2O_3 nanorods. TEM images and the respective electron diffraction patterns of (f) a GaOOH nanorod grown at 150 °C, and (g) a Ga_2O_3 nanorod. Scale bar in (c), (d) and (e): 1 μm.

The XRD patterns of β-Ga_2O_3nanorod arrays decorated with two different nominal deposition thicknesses (3 nm vs. 8 nm) of LSCO nanoparticles are shown in **Figure 5-2(a)**, where most of the peaks match the monoclinic β-Ga_2O_3 and the SnO_2 seed layer.

Meanwhile, the two strongest peaks from LSCO are too close to the peaks from SnO_2 to be differentiated from them. The corresponding top-view SEM images of LSCO-nanoparticle-decorated β-Ga_2O_3 nanorods reveal negligible difference compared with pure β-Ga_2O_3 nanorods with no nanoparticle decoration (**Figure 5-2(b)** and **(c)**), indicating very small LSCO nanoparticle sizes. EDXS shown in **Figure 5-2(d)** indeed shows the presence of La, Sr, Co, O originating from the LSCO nanoparticle decoration, along with Ga and O from the nanorod cores.

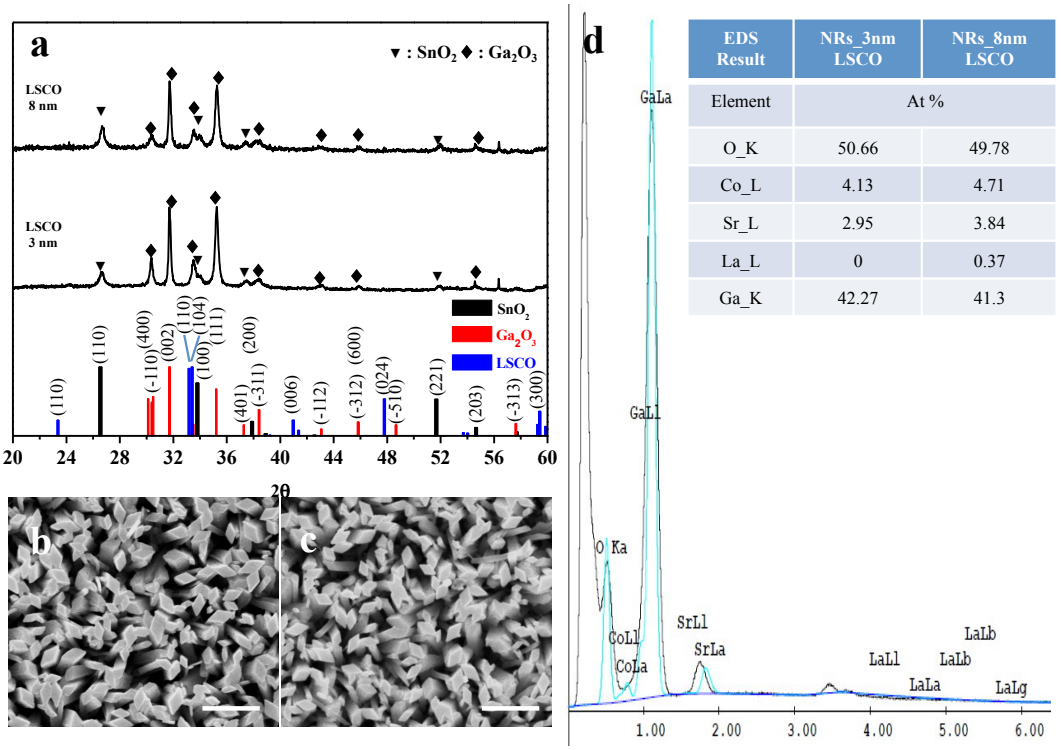

EDS Result	NRs_3nm LSCO	NRs_8nm LSCO
Element	At %	
O_K	50.66	49.78
Co_L	4.13	4.71
Sr_L	2.95	3.84
La_L	0	0.37
Ga_K	42.27	41.3

Figure 5-2: X-ray diffraction (XRD) patterns from (a) β-Ga_2O_3 nanorod arrays with 3 nm (middle) and 8 nm thick (top) LSCO nanoparticle deposition. A top-view SEM image of β-Ga_2O_3 nanorod arrays with (b) 3nm, and (c) 8 nm LSCO nanoparticle decoration. (d) EDX spectrum of β-Ga_2O_3 nanorod arrays with 3 nm LSCO decoration, and the inset table is the composition analysis of β-Ga_2O_3 nanorod arrays with LSCO decorations.

A low-magnification bright-field TEM image of a LSCO-decorated β-Ga_2O_3 nanorod clearly confirms the rough surface of nanorod decorated with LSCO nanoparticles (**Figure 5-3(a)**). The insets show the high-resolution lattice images of the LSCO decorated nanorod. LSCO nanoparticle with (110) plane is found at the nanorod surface layer, and β-Ga_2O_3 nanorod core is exposed with (002) and (-401) planes. In **Figure 5-3(b)-(f)**, the STEM elemental mapping display strong uniform intensities of Ga and O signals through the whole nanorod, while those of La, Sr, and Co are weakly scattered over the nanorod surface. The EDXS spectrum in **Figure 5-3(g)** confirms the presence of Ga and O from the nanorod, and La, Sr, and Co from the nanoparticle surface decoration.

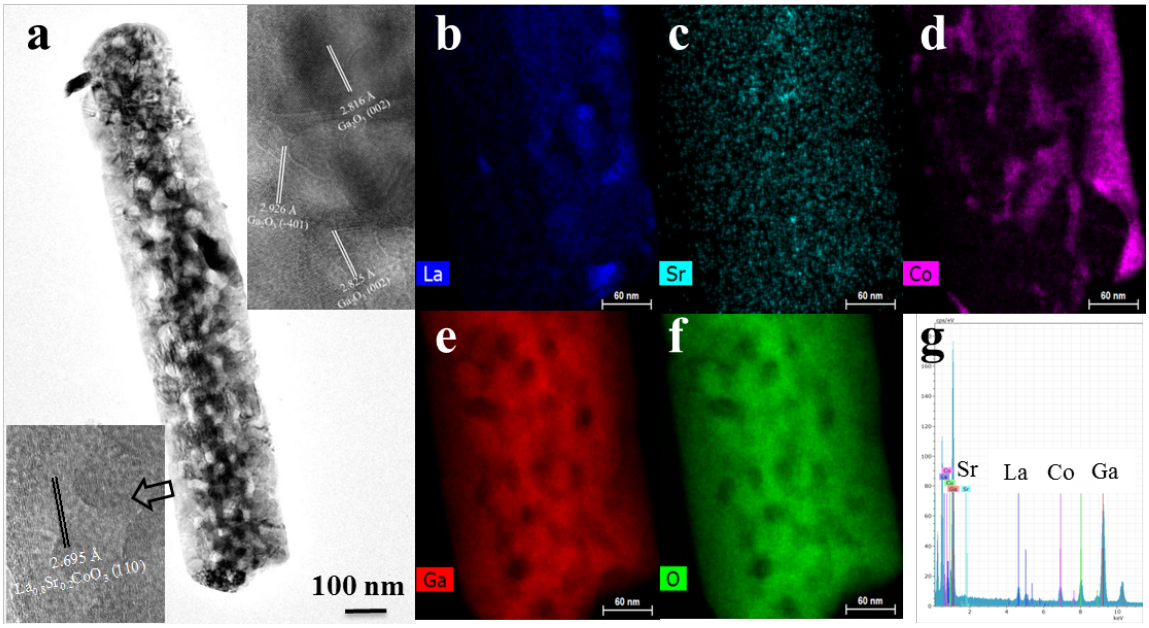

Figure 5-3: (a) TEM image of a post annealing β-Ga_2O_3 nanorod coated with 8 nm LSCO decoration. The insets are the high resolution images of coated LSCO nanoparticles on the surface (lower left corner) and β-Ga_2O_3 (upper right corner). (b)-(f) show the element mapping of 8 nm LSCO-coated β-Ga_2O_3 nanorod, presenting the element distribution of La, Sr, Co, Ga, O respectively. (g) The corresponding LSCO-coated β-Ga_2O_3 nanorod energy dispersive X-ray spectrum.

We then employed the prepared β-Ga_2O_3 nanorod arrays for *in situ* NO_2 detection at 800°C, exploiting the high temperature stability of β-Ga_2O_3. **Figure 5-4(a)** represents typical electrical responses of the β-Ga_2O_3 nanorod array as a function of time upon periodic exposures to NO_2 (with concentration of 100, 200, and 300 ppm, balanced in high purity N_2). 100 % high purity N_2 was also used to drive the recovery of the sensor. Upon exposure to NO_2, the pure β-Ga_2O_3 nanorod array shows a fast, reproducible, and concentration-dependent increase in resistance (from ~4× to ~8×), confirming the functionality of β-Ga_2O_3 nanorod array for sensing NO_2 at high temperature.

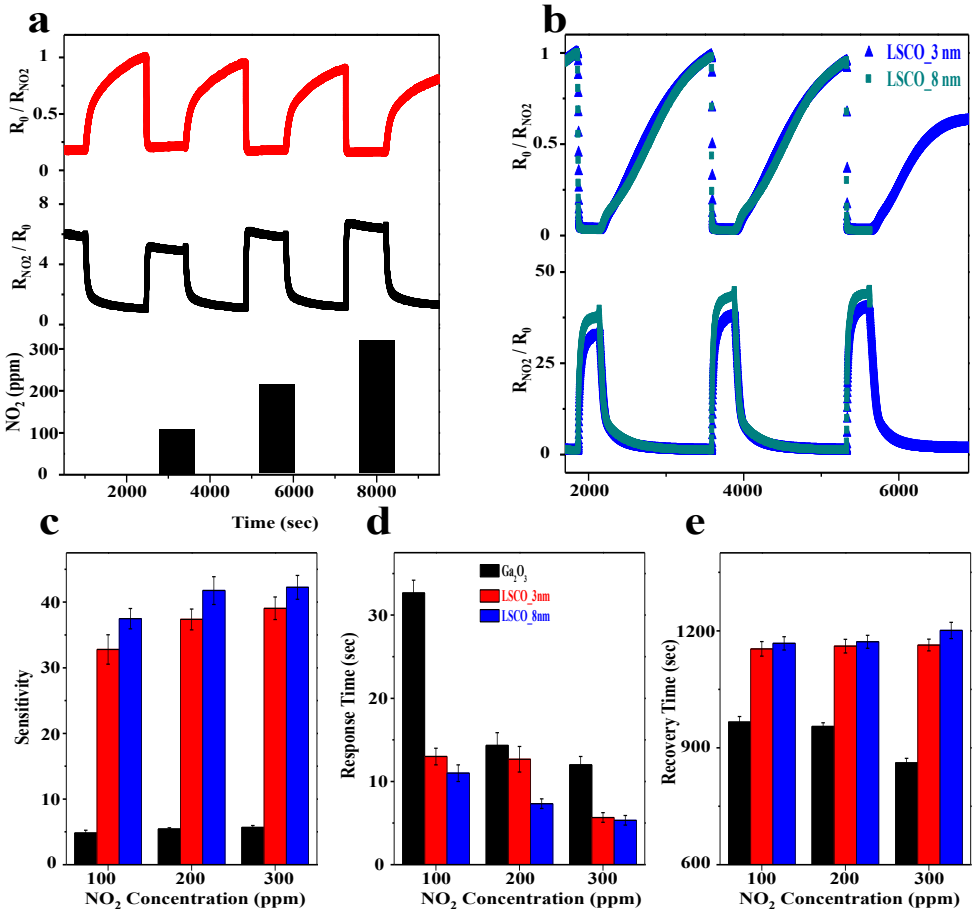

Figure 5-4: NO_2 gas sensing test results: (a) Normalized sensitivity-time characteristics of pure β-Ga_2O_3 nanorod array tested at 800 °C with N_2 as background atmosphere and its corresponding NO_2 concentration; (b) Normalized sensitivity-time characteristics of β-Ga_2O_3/LSCO nanorod arrays tested at 800 °C; (c) Sensitivity, (d) Response time and (e) Recovery time versus NO_2 concentrations characteristics of β-Ga_2O_3 and β-Ga_2O_3/LSCO nanorod arrays tested at 800 °C.

Compared with resistive-type, Ga_2O_3-based NO_2 gas sensors, Jin *et al.* demonstrated multiple networked β-Ga_2O_3-based NO_2 gas sensor, however, the response of pristine β-Ga_2O_3 toward NO_2 at 100 and 200 ppm is about 1.47 and 1.76 (relative response is ~47 and 76%) at 300 °C, respectively.[47] By purging with nitrogen, the resistance of β-Ga_2O_3 nanorod arrays could be fully reduced back to its base value, indicating a quick desorption of NO_2 molecules from the surface of β-Ga_2O_3 nanorod array. The observed response time (t_{90}) of the β-Ga_2O_3 nanorod, defined as the time when the normalized

current change reaches 90 % of the maximum response after NO_2 exposure, is 33 seconds towards 100 ppm NO_2, and it decreases for higher NO_2 concentrations (i.e., faster response). Overall, Ga_2O_3 nanorod sensor response is fast at high temperature while displaying a negligible drift in the baseline for repeated operations. This improved baseline drift performance might be due to the operated high temperature that enables faster analyte adsorption and desorption kinetics. In detail, the increase in resistance of β-Ga_2O_3 nanorod arrays upon exposure to oxidizing gas NO_2 is generally explained by the formation of an electron depletion layer on the surface of nanorods as NO_2 molecules react with conduction electrons to form surface oxide ion (O^{2-}) according to the following reaction:[22, 48]

$$NO_{2(g)} + 2e^- \rightarrow NO_{(ads)} + O^{2-}$$

The consistently observed sensor response to NO_2 via the increase in resistance thus indicates that the majority charge carriers in our β-Ga_2O_3 are electrons (thus an n-type semiconductor sensor). The predominant point defects in β-Ga_2O_3 are oxygen vacancies, and they are known to be n-type dopant, generating free electrons via following mechanism:[49]

$$Ga_2O_3 \leftrightarrow 2Ga_{Ga}^{x} + 2O_O^{x} + V_O^{*} + e^- + ½\ O_2$$

where Ga_{Ga}^{x} and O_O^{x} represent the regular lattice ions, while V_O^{*} is the charged defect with single ionized oxygen vacancy. It is worthy to note that the oxygen vacancies can also act as preferential adsorption sites for NO_2 molecules,[50, 51] facilitating the sensor response of the β-Ga_2O_3 nanorods.

We find that the decoration of catalytic LSCO nanoparticles on the pristine β-Ga_2O_3 nanorods, greatly enhances the NO_2 gas sensing performance at high temperature (800

°C). The dynamic sensing characteristics of LSCO-nanoparticle-decorated β-Ga2O_3 nanorod arrays under different NO_2 concentrations are shown in **Figure 5-4(b)**. We tested two different nominal thicknesses of LSCO nanoparticle deposition conditions (3 nm or 8 nm). Regardless of the thickness and tested NO_2 concentration, the NO_2 sensitivity of β-Ga_2O_3 nanorod arrays is enhanced over 600 % with the LSCO nanoparticle decoration. The pristine β-Ga_2O_3 nanorod arrays shows a base sensitivity ~6 at 300 ppm NO_2 exposure, while the sensitivity of 3 nm and 8 nm-LSCO-nanoparticle-decorated samples reach ~39 and 42 at the same NO_2 concentration, respectively (**Figure 5-4(c)**). Meanwhile, thicker LSCO nanoparticle decoration (8 nm) appears to modestly increase the sensitivity (by ~ 10 %) compared with 3 nm LSCO nanoparticle decoration, which is most likely resulted from an improved nanoparticle surface coverage.

Beside the significantly enhanced NO_2 sensitivity, the LSCO-nanoparticle decoration on β-Ga_2O_3 nanorod arrays also enables a faster temporal sensor response to a given NO_2 exposure compared with pristine β-Ga_2O_3 nanorod arrays. For instance, the sample with 8 nm LSCO nanoparticle decoration has a response time of ~5 seconds at the highest NO_2 concentration (300 ppm), which is about 60 % shorter than that of pristine β-Ga_2O_3nanorod arrays. The 3 nm LSCO-nanoparticle decoration also results in a similarly reduced response time (by ~67 % and ~60 % at NO_2 concentration of 100 and 300 ppm, respectively) (**Figure 5-4(d)**). Meanwhile, the recovery of β-Ga_2O_3 nanorod sensors at the absence of NO_2 becomes slower with the LSCO nanoparticle decoration by ~20 %, compared with pristine β-Ga_2O_3 nanorod array sensors (**Figure 5-4(e)**). This might be due to the different desorption kinetics of NO_2 on LSCO and Ga_2O_3 surfaces as discussed later.

For the observed enhancement in the NO_2 sensitivity by LSCO nanoparticle decoration, we find that the p-n junction is one of the likely responsible mechanisms.[52] Since the LSCO nanoparticles are p-type semiconductor, they form p-n heterojunction on the n-type β-Ga_2O_3 nanorod surface. It subsequently leads to a formation of a space charge region (i.e., depletion region) in β-Ga_2O_3 near the interface, reducing the volume of conducting channel within the individual β-Ga_2O_3 nanorods. When oxidizing NO_2 molecules come into contact with the sensor surface, the adsorption of NO_2 molecules occurs on the both surfaces of LSCO nanoparticles and uncovered β-Ga_2O_3. Especially, the unpaired electron of the NO_2 molecule reacts with the dangling bonds available on the LSCO nanoparticle surface and transforms into NO_2^-, which in turn increases the free hole concentration in the valence band of LSCO.[53] This not only renders the LSCO nanoparticles more p-type but also expands the depletion region within in the β-Ga_2O_3 in contact with LSCO, further increasing the resistance (i.e., sensor response) of Ga_2O_3. This is the extra contribution to the intrinsic resistance increase of pristine Ga_2O_3 upon the NO_2 exposure, being responsible for the overall enhanced NO_2 sensitivity by the LSCO nanoparticle decoration. By the same explanation, it is natural that the increased surface coverage of LSCO nanoparticles (i.e., larger nominal thickness of LSCO deposition condition) further improves the NO_2 sensitivity of β-Ga_2O_3 nanorod arrays as we observed.

In the meantime, we understand that the somewhat slowed senor recovery of LSCO-nanoparticle-decorated β-Ga_2O_3 nanorod arrays is most likely caused by the slower desorption kinetics of NO_2 (or NO_2^-) on the LSCO nanoparticle surface compared with those on β-Ga_2O_3—while the faster desorption of NO_2 from the β-Ga_2O_3 nanorod surface

primarily drives the decrease in resistance (i.e., sensor recovery, via reduced depletion region) during the absence of NO_2, the relatively slower NO_2 desorption from the LSCO surface results in a residual temporal resistance and consequently lagged sensor recovery as the depletion region near the LSCO nanoparticles is relieved with a slower pace.

Finally, we demonstrate a highly selective sensing of NO_2 over O_2 using the LSCO-nanoparticle-decorated β-Ga_2O_3 nanorod array sensor. In addition to the sensitivity, the selectivity is another major challenge for gas sensors used in harsh industrial environments (e.g., high temperature, high pressure, presence of contaminants, dynamic gas flow). Particularly, it becomes a key issue when there are multiple species of gas analytes with similar chemical natures. For example, O_2 is a well-known oxidizing gas that induces the increase in resistance (i.e., sensor response similar to NO_2) of n-type metal oxides upon the surface adsorption.[54, 55]

Furthermore, we find that the LSCO-nanoparticle-decorated β-Ga_2O_3 nanorod array sensor clearly differentiates NO_2 from O_2 via highly distinguishable sensitivity and response time (**Figure 5-5**). The NO_2 sensitivity of LSCO-nanoparticle-decorated (8 nm) Ga_2O_3 nanorod array sensor is ~10 times larger than that toward O_2 at the same analyte concentration (300 ppm) (**Figure 5-5(b)**). Furthermore, there is a distinct difference in response time; the sensor response time for NO_2 only is 5 seconds while it is around 400 seconds for O_2. One possible reason for this difference in response time is the difference in adsorption energies between NO_2 and O_2 on the surfaces of LSCO and Ga_2O_3. Not covered by the current the scope of study, further investigations are being planned to verify this hypothesis.

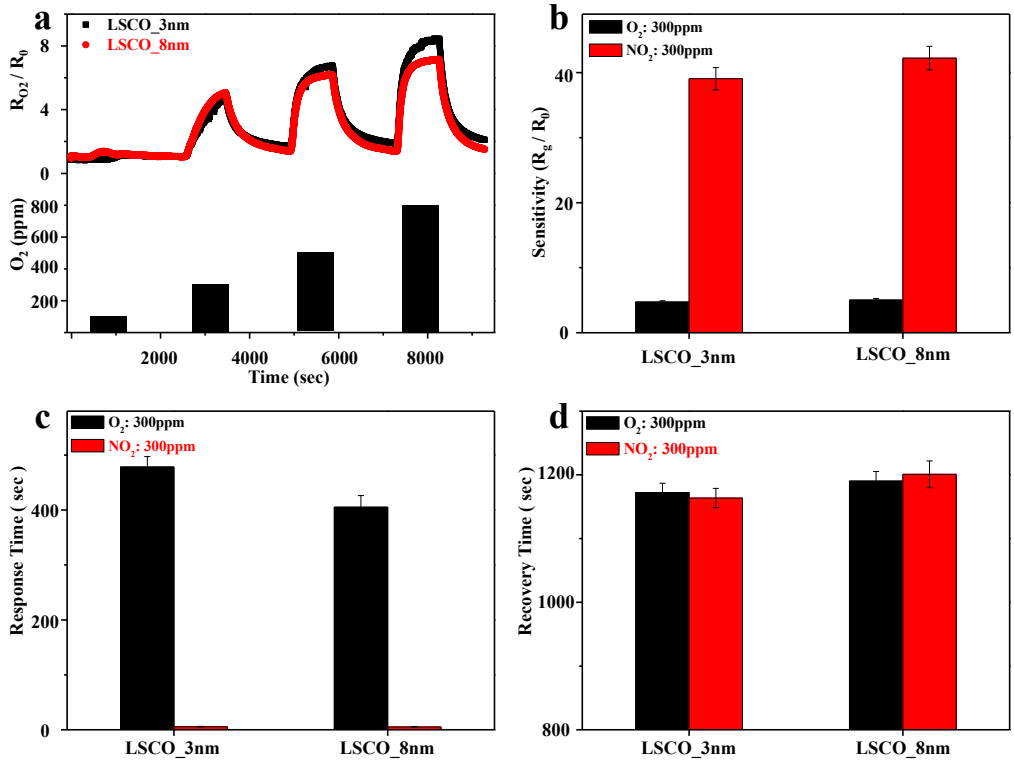

Figure 5-5: (a) Normalized sensitivity-time oxygen sensing properties of β-Ga_2O_3/LSCO nanorod arrays tested at 800 °C with N_2 as background atmosphere and its corresponding O_2 concentration. (b) Sensitivity (c) Response time and (d) Recovery time of LSCO/β-Ga_2O_3 nanorod array upon exposure to 300 ppm of NO_2 and O_2 tested at 800 °C.

5.4: Conclusion

In summary, the LSCO-nanoparticle decoration enabled a highly enhanced NO_2 sensitivity in β-Ga_2O_3 nanorod array gas sensors at high temperature with fast sensor response and high selectivity over O_2. The formation of p-n heterojunction is suggested to play major roles in the observed enhancement of sensor performances as it contributes to the modulation of depletion region with differentiated analyte desorption kinetics. These findings provide valuable information for the rational design and development of high-

performance gas sensors for oxidative gas pollutants at high temperatures.

Reference

1. Khodakarami, J.; Ghobadi, P., Urban Pollution and Solar Radiation Impacts. *Renewable Sustainable Energy Rev.* 2016, 57, 965-976.
2. Tsujita, W.; Yoshino, A.; Ishida, H.; Moriizumi, T., Gas Sensor Network for Air-Pollution Monitoring. *Sens. Actuators, B* 2005, 110, 304-311.
3. Kim, H. J.; Yoon, J. W.; Choi, K. I.; Jang, H. W.; Umar, A.; Lee, J. H., Ultraselective and Sensitive Detection of Xylene and Toluene for Monitoring Indoor Air Pollution Using Cr-Doped NiO Hierarchical Nanostructures. *Nanoscale* 2013, 5, 7066-7073.
4. Kumar, A.; Kim, H.; Hancke, G. P., Environmental Monitoring Systems : A Review. *IEEE Sens. J.* 2013, 13, 1329-1339.
5. Tuller, H. L., Materials for High Temperature Electrochemical Applications: Automotive Sensors, Catalysts and Traps. *Sens. Actuators, B* 2013, 187, 106.
6. Fergus, J. W., Solid Electrolyte Based Sensors for the Measurement of CO and Hydrocarbon Gases. *Sens. Actuators, B* 2007, 122, 683.
7. Fergus, J. W., Perovskite Oxides for Semiconductor-Based Gas Sensors. *Sens. Actuators, B* 2007, 123, 1169.
8. Fergus, J. W., Materials for High Temperature Electrochemical NO_x Gas Sensors. *Sens. Actuators, B* 2007, 121, 652.
9. Ueda, T.; Nagano, T.; Okawa, H.; Takahashi, S., Zirconia-Based Amperometric Sensor Using La–Sr-Based Perovskite-Type Oxide Sensing Electrode for Detection of NO_2. *Electrochem. Commun.* 2009, 11, 1654-1656.
10. Yang, J.-C.; Dutta, P. K., High Temperature Amperometric Total NO_x Sensors with Platinum-Loaded Zeolite Y Electrodes. *Sens. Actuators, B* 2007, 123, 929-936.
11. Mirura, N.; Lu, G.; Yamazoe, N., High-Temperature Potentiometric/Amperometric NO_x Sensors Combining Stabilized Zirconia with Mixed-Metal Oxide Electrode. *Sens. Actuators, B* 1998, 52, 169-178.
12. Zhuiykov, S.; Ono, T.; Yamazoe, N.; Mirura, N., High-Temperature NO_x Sensors Using Zirconia Solid Electrolyte and Zinc-Family Oxide Sensing Electrode. *Solid State Ionics* 2002, 152-153, 801-807.
13. Miura, N.; Koga, T.; Nakatou, M.; Elumalai, P.; Hasei, M., Electrochemical NO_x Sensors Based on Stabilized Zirconia: Comparison of Sensing Performances of Mixed-Potential-Type and Impedancemetric NO_x Sensors. *J. Electroceram.* 2006, 17, 979-986.
14. Mirura, N.; Zhuiykov, S.; Ono, T.; Hasei, M.; Yamazoe, N., Mixed Potential Type Sensor Using Stabilized Zirconia and $ZnFe_2O_4$ Sensing Electrode for Noxdetectionat High Temperature. *Sens. Actuators, B* 2002, 83, 222-229.
15. Mirura, N.; Akisada, K.; Wang, J.; Zhuiykov, S.; Ono, T., Mixed-Potential-Type NO_x Sensor Based on YSZ and Zinc Oxide Sensing Electrode. *Ionics* 2004, 10, 1-9.
16. Ferroni, M.; Guidi, V.; Martinelli, G.; Nelli, P.; Sberveglieri, G., Gas-Sensing Applications of W–Ti–O-Based Nanosized Thin Films Prepared by R.F. Reactive Sputtering. *Sens. Actuators, B* 1997, 44, 499-502.

17. Afzal, A.; Cioffi, N.; Sabbatini, L.; Torsi, L., NO_x Sensors Based on Semiconducting Metal Oxide Nanostructures: Progress and Perspectives. *Sens. Actuators, B* 2012, 171-172, 25-42.
18. Ruiz, A. M.; Sakai, G.; Cornet, A.; Shimanoe, K.; Morante, J. R.; Yamazoe, N., Cr-Doped TiO_2 Gas Sensor for Exhaust NO_2 Monitoring. *Sens. Actuators, B* 2003, 93, 509-518.
19. Lu, G.; Miura, N.; Yamazoe, N., High-Temperature Sensors for NO and NO_2 Based on Stabilized Zirconia and Spinel-Type Oxide Electrodes. *J. Mater. Chem.* 1997, 7, 1445-1449.
20. You, L.; He, X.; Wang, D.; Sun, P.; Sun, Y. F.; Liang, X. S.; Du, Y.; Lu, G. Y., Ultrasensitive and Low Operating Temperature NO_2 Gas Sensor Using Nanosheets Assembled Hierarchical WO_3 Hollow Microspheres. *Sens. Actuators, B* 2012, 173, 426-432.
21. Sharma, A.; Tomar, M.; Gupta, V., SnO_2 Thin Film Sensor with Enhanced Response for NO_2 Gas at Lower Temperatures. *Sens. Actuators, B* 2011, 156, 743-752.
22. Giang, H. T.; Duy, H. T.; Ngan, P. Q.; Thai, G. H.; Thu, D. T. A.; Thu, D. T.; Toan, N. N., High Sensitivity and Selectivity of Mixed Potential Sensor Based on Pt/YSZ/$SmFeO_3$ To NO_2 Gas. *Sens. Actuators, B* 2013, 183, 550-555.
23. Li, Y.; Wlodarski, W.; Galatsis, K.; Moslih, S. H.; Cole, J.; Russo, S.; Rockelmann, N., Gas Sensing Properties of P-Type Semiconducting Cr-Doped TiO_2 Thin Films. *Sens. Actuators, B* 2002, 83, 160-163.
24. Huang, H.; Tian, S.; Xu, J.; Xie, Z.; Zeng, D.; Chen, D.; Shen, G., Needle-Like Zn-Doped SnO_2 Nanorods with Enhanced Photocatalytic and Gas Sensing Properties. *Nanotechnology* 2012, 23, 105502.
25. Wan, Q.; Wang, T. H., Single-Crystalline Sb-Doped SnO_2 Nanowires: Synthesis and Gas Sensor Application. *Chem. Commun.* 2005, 3841-3843.
26. Rai, P.; Kim, Y.-S.; Song, H.-M.; Song, M.-K.; Yu, Y.-T., The Role of Gold Catalyst on the Sensing Behavior of ZnO Nanorods for CO and NO_2 Gases. *Sens. Actuators, B* 2012, 165, 133-142.
27. Joshi, R. K.; Hu, Q.; Alvi, F.; Joshi, N.; Kumar, A., Au Decorated Zinc Oxide Nanowires for CO Sensing. *J. Phys. Chem. C* 2009, 113, 16119-16202.
28. Kolmakov, A.; Klenov, D. O.; Lilach, Y.; Stemmer, S.; Moskovits, M., Enhanced Gas Sensing by Individual SnO_2 Nanowires and Nanobelts Functionalized with Pd Catalyst Particles. *Nano Lett.* 2005, 5, 667-673.
29. Xing, R.; Li, Q.; Xia, L.; Song, J.; Xu, L.; Zhang, J.; Xie, Y.; Song, H., Au-Modified Three-Dimensional In_2O_3 Inverse Opals: Synthesis and Improved Performance for Acetone Sensing toward Diagnosis of Diabetes. *Nanoscale* 2015, 7, 13051-13060.
30. Rai, P.; Khan, R.; Raj, S.; Majhi, S. M.; Park, K. K.; Yu, Y. T.; Lee, I. H.; Sekhar, P. K., Au@Cu_2O Core-Shell Nanoparticles as Chemiresistors for Gas Sensor Applications: Effect of Potential Barrier Modulation on the Sensing Performance. *Nanoscale* 2014, 6, 581-588.
31. Miller, D. R.; Akbar, S. A.; Morris, P. A., Nanoscale Metal Oxide-Based Heterojunctions for Gas Sensing: A Review. *Sens. Actuators, B* 2014, 204, 250-272.
32. Wang, J. X.; Sun, X. W.; Yang, Y.; Kyaw, K. K.; Huang, X. Y.; Yin, J. Z.; Wei, J.; Demir, H. V., Free-Standing ZnO-CuO Composite Nanowire Array Films and Their Gas Sensing Properties. *Nanotechnology* 2011, 22, 325704.

33. Wu, N.; Zhao, M.; Zheng, J.-G.; Jiang, C.; Myers, B.; Li, S.; Chyu, M.; Mao, S. X., Porous CuO–ZnO Nanocomposite for Sensing Electrode of High-Temperature CO Solid-State Electrochemical Sensor. *Nanotechnology* 2005, 16, 2878-2881.
34. Li, L.; Zhang, C.; Chen, W., Fabrication of SnO_2-SnO Nanocomposites with p-n Heterojunctions for the Low-Temperature Sensing of NO_2 Gas. *Nanoscale* 2015, 7, 12133-12142.
35. Wang, Z. L.; Petroski, J. M.; Green, T. C.; El-Sayed, M. A., Shape Transformation and Surface Melting of Cubic and Tetrahedral Platinum Nanocrystals. *J. Phys. Chem. B* 1998, 102, 6145-6151.
36. Lin, H.-J.; Baltrus, J. P.; Gao, H.; Ding, Y.; Nam, C.-Y.; Ohodnicki, P.; Gao, P.-X., Perovskite Nanoparticle-Sensitized Ga_2O_3 Nanorod Arrays for CO Detection at High Temperature. *ACS Appl. Mater. Interfaces* 2016, 8, 8880-8887.
37. Hancock, C. A.; Porras-Vazquez, J. M.; Keenan, P. J.; Slater, P. R., Oxyanions in Perovskites: From Superconductors to Solid Oxide Fuel Cells. *Dalton Trans.* 2015, 44, 10559-10569.
38. Rubel, M. H.; Miura, A.; Takei, T.; Kumada, N.; Mozahar Ali, M.; Nagao, M.; Watauchi, S.; Tanaka, I.; Oka, K.; Azuma, M.; Magome, E.; Moriyoshi, C.; Kuroiwa, Y.; Azharul Islam, A. K., Superconducting Double Perovskite Bismuth Oxide Prepared by A Low-Temperature Hydrothermal Reaction. *Angew. Chem.* 2014, 53, 3599-3603.
39. Yan, B.; Jansen, M.; Felser, C., A Large-Energy-Gap Oxide Topological Insulator Based on the Superconductor $BaBiO_3$. *Nat. Phys.* 2013, 9, 709-711.
40. Staruch, M.; Gao, H.; Gao, P.-X.; Jain, M., Low-Field Magnetoresistance in $La_{0.67}Sr_{0.33}MnO_3$: ZnO Composite Film. *Adv. Funct. Mater.* 2012, 22, 3591-3595.
41. Gao, H.; Staruch, M.; Jain, M.; Gao, P.-X.; Shimpi, P.; Guo, Y.; Cai, W.; Lin, H.-J., Structure and Magnetic Properties of Three-Dimensional (La,Sr)MnO_3 Nanofilms on ZnO Nanorod Arrays. *Appl. Phys. Lett.* 2011, 98, 123105.
42. Bartic, M.; Ogita, M.; Isai, M.; Baban, C.-L.; Suzuki, H., Oxygen Sensing Properties at High Temperatures of β-Ga_2O_3 Thin Films Deposited by the Chemical Solution Deposition Method. *J. Appl. Phys.* 2007, 102, 023709.
43. Hoefer, U.; Frank, J.; Fleisher, M., High Temperature Ga_2O_3-Gas Sensors and SnO_2-Gas Sensor: A Comparison. *Sens. Actuators, B* 2001, 78, 6-11.
44. Schwebel, T.; Fleischer, M.; Meixner, H.; Kohl, C.-D., CO-Sensor for Domestic Use Based on High Temperature Stable Ga_2O_3 Thin Flms. *Sens. Actuators, B* 1998, 49, 46-51.
45. Wang, C.; Yin, L.; Zhang, L.; Xiang, D.; Gao, R., Metal Oxide Gas Sensors: Sensitivity and Influencing Factors. *Sensors* 2010, 10, 2088-2106.
46. Liu, Y.; Parisi, J.; Sun, X.; Lei, Y., Solid-State Gas Sensors for High Temperature Applications – A Review. *J. Mater. Chem. A* 2014, 2, 9919-9943.
47. Jin, C.; Park, S.; Kim, H.; Lee, C., Ultrasensitive Multiple Networked Ga_2O_3-Core/ZnO-Shell Nanorod Gas Sensors. *Sens. Actuators, B* 2012, 161, 223-228.
48. Gönüllü, Y.; Haidry, A. A.; Saruhan, B., Nanotubular Cr-Doped TiO_2 for Use as High-Temperature NO_2 Gas Sensor. *Sens. Actuators, B* 2015, 217, 78-87.
49. Bartic, M.; Baban, C.-I.; Suzuki, H.; Ogita, M.; Isai, M., β-Gallium Oxide as Oxygen Gas Sensors at a High Temperature. *J. Am. Ceram. Soc.* 2007, 90, 2879-2884.

50. Maeng, S.; Kim, S. W.; Lee, D. H.; Moon, S. E.; Kim, K. C.; Maiti, A., SnO_2 Nanoslab as NO_2 Sensor: Identification of the NO_2 Sensing Mechanism on a SnO_2 Surface. *ACS Appl. Mater. Interfaces* 2014, 6, 357-363.
51. Epifani, M.; Prades, J. D.; Comini, E.; Pellicer, E.; Avella, M.; Siciliano, P.; Faglia, G.; Cirera, A.; Scotti, R.; Morazzoni, F.; Morante, J. R., The Role of Surface Oxygen Vacancies in the NO_2 Sensing Properties of SnO_2 Nanocrystals. *J. Phys. Chem. C* 2008, 112, 19540-19546.
52. Sharma, A.; Tomar, M.; Gupta, V., Enhanced Response Characteristics of SnO_2 Thin Film Based NO_2 Gas Sensor Integrated with Nanoscaled Metal Oxide Clusters. *Sens. Actuators, B* 2013, 181, 735-742.
53. Thirumalairajan, S.; Girija, K.; Mastelaro, V. R.; Ponpandian, N., Surface Morphology-Dependent Room-Temperature $LaFeO_3$ Nanostructure Thin Films as Selective NO_2 Gas Sensor Prepared by Radio Frequency Magnetron Sputtering. *ACS Appl. Mater. Interfaces* 2014, 6, 13917-13927.
54. Xu, Y.; Zhou, X.; Sorensen, O. T., Oxygen Sensors Based on Semiconducting Metal Oxides: An Overview. *Sens. Actuators, B* 2000, 65, 2-4.
55. Liu, Z.; Yamazaki, T.; Shen, Y.; Kikuta, T.; Nakatani, N.; Li, Y., O_2 and CO Sensing of Ga_2O_3 Multiple Nanowire Gas Sensors. *Sens. Actuators, B* 2008, 129, 666-670.

CHAPTER 6

UV-Enhanced CO Sensing Using Ga_2O_3-Based Nanorod Arrays at Elevated Temperature

Monitoring and control of gaseous combustion process are critically important in advanced energy generation systems such as power plants, gas turbines, and automotive engines, etc. However, very limit number of gas sensors in the market are available for such application due to the inherent high temperature of combustion gases. Therefore, there is an urgent need to develop fast, sensitive, and stable high-temperature gas sensors for various applications. In this study, we developed a new, high-performance, non-noble-metal based catalytic nanoparticle nanorod array gas sensor assisted with ultra-violet [1] illumination for high-temperature gas sensing application. A comparative sensor study was conducted between nanowire arrays of pristine β-Ga_2O_3, $La_{0,,8}Sr_{0.2}FeO_3$(LSFO)- decorated β-Ga_2O_3, and Pt-decorated β-Ga_2O_3 under UV illumination.

Without UV-illumination, it was found surface decoration of a thin layer of either LSFO or Pt nanoparticles can enhance the sensitivity to 10.15 and 10.81 times for 5 nm LSFO and 1nm Pt, respectively. The improvement of sensitivity is around an order of magnitude of CO at 500 °C.

Besides, under the illumination of UV wavelength of 254 nm, the CO gas-sensing performances of Ga_2O_3-based nanorod arrays sensors were further enhanced, such as improve the sensitivity to 125 %, reduce the response time to 69 % for LSFO-decorated

sample after turning on UV-illumination. Similar results were found for Pt-decorated sample as well.

The enhancement of sensing properties for detecting CO gas under UV light illumination at high temperature is due to the increase of photoinduced electron-hole pairs. In the condition of LSFO-decorated β-Ga_2O_3 nanorad array sensor under UV light, the enhancement is through the combination of sensitizing effect and photocurrent.

6.1: Introduction

In order to efficiently monitor and control combustion process of various feedstocks and reduce the resultant emissions at high temperature, numerous efforts have been made to develop high temperature gas sensors and deal with increasingly stringent air pollutions.[2, 3] For automotive and power industries, incomplete combustion of energy source, i.e. fossil fuel, leads to the emission of carbon monoxide (CO) and hydrocarbons(HCs).[4] Combustion efficiency or reduction of the pollutant emission can be improved by high temperature gas sensor providing real-time feedback to combustion process and monitor emissions.[2, 3] These gas sensors are required to be operated in harsh environment at above 500 °C and in particularly the exhaust gases out of engines can reach temperature close to 1000 °C.[5-7] Therefore, gas sensors possessing extremely good thermal stability as well as high sensitivity and selectivity for *in-situ* application were required. In order to meet the requirement of *in-situ* gas sensing detection at high temperature, metal oxide-based electrochemical sensors have been seen as potential high temperature gas sensing candidates for past few decades due to its viable and robust technology.[2-9]

Moreover, the optical gas sensor is another powerful and promising methodology to monitor the presence of gas species and concentrations in the market. Typically, optical sensors are based on measurement of optical absorption at specific wavelengths. In contrast, optical gas sensors provide fast response and high gas specificity, i.e., great selectivity, with non-cross-response to other gases which are not the target and present an interesting and potentially viable solution to avoid the challenge of making reliable electrical contacts on sensing elements such as nanomaterials in order to fabricate electrical or electrochemical sensors.[10] Lately, the development of optical sensors directly uses photon-matter interactions such as luminescence, optical spectrum or electro-activated mechanical sensors (e.g., surface acoustic wave), which can monitor and detect gas species in various advanced power systems wirelessly.[11]

Although optical fiber or SAW sensors have been successfully applied individually in harsh environments for remote and wireless sensing, there're several other significantly optical methods such as photocurrent or photoluminescence been neglected for real time gas detection. With the cooperation of these optical sensing modes, there're some improvements and merits which can easily prevail over other methods. For example, in the case of photocurrent, the sensing response time could be shorten in the range of a fraction of second.[12] An integrated auto-combustion exhaust gas sensor including a photodector based on gallium nitride (GaN) and an UV arc discharge lamp was also demonstrated.[13] The arc discharge lamp induces electronic transitions in the gas molecules flowing between the light source and the GaN photodetector. The modifying fraction of light in the UV spectral region detected by the GaN photodetector can be determined the exhaust gas concentration. In addition, recent works by Faglia et al.,[14, 15]

revealed that by employing the luminescence, SnO_2 nanowires' visible emission could be quenched upon exposure to very low concentrations of NO_2 on the range of a few ppm, so was found the similar result of porous silica shells of diatoms.[16] Therefore, a portable sensor using a luminescence detector and photoexcitation source (e.g., UV souce) has been realized at room temperature.

To the best of my knowledge, most of the gas sensors equipped with photoexcitation sources have been done at low temperature. In this report, we tried to incorporate photoexcitation source into the nanorod-based gas sensor arrays and successfully demonstrated a UV photo-assisted Ga_2O_3-based nanowire gas sensors that could effectively work at high temperature. The Ga_2O_3-based nanorod arrays were successfully prepared by post thermal annealing following a hydrothermal deposition method. Our prior work indicated that Ga_2O_3-based resistor-type gas sensor shows great sensitivity to reducing gas, i.e. CO, at 500°C and thus would be one of the most promising materials for high temperature gas sensor application. However, both response and recovery time should be considered in the gas sensor as well. In the present work, we conduct a comparative study on the sensing properties of pristine, Pt-nanoparticle-, and $La_{0.8}Sr_{0.2}FeO_3$ (LSFO)-nanoparticle-sensitized β-Ga_2O_3 nanorod arrays with UV light illumination and clearly show that the perovskite-nanoparticle decoration can enhance the gas sensitivity by an order of magnitude at 500°C with excellent dynamic gas sensing response characteristics, which rival the performance of Pt-decorated sensors. The UV light illumination is found to improve the sensitivity, response and recovery performances of these sensors.

6.2: Experimental

In this section, the chemicals or substrates needed for the hydrothermal synthesis of β-Ga_2O_3-based nanorod arrays and the ultra-violet light source conducted for high temperature CO gas sensing test were list in this section. Also, all the steps for the hydrothermal synthesis method were described here.

6.2.1: Precursor, Substrate and Sputtering Target Chemicals

(I) Gallium (III) nitrate hydrate ($Ga(NO_3)_3 \cdot 9H_2O$, 99.9998%): the white-colored gallium salt of nitric acid with good solubility in water was purchased from Acros Organics and it's the precursor of the Ga_2O_3 nanorod.

(II) Tin dioxide (SnO_2, >99.9%): the white circular, inorganic compound target was used for R.F. magnetron sputtering to fabricate the seed layer for further hydrothermal synthesis. It's purchased from Stanford Advanced Materials.

(III) Silicon (Si, (100)): substrates (boron doped, p-type, 1~10 ohm-cm, 100 mm in diameters, 500 μm in thickness, single flat, single side polish) topped with 1μm silicon dioxide (SiO_2) as the insulation layer were purchased from University Wafer.

(IV) Lanthanum strontium iron oxide ($La_{0.8}Sr_{0.2}FeO_3$, 99.99%): this perovskite material was used as the target of radio-frequency magnetron sputtering to decorate the surface of β-Ga_2O_3 nanorods and purchased from Kurt J. Lesker Co.

(V) Platinum (Pt, 99.999%): the noble metal target was used as the target for direct current (D.C.) sputtering to modify the surface of β-Ga_2O_3 nanorods and purchased from Kurt J. Lesker Co.

6.2.2: Preparation of $La_{0.8}Sr_{0.2}FeO_3$ / Ga_2O_3 Nanorod Arrays

Si (100) wafers with 1 μm SiO_2 insulator layer are used as substrates in this experiment. For the purpose of removing surface grease and organic deposits, substrates were immersed in acetone solution and sonicated for 5 minutes and rinsed for another 5 minutes by deionized (DI) water. In order to remove the residual water on the surface of Si substrate, Si substrates were hold tilt and high purity nitrogen gas (N_2) was used to purge the surface in one direction towards the low side. A seed layer, 50 nm tin dioxide (SnO_2), was sputtered on Si substrates by radio frequency (RF) magnetron sputtering system and followed by ambient post-annealing at 900 °C for 2 hours in order to make it crystalline. Gallium hydroxide (GaOOH) nanoroad arrays were fabricated on Si/SiO_2 substrates through hydrothermal method. First, a $Ga(NO_3)_3$ solution with the pH value controlled at around 2 was prepared by dissolving 0.6g $Ga(NO_3)_3 \cdot 9H_2O$ in 40 ml deionized (DI) water and stirred for 10 minutes. Vertical GaOOH nanorod arrays were then fabricated on SnO_2 seed layer of the Si substrates incubated in the precursor solution at 150 °C for 12 hours for the hydrothermal growth. The fabricated GaOOH nanorod arrays samples were washed by DI water after the growth, dried at 80 °C and then annealed at 1000 °C for 4 hours to convert into pure β-Ga_2O_3 nanorod arrays completely. The surface decoration of nanoparticles, either Pt or La-based perovskite oxide LSFO, on β-Ga_2O_3 nanorod arrays was achieved by RF magnetron sputtering and the nominal thickness was monitored by a quartz microbalance installed in the chamber.

6.2.3: Gas Sensing Test Setup and Installation of the Device

The resistor-type β-Ga_2O_3-based nanorod arrays were installed on an Al_2O_3 ceramic holder, as illustrated in **Figure 4-1**. Two Pt wires with the thickness of 10 μm, serving as two electrodes, were tightly tied into the two close ceramic bulks acting as the substrate holder. The β-Ga_2O_3-based nanorod arrays were kept in the center of the ceramic holder and exposure area with size dimensions of 1 centimeter x 0.5 centimeter is acted as sensing area. The sensor device placed in the center of a tube furnace equipped with a temperature controller was connected to a CHI 660D electrochemical analyzer (CH Instruments Inc., USA) through two long Ni-Cr alloy wires which acts and electrodes and were embedded into a alumina tube to conduct *in-situ* temperature gas sensing tests.

After the installation, the temperature of the tube furnace was then heated from room temperature to 500 °C in air with a ramping rate of 20 °C/min. The gas sensing performance of the β-Ga_2O_3-based nanorod arrays at 500 °C was evaluated by measuring the resistivity change which the applied voltage was kept at 1 volt upon exposure to fixed concentration of carbon monoxide at 100 parts-per-million (ppm) in a gas flow system with a constant flow rate of 1.5 L/min. In order to prevent the oxidation of carbon monoxide- a strong reducing gas- react with O_2, high purity nitrogen was used as the carrying gas instead of air to avoid a strong reducing gas, i.e. CO, to react with oxygen at 500 °C. During CO sensing experiment, the sensor placed in a furnace at 500 °C was first exposed to CO/N_2 mixture for 16 minutes, followed by high purity N_2 for 24 minutes to recover the gas sensor, and then the cycle of exposure and recovery was repeated.

The sensitivity of the devices defined here is: I_{CO} / I_0, where I_{CO} is the current under CO/N_2 mixture and I_0 is the current under high purity N_2. The response time is defined as 'the time duration required for gas sensitivity to reach 90 % upon exposure of a sensor to CO', and recovery is defined as 'the time duration required for the gas sensitivity to decrease to 10 % of the sensitivity upon the termination of CO injection.

6.3: Results and Discussion

The crystal phases of as-synthesized GaOOH**,** β-Ga_2O_3 nanorods before and after surface decoration of Pt or $La_{0.8}Sr_{0.2}FeO_3$ were characterized by XRD shown in **Figure 6-1**. As shown in **Figure 6-1(a)**, the XRD spectrum of internediate GaOOH nanorods matchs the combination of orthorhombic GaOOH phase (JCPDS # 06-0180) and the underlayer SnO_2 phase. In typical GaOOH powder, (110) plane shows the strongest intensity, however, GaOOH nanorods show the preferred growth orientation perpendicular to (111) plane in this study. Other minor peaks in the spectrum are from the underlying tetragonal SnO_2 seed layer. The GaOOH phase is completed converted to monoclinic β-Ga_2O_3 (JCPDS # 41-1103) phase, shown in **Figure 6-1(b),** after post annealing at 1000 °C for 4 hours. However, due to the small volume of surface decoration, the XRD spectrum of either Pt **(Figure 6-1(c))** or LSFO (**Figure 6-1(d)**)-coated β-Ga_2O_3 nanorods didn't show clear peaks corresponding to Pt or LSFO phase.

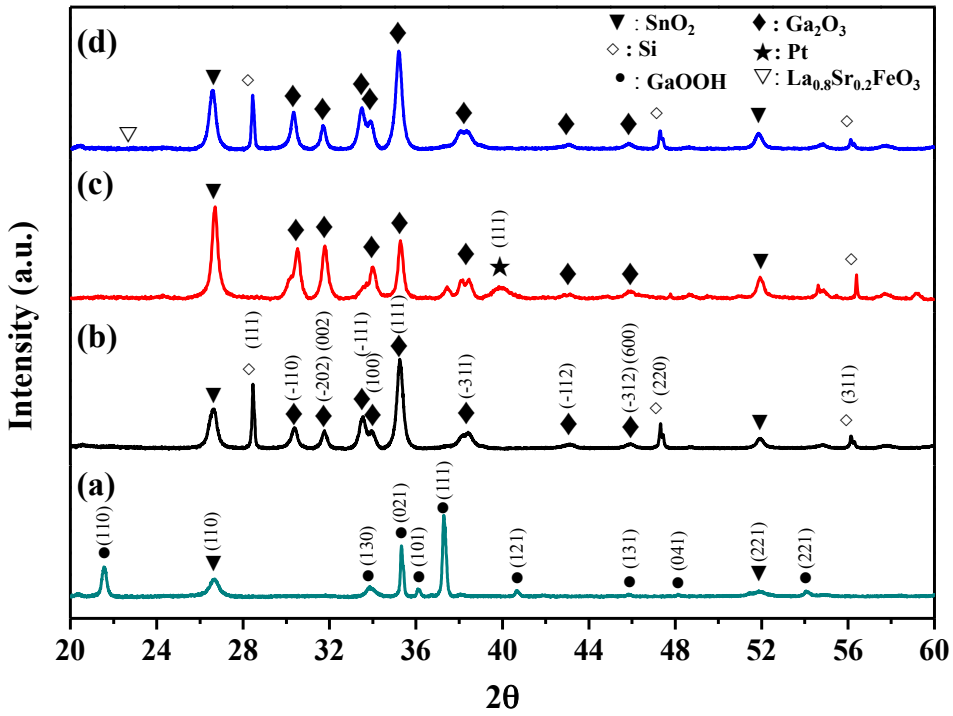

Figure 6-1: X-ray diffraction (XRD) patterns of (a) GaOOH nanorod arrays, (b) β-Ga_2O_3 nanorod arrays, (c) β-Ga_2O_3 / Pt particles nanorod arrays, (d) β-Ga_2O_3 /LSFO nanorod arrays.

The morphology of the grown vertically nanorod arrays was characterized by SEM, as shown in **Figure 6-2**. The as-synthesized GaOOH nanorod arrays were uniform in shape with diamond-shaped cross-section diagonal length of 100 - 300 nm and length close to 2 μm, which were shown in **Figure 6-2(a)** and **(b)**, respectively. **Figure 6-2(c)** presents the X-ray energy dispersive spectroscopy (EDX) point analysis was employed to investigate the compositions of the GaOOH nanorod, indicating the presence of Ga and O exists on the nanorod and Si signal from the supported Si substrate.

After the post heat treatment at 1000 °C for 4 hours, the converted pure β-Ga_2O_3 phase retained the diamond-shaped tips, which were not affected by following Pt or LSFO nanoparticle decoration and were shown in **Figure 6-2(d)**, **(e)** and **(f)**.

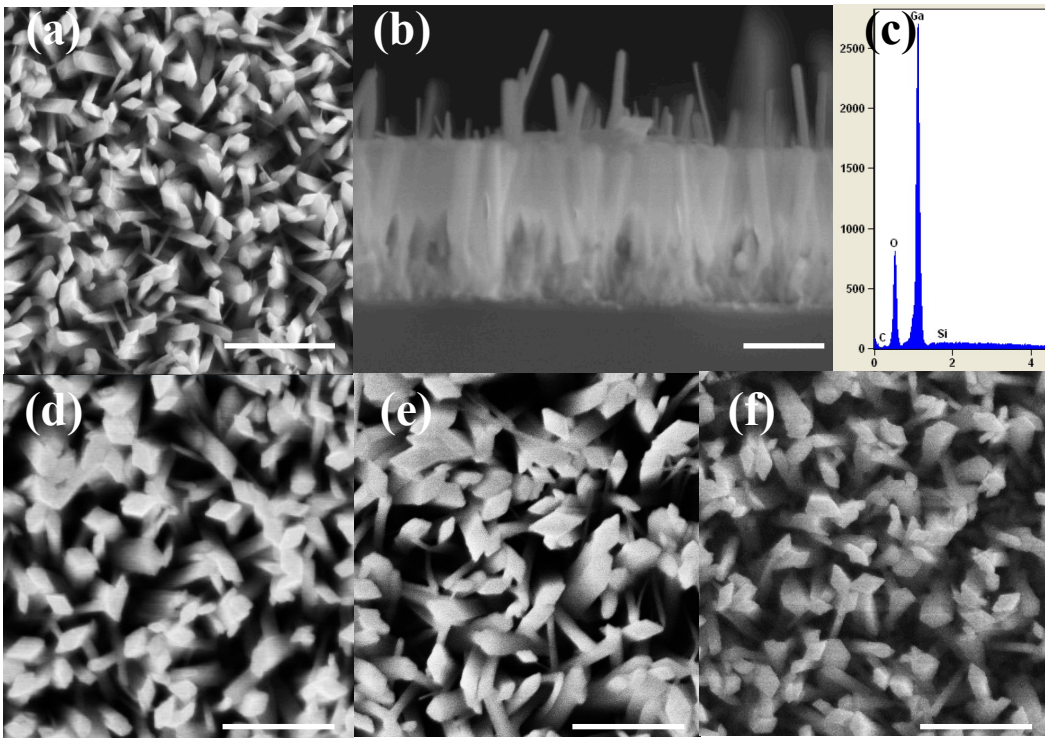

Figure 6-2: (a) top and (b) cross-sectional view SEM image, (c) EDX spectrum of GaOOH nanorod arrays,(d) a top view of Ga_2O_3, (e) 5 nm LSFO surface decoration of Ga_2O_3, (f) Sputtered Pt surface decoration of Ga_2O_3. Scale bar is 1μm.

In order to investigate the distribution of Pt nanoparticles over β-Ga_2O_3 nanorod, the low-magnification and high resolution of bright-field TEM images were took and shown in **Figure 6-3(a)**. The diameter of the nanorod is around 200 nm and the length is around 1 μm. High-resolution image shows the surface of the β-Ga_2O_3 nanorod is covered with bumping Pt nanoparticles which the diameter of each nanoparticle on the edge of β-Ga_2O_3 nanorod is around 2 nm. The corresponding Energy-Disperse X-ray spectrum and

composition analysis are also shown on the up-right side, the signals of Ga, o and Pt were clearly observed. **Figure 6-3(b) ~ (d)** show the element mapping and the intensities of Ga and O are strong through the whole nanorod and the signal of Pt is well-distributed over the whole nanorod.

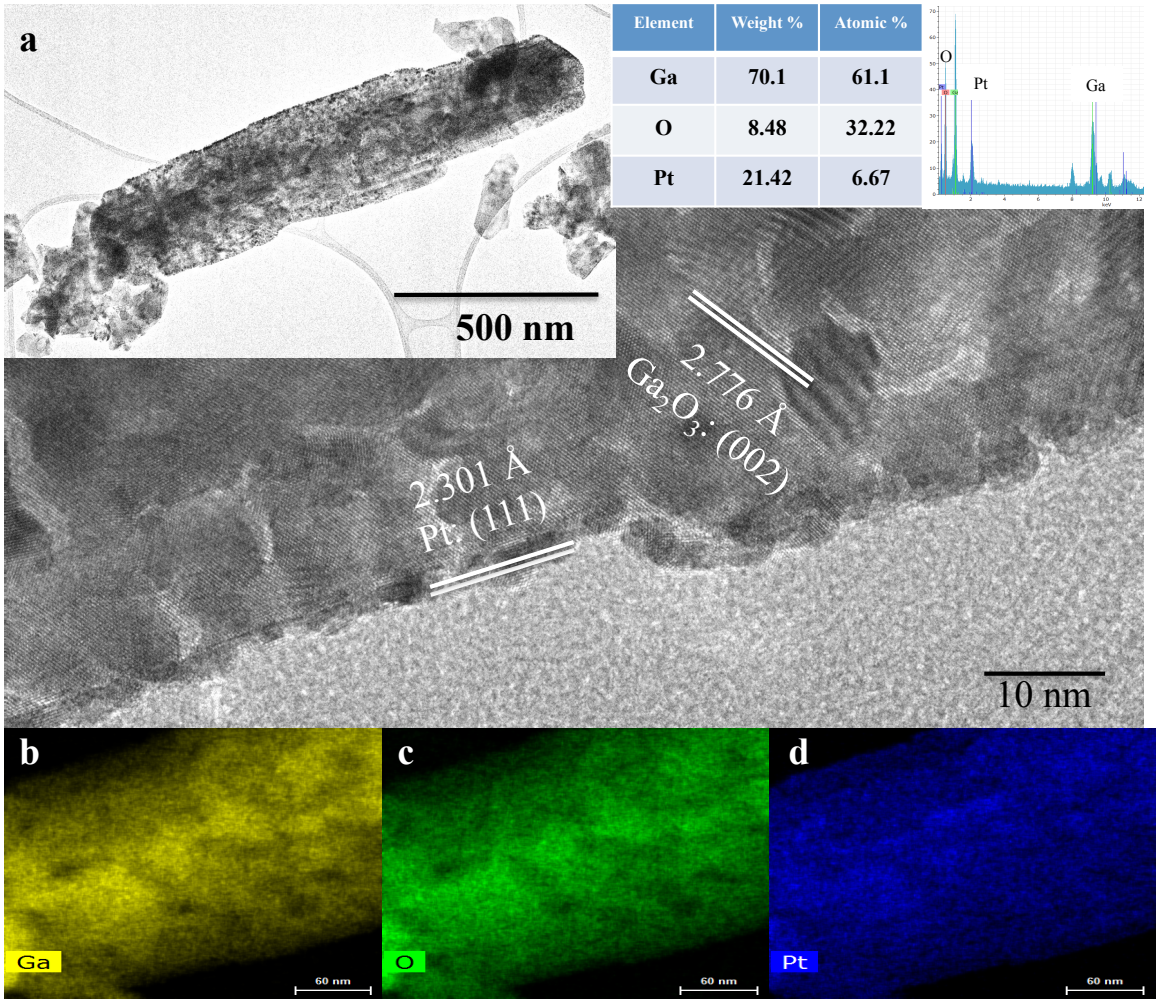

Figure 6-3: (a) TEM and high resolution images of a post annealing β-Ga_2O_3 nanorod coated with 1 nm Pt. The insets are the corresponding Energy-Disperse X-ray spectrum and composition analysis. (b)~(d) show the element mapping of 1 nm Pt-coated β-Ga_2O_3 nanorod, which present element distribution of Ga, O, Pt respectively.

Based on our previous study, we found LSFO nanoparticle surface decoration has an excellent gas sensing catalytic performance on β-Ga_2O_3 nanorods, comparable to that of Pt nanoparticle decoration.[17] In this study, we incorporated with ultra-violet light to tested the high temperature (500 °C) CO gas sensing properties of β-Ga_2O_3 nanord arrays with three different surface conditions: pristine, Pt-nanoparticle-decorated (1 nm or 5 nm nominal film thickness), and LSFO-nanoparticle-decorated as a comparison.

Figure 6-4(a) shows the dynamic sensing characteristics obtained from the pristine β-Ga_2O_3 nanord arrays sensor at 500 °C in high purity N_2 and in the gas mixture with 100 ppm CO balanced by N_2 and high purity N_2 was also used to recover the sensor. Upon exposure of the pristine β-Ga_2O_3 nanord arrays to CO, the current of β-Ga_2O_3 nanord arrays increases rapidly and display the behavior corresponding to on/off of UV light illumination with a response time (t_{90}, defined as the time when the normalized current change reached 90 % of the maximum response after the exposure to carbon monoxide) of 699 seconds without UV illumination and 623 seconds with UV light on at 500 °C, respectively. In addition, the sensor shows sensitivities of 6.3, 8.39 ~ 9.73 at CO concentration of 100 ppm under non-UV, UV illumination, respectively, which was shown in **Figure 6-4(b)**. That means the sensor can sustain in later cycles at high temperature, the sensor response towards twice exposure of 100 ppm carbon monoxide under UV illumination exhibited a reproducible response. Besides, UV light can further enhance the recovery ability since the recovery time decreases from 684 seconds of non-UV illumination condition to 488, 562 seconds under UV light illumination.

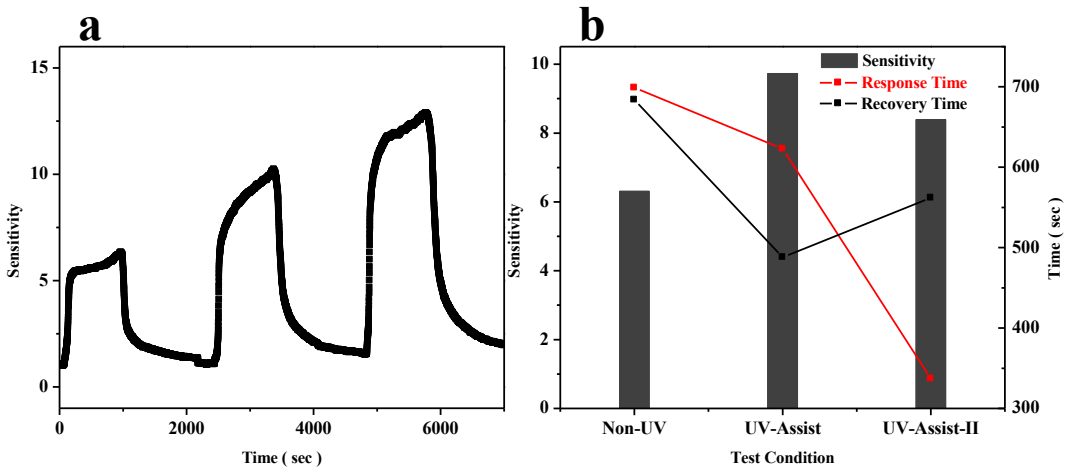

Figure 6-4: Carbon monoxide gas sensing test on pristine β-Ga_2O_3 nanorods array : (a) Normalized sensitivity-time characteristics of β-Ga_2O_3 nanorod arrays tested at 500 °C with N_2 as background atmosphere with/without UV light illumination; (b) Sensitivity, response and recovery time of CO gas sensing test under dark and UV illumination condition.

Figure 6-5 represents the CO gas sensing test results of pristine, 5 nm LSFO-, and 1 nm Pt- β-Ga_2O_3 nanorod arrays. In the case of LSFO surface decoration gas sensor, the sensitivity of 100 ppm CO gas was enhanced by 10.15 times compare to pure β-Ga_2O_3 nanorods array under non-UV illumination condition. Besides, UV- illumination can further improve the sensitivity to 77.56 while the sensitivity of LSFO- β-Ga_2O_3 nanorods is 63.9 under dark condition, shown in **Figure 6-5(b)**. However, the response time of LSFO nanoparticles decoration sample is a little longer than pure β-Ga_2O_3 nanorods, but the recovery time shows opposite effect, LSFO decoration can further decrease the recovery time, shown in **Figure 6-5(c)** and **(d)**.

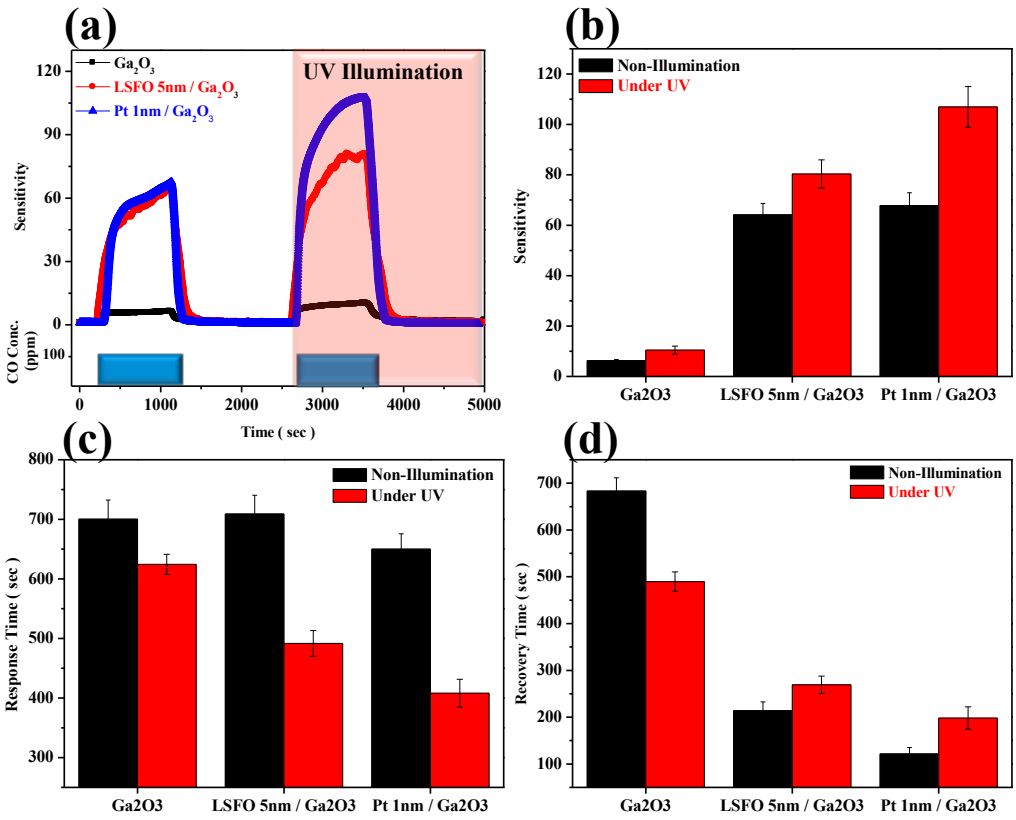

Figure 6-5: CO gas sensing test on pristine, surface decoration of LSFO- and Pt / β-Ga_2O_3 :(a) Normalized sensitivity-time characteristics; (b) sensitivity, (c) recovery time and (d) recovery time under dark or UV illumination tested at 500 °C.

On the other hand, the surface decorations of different nominal thickness of Pt-nanoparticles on β-Ga_2O_3 nanorod arrays were also studied, as shown in **Figure 6-6**. It shows that 1 nm Pt-nanoparticle-decoration can improve the sensitivity of CO to 68.49 that is similar to that of LSFO-nanoparticle-decoration sample. Surface decoration of 5 nm Pt-nanoparticle over β-Ga_2O_3 can further enhance the sensitivity to 300.08 at the same test condition.

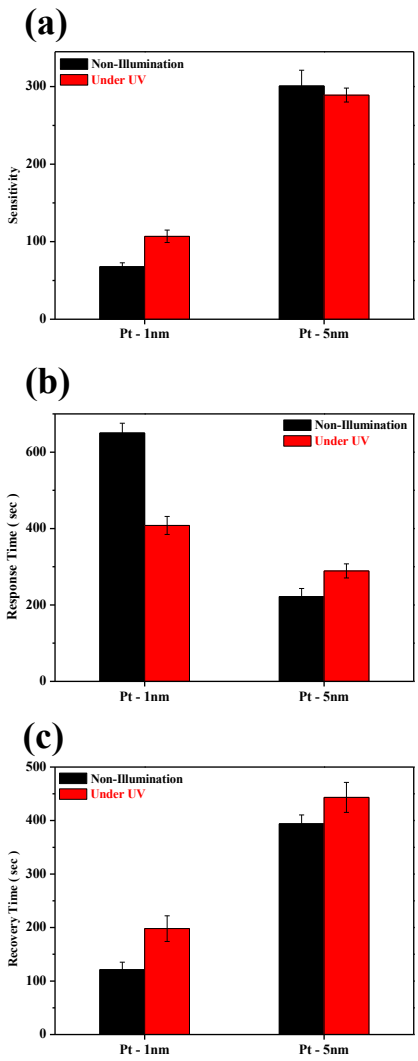

Figure 6-6: CO gas sensing test on 1 and 5 nm Pt-nanoparticle surface decoration of β-Ga_2O_3 (a): sensitivity, (b) response time and (c) recovery time.

It's believed the enhancement of gas sensing performance is originating from so called spillover effect. In the spill-over process, CO molecules are first efficiently adsorbed on the Pt nanoparticles surface and react with pre-adsorbed oxygen species on the nanorods with reduced activation energy, resulting in an efficient electron back-feeding into the charge depletion layer of β-Ga_2O_3. In addition, the Pt electric sensitization effect is further enhancing the gas sensing, further detail was described in our previous report.

Besides, the response time is 651 seconds and 222 seconds for 1 nm and 5 nm Pt-nanoparticle surface decoration, respectively. Compare with pristine β-Ga_2O_3 nanorod arrays, the surface decoration of Pt-nanoparticle can improve the performance of response time. As for recovery time, it's 122 and 393 seconds for 1 nm and 5 nm Pt-nanoparticle decoration accordingly.

However, under 254 nm UV illumination, the CO sensitivity can improve from 68.9 in dark circumstance to 189.9 for 1 nm Pt-decoration sample; the response time can deduce from 651 to 407 seconds, though recovery time shows opposite trend. In the case of 5 nm Pt-decoration, though, the CO sensitivity is from 300.08 in the dark to 289.9 under UV illumination, and response and recovery time both become even worse than dark condition. Therefore, under UV excitation and the surface decoration of Pt nanoparticles, the sensitivity can be enhanced by approximately 10-60 times.

All three test conditions, pristine β-Ga_2O_3 and surface decoration with LSFO or Pt nanoparticles, show the improvement of sensitivity, response and recovery time toward UV excited photocurrent which can add to the sensing signal.

Electron-hole pairs will be generated at the surface upon exposure to UV light with a photon energy larger than the band gap of β-Ga_2O_3. Since the band gap of β-Ga_2O_3 is around 4.9 eV, in this report, the wavelength of UV light is 254 nm that is capable to generate photocurrent in β-Ga_2O_3 nanorod. Some of the photo-generated electrons and holes will recombine with each other and many of the remaining photo-generated holes will react with negatively charged adsorbed oxygen ions on the surface according to the following reactions:

$$h^+ (h\nu) + O^{2+}(ads) \rightarrow O_2(g)$$

$$h^+ (h\nu) + O^-(ads) \rightarrow 1/2\ O_2(h\nu)$$

$$2h^+ (h\nu) + O^{2-}(ads) \rightarrow 1/2\ O_2(h\nu)$$

As a result of these reactions, the surface depletion layer in the β-Ga_2O_3 nanorod will be reduced. Upon exposure to CO gas, CO gas molecules reach the surface of β-Ga_2O_3 nanorod and react with remaining oxygen ions as follows:

$$CO + O_2^-(ad) \rightarrow O_2(g)$$

These reactions released electrons, which could enhance the carrier densities. Therefore, with the combination of photo response and photocatalytic processes, Ga_2O_3 exhibited large response to CO gas at 500 °C.

As described above, the addition of tiny LSFO nanoparticles to β-Ga_2O_3 could greatly increase the sensitivity to CO at high temperature under UV illumination. Here, we attempt to suggest a most likely sensing model for understanding the sensing behavior of the sensor using LSFO/Ga_2O_3 under UV illumination.

As we know, β-Ga_2O_3 is n-type and LSFO is p-type semiconductor. When the LSFO nanoparticles were sputtered on the surface of Ga_2O_3 nanorods, many local heterocontacts between the LSFO and β-Ga_2O_3 were formed. Since the Fermi energy level of LSFO is higher than that of Ga_2O_3, the electrons produced by UV illumination could transfer from the conduction band of LSFO to that of β-Ga_2O_3 and combined with the adsorbed oxygen on the surface of the β-Ga_2O_3 nanorods and increased the oxidation activity of the β-Ga_2O_3 nanorods. After CO gas is introduced into the system, CO molecules will further react with the pre-adsorbed oxygen ions and release electrons back to conduction band of

β-Ga_2O_3. Therefore, the carrier density of core β-Ga_2O_3 nanorods will increase according to the processes discussed above.

In the case of surface decoration with sputtered-Pt nanoparticles, the enhancement of CO gas by Pt-functionalization can be explained based on the models proposed for the metal catalyst-enhanced gas sensing of nanomaterials. Oxygen ions are spill over the β-Ga_2O_3 nanorod surface by the Pt nanoparticles and the chemisorption of CO gas is enhanced on the Pt nanoparticle surface owing to the catalytic or conductive nature of Pt. Consequently, combination of the spillover effect and the enhancement of chemisorption results in the enhanced electrical response of the Pt-functionalized β-Ga_2O_3 nanorod arrays to CO gas.

However, nominal thickness of 5 nm Pt nanoparticles decoration one shows inverse trend, since thicker nanoparticles will form locally conductive channel results in negligible UV photocurrent effect in this case.

6.4: Conclusion

In summary, large-scaled β-Ga_2O_3-based vertical nanorod arrays have been successfully fabricated on Si substrate using a two-step synthetic process. Gas sensing results show that UV illumination can enhanced the sensitivity of the pristine, LSFO-nanoparticle-, and Pt-nanoparticle-modified β-Ga_2O_3 nanorod arrays as exposure to CO gas at high temperature (500 °C). Under wavelength of 254 nm UV illumination, enhanced sensitivity of CO gas by 40-60 % for pristine β-Ga_2O_3 nanorod array at 500 °C since hole-electron pair can be generated by UV-Illumination and depletion layer can be tuned and thus enhance the sensitivity; with perovskite decoration of LSFO nanoparticles,

the sensitivity could be further enhanced due to the sensitizing effect. As for surface decoration of Pt-nanoparticle, the enhancement would be the combination of photocurrent and spill-over effect. However, thicker Pt would form locally continuous film resulting in negligible UV photocurrent effect.

Reference

1. Hamelers, H. V. M.; Schaetzle, O.; Paz-García, J. M.; Biesheuvel, P. M.; Buisman, C. J. N., Harvesting Energy from CO_2 Emissions. *Environ. Sci. Technol. Lett.* 2014, 1, 31-35.
2. Tuller, H. L., Materials for High Temperature Electrochemical Applications: Automotive Sensors, Catalysts and Traps. *Sens. Actuators, B* 2013, 187, 106-110.
3. Moos, R.; Izu, N.; Rettig, F.; Reiss, S.; Shin, W.; Matsubara, I., Resistive Oxygen Gas Sensors for Harsh Environments. *Sensors* 2011, 11, 3439-65.
4. Liu, Y.; Lei, Y., Pt-CeO_2 Nanofibers Based High-Frequency Impedancemetric Gas Sensor for Selective CO and C_3H_8 Detection in High-Temperature Harsh Environment. *Sens. Actuators, B* 2013, 188, 1141-1147.
5. Fergus, J. W., A Review of Electrolyte and Electrode Materials for High Temperature Electrochemical CO_2 and SO_2 Gas Sensors. *Sens. Actuators, B* 2008, 134, 1034-1041.
6. Fergus, J. W., Solid Electrolyte Based Sensors for the Measurement of CO and Hydrocarbon Gases. *Sens. Actuators, B* 2007, 122, 683-693.
7. Akbar, S.; Dutta, P.; Lee, C., High-Temperature Ceramic Gas Sensors: A Review. *Int. J. Appl. Ceram. Technol.* 2006, 3, 302-311.
8. Fergus, J. W., Perovskite Oxides for Semiconductor-Based Gas Sensors. *Sens. Actuators, B* 2007, 123, 1169-1179.
9. Fergus, J. W., Materials for High Temperature Electrochemical NO_x Gas Sensors. *Sens. Actuators, B* 2007, 121, 652-663.
10. Hodgkinson, J.; Tatam, R. P., Optical Gas Sensing: A Review. *Meas. Sci. Technol.* 2013, 24, 012004.
11. Romanosky, R. R., *Department of Energy / NETL Cross-Cutting Research: Sensor and Control Program Review Meeting* 2012.
12. Zhou, J.; Gu, Y.; Hu, Y.; Mai, W.; Yeh, P. H.; Bao, G.; Sood, A. K.; Polla, D. L.; Wang, Z. L., Gigantic Enhancement in Response and Reset Time of ZnO UV Nanosensor by Utilizing Schottky Contact and Surface Functionalization. *Appl. Phys. Lett.* 2009, 94, 191103.
13. Mello, M.; Potì, B.; Risi, A. d.; Passaseo, A.; Lomascolo, M.; Vittorio, M. D., GaN Optical System for CO and NO Gas Detection in the Exhaust Manifold of Combustion Engines. *J. Opt. A: Pure Appl. Opt.* 2006, 8, S545-S549.

14. Lettieri, S.; Setaro, A.; Baratto, C.; Comini, E.; Faglia, G.; Sberveglieri, G.; Maddalena, P., On the Mechanism of Photoluminescence Quenching in Tin Dioxide Nanowires by NO_2 Adsorption. *New J. Phys.* 2008, 10, 043013.
15. Faglia, G.; Baratto, C.; Sberveglieri, G.; Zha, M.; Zappettini, A., Adsorption Effects of NO_2 at ppm Level on Visible Photoluminescence Response of SnO_2 Nanobelts. *Appl. Phys. Lett.* 2005, 86, 011923.
16. Lettieri, S.; Setaro, A.; De Stefano, L.; De Stefano, M.; Maddalena, P., The Gas-Detection Properties of Light-Emitting Diatoms. *Adv. Func. Mater.* 2008, 18, 1257-1264.
17. Lin, H.-J.; Baltrus, J. P.; Gao, H.; Ding, Y.; Nam, C.-Y.; Ohodnicki, P.; Gao, P.-X., Perovskite Nanoparticle-Sensitized Ga_2O_3 Nanorod Arrays for CO Detection at High Temperature. *ACS Appl. Mater. Interface* 2016, 8, 8880-8887.

CHAPTER 7

H_2 Treatment Effect of Porous Ga_2O_3 Nanorod Array based Gas Sensors at High Temperature

Metal oxide-based sensors have played a key role in detection of toxic, flammable and combustible gases in the past few decades, but most of these sensors usually are operated under comparatively low temperatures. Although reducing the operation temperature close to room temperature is energy saving in perspective of practical application, it is still an unwavering grand challenge to realize *in situ* or real-time detection and monitoring of combustion progresses in fossil-fueled power plants, vehicle engines at high temperature. Here in this work, we report a readily defect-tuning strategy to accomplish high sensitivity and short response time, two of the most important parameters in metal oxide-based gas sensors at high temperature.

Specifically, porous crystalline gallium oxide (Ga_2O_3) nanorod arrays after different hydrogen (H_2) treatments have been prepared by using a hydrothermal synthesis, post annealing in ambient and H_2 atmosphere at different temperatures. The resulting H_2-treated Ga_2O_3 material serves as an efficient high temperature gas-sensing material for specific carbon monoxide (CO) detection with both high sensitivity, and fast response and recovery. Such a hydrogen treatment strategy is anticipated to provide a promising motivation for rational design of various gas sensing devices at high temperature.

7.1: Introduction

It is highly desirable to detect and monitor toxic, combustible and flammable gases efficiently in both industry settings and community neighborhood. Great efforts have

been made for designing and fabricating effective gas sensors that are both of high performance and of low cost for practical applications. Therefore, metal oxide semiconductor materials attract attention and become the most-widely used gas sensors because of their low cost of manufacture, high stability and good performance.[1, 2] The mechanism of semiconductor gas sensors is based on the interaction between the chemisorbed oxygen species on the surface of semiconductor material and the targeted gas molecules, which would lead to the alteration in the electrical resistance. So far, semiconducting metal oxides such as SnO_2,[3-6] ZnO,[7-9] TiO_2[10-12] have been extensively investigated as gas sensors because of their good sensing performance and low cost. Most of these work focus on low working temperature region ranging from room temperature to around 200 °C. Reducing the operation temperature down to room temperature could really extend the applications of semiconductor sensors in daily life, need less heating element with lower energy consumption and enhanced operation safety.

However, monitoring combustion and emission process at high temperature is extreme important from -energy-saving perspective.[13] With an instant feedback of the gas compositions detected in the internal combustion engine, the efficient injection of oxygen or fuel can be readily controlled.[14] Therefore, the optimal combustion efficiency and less exhaust emission can be reached at the same time. Thus, suitable gas sensors are demanded at high temperature toward monitoring combustion and emission processes. The sensors used for *in situ* and real-time gas detection should sustain temperatures above 600 °C.

In automotive engines, exhaust aftertreatment systems and fossil-fueled power plants, the major exhausts are carbon monoxide (CO), hydrocarbons (HCs), nitric oxide (NO)

and nitrogen dioxide (NO_2).[15] Carbon monoxide is a colorless, odorless, toxic gas formed when carbon is not fully burned in fuels and automobile exhaust gases contribute to around 60 % CO emission.[16, 17] High temperature CO gas sensors are on demand in order for controlling the emission of CO due to its toxicity to human health. In addition, since CO is a strong reducing gas and could irreversibly interact with many sensing materials and lead to dysfunctional sensors.[18] Hence, *in situ* detection of CO is critical for monitoring combustion processes at high temperatures. Typical binary metal oxide CO gas sensors reported can operate at mild temperatures (< 700 °C). However, the exhaust gas temperatures of some engines can reach 1000 °C, which require very high thermal stability on the sensor devices.

Various metal oxides have been investigated for applications in high temperature environments.[15, 19-25] Amongst them, gallium oxide is one of the most promising materials as high temperature sensors due to its high thermal and chemical stability. Thin-film based Ga_2O_3 gas sensors have been demonstrated as promising oxygen sensors at high temperatures ranging from 600-1000 °C and can also detect reducing gases such as H_2 or CO, etc. at high temperatures.[20, 26, 27] However, the conventional thin film technology has its intrinsic limitations because the total surface area and sensing performance will be influenced in the process of sensor device miniaturization. Therefore, for the purpose of increasing the surface that can react with the target gas, nanorods have been investigated with decreased size and increased surface-to-volume ratio and shown promising results as chemical sensors.[6, 7, 28, 29]

In this section, a novel wide band-gap β-Ga_2O_3 (~ 4.9 eV) nanorod arrays were successfully synthesized on Si substrates by combining a hydrothermal method and high

temperature calcination. Currently, β-Ga_2O_3 high temperature gas sensors have been investigated by several methods such as surface functionalization,[30, 31] heterojunction and ultra-violet illumination-assisted to improve the sensing performance.[32] In addition, in ceramic materials exemplified by metal oxides, point defects including electronic and ionic defects directly contribute to the electrical conduction that help generate the resistive type sensor signals. Through thermal annealing of materials under different atmospheres at different temperatures, the point defect configurations and populations can be varied. Here, we used hydrogen gas to treat Ga_2O_3 at different temperature in order to introduce oxygen related point defects such as vacancies to tune and improve the sensor performance.

7.2: Experimental

7.2.1: Precursor, Substrate and Sputtering Target Chemicals

(I) Gallium(III) nitrate hydrate ($Ga(NO_3)_3 \cdot 9H_2O$, 99.9998%): the gallium salt of nitric acid was purchased from Acros Organics. It's a white, slightly hygroscopic and crystal powder with good solubility in water. It's used as the precursor of hydrothermal synthesis in this work.

(II) Tin dioxide (SnO_2, >99.9%): the inorganic compound target with diameter 2" and 0.25" in thickness was purchased from Stanford Advanced Materials. The white circular target was used as the seed layer for further hydrothermal synthesis.

(III) Silicon (Si, (100)): substrates (boron doped, p-type, 1~10 ohm-cm, 100 mm in diameters, 500 μm in thickness, single flat, single side polish) topped with 1μm silicon dioxide (SiO_2) were purchased from University Wafer.

7.2.2: Preparation Ga_2O_3 Nanorod Arrays and Post-Hydrogen Treatments

Before synthesis, Si substrates were immersed in acetone solution and sonicated for 5 minutes and rinsed for another 5 minutes by deionized (DI) water to remove surface grease and organic deposits in the first place. And then holding Si substrate tilt and using N_2 to purge the surface in one direction from high to low to remove the residual water on each side of the surface of Si substrates. Next, a SnO_2 seed layer with 50 nm thickness was sputtered on Si substrates by RF magnetron sputtering system and followed by ambient post-annealing to make it crystalline at 900 °C for 2 hours. Afterwards, gallium hydroxide (GaOOH) nanoroad arrays were fabricated on Si/SiO_2 substrates through hydrothermal method. By dissolving 0.6 g $Ga(NO_3)_3 \cdot 9\ H_2O$ in 40 mL deionized (DI) water and stirred for 10 minutes, a $Ga(NO_3)_3$ solution with the pH value controlled at around 2 was prepared. Pour the prepared solution into the Teflon bottle and fix the Si substrates, vertical GaOOH nanorod arrays were then grown on SnO_2 seed layer of the Si substrates incubated in the precursor solution at 150 °C for 12 hours for the hydrothermal growth. After the growth process, the fabricated GaOOH nanorod arrays samples were then washed by DI water couple times and dried at 80 °C in the ambient atmosphere, and next annealed at 1000 °C for 4 hours to convert into pure β-Ga_2O_3 nanorod arrays completely.

Hydrogen treatments:

Post-hydrogen treatments applied on Ga_2O_3 nanorod arrays were accomplished on ChemiSorb 2720 Pulse Chemisorption System, Micromeritics Instrument Corporation. Ga_2O_3 nanorod arrays were put into the tube sample cell and fixed on the system under 10

% H_2 in N_2 with a flow rate of 25 standard cubic centimeters per minute (sccm). The ramping rate is 20 °C / minute and the duration time of each temperature is 30 minutes.

7.2.3: Gas Sensing Test Setup and Installation of the Device

The high temperature gas sensing properties of β-Ga_2O_3 nanorod arrays were tested by monitoring the potentiostatic current response of the β-Ga_2O_3 nanorod array device to carbon monoxide (CO) exposure in a high temperature tube furnace equipped with an alumina tube, electrical feedthroughs (Ni/Cr lead wires), and a gas injection system. Pt wires (10 μm diameter) were used to connect the nanorod gas sensor placed in the center position of the tube to Ni/Cr lead wires, which were externally connected to an electrochemical work station (CHI 601C). The nanorod sensor was subjected to a fixed 1 volt direct current (DC) bias while being heated from room temperature to 500 °C in air with a heating rate of 20 °C/min. Gas sensing tests were then performed at 500 °C under varying concentration of CO (N_2 balance; from 20, 50, 80, and to 100 ppm; total chamber pressure 1 atmosphere). The responses of the nanorod sensor to CO were evaluated by measuring the magnitude of current change upon the exposure to various concentrations of CO under a dynamic gas flow condition with a constant flow rate of 1.5 L/min (high purity N_2 as carrier gas), which was regulated by a computer-controlled gas mixing system (S-4000, Environics Inc., USA). The desired CO concentrations can be achieved by 2 % CO cylinder connected to one port of the system and diluted by another pure nitrogen cylinder connected in another port of the gas mixing system. In detail, the nanorod sensor device was first exposed to CO/N_2 mixture for 16 min, followed by high purity N_2 purge for 24 minutes (i.e., one gas exposure cycle) to recover the sensor, and

then multiple exposure cycles were repeated. We define the device gas sensitivity as: (R_0 / R_{CO}) -1, where R_{CO} is the resistance under CO/N_2 mixture and R_0 is the resistance under high purity N_2. The response time is defined as 'the time duration required for gas sensitivity to reach 90 % upon exposure of a sensor to CO', and recovery is defined as 'the time duration required for the gas sensitivity to decrease to 10 % of the sensitivity upon the termination of CO injection.

7.3: Results and Discussion

The as-synthesized orthorhombic structured GaOOH with preferred orientation instead of random orientation powdered GaOOH and and pure β-Ga_2O_3 nanorod arrays obtained by post annealing at 1000 °C for 4 hours were first demonstrated by other reports in our group.[30] Furthermore, the length of the as-synthesized GaOOH nanorod grown perpendicularly to the Si substrates is around 1.8 μm and the diagonal length of the diamond shaped tip is around 200 nm on either GaOOH or β-Ga_2O_3 nanorod.

The XRD patterns of pure β-Ga_2O_3 nanorod arrays and the samples with post hydrogen treatments at different temperatures such as 300, 400, 500 °C were shown in **Figure 7-1(a)**, **(b)**, **(c)** and **(d)** respectively, where most of the peaks match monoclinic β-Ga_2O_3 and few peaks from SnO_2 which acts as the seed layer in the hydrothermal synthesis process. Basically there's no peak other than monoclinic β-Ga_2O_3 been found after post hydrogen treatments.

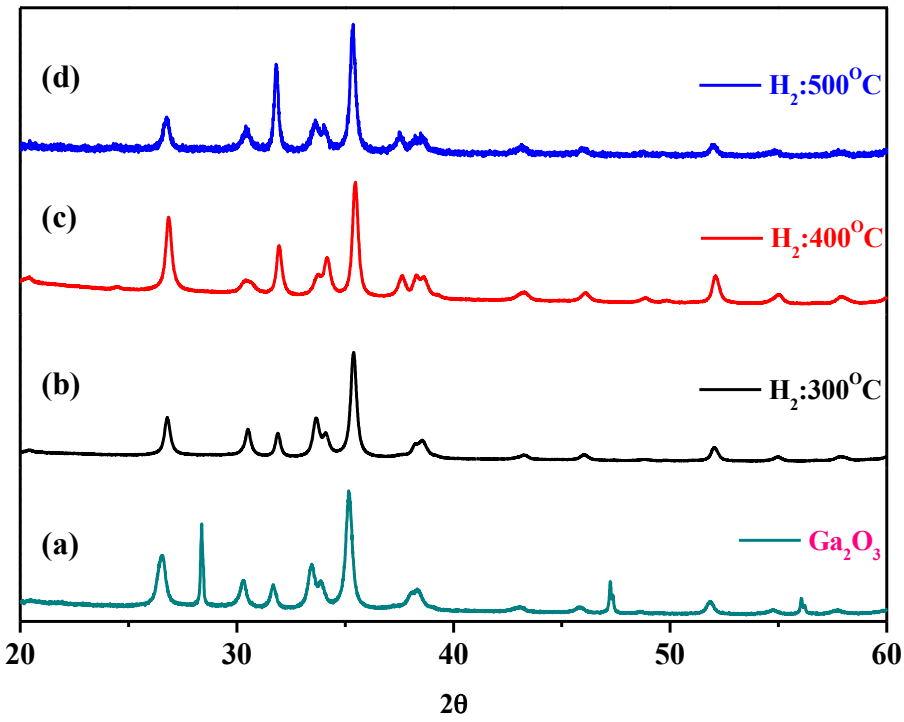

Figure 7-1: X-ray diffraction patterns of (a) pristine Ga_2O_3 nanorod arrays, and post-hydrogen treatments on (b) 300 °C, (c) 400 °C and (d) 500 °C for 30 minutes.

The top views and 45°-tilted view SEM images of β-Ga_2O_3 nanorod arrays treated with post hydrogen annealing at 300, 400, 500 °C were shown in **Figure 7-2**. Based on the pictures from both top and tilt view, morphology did not change much. The samples after post hydrogen treatments at different temperatures still keep diamond-shaped like tip surfaces.

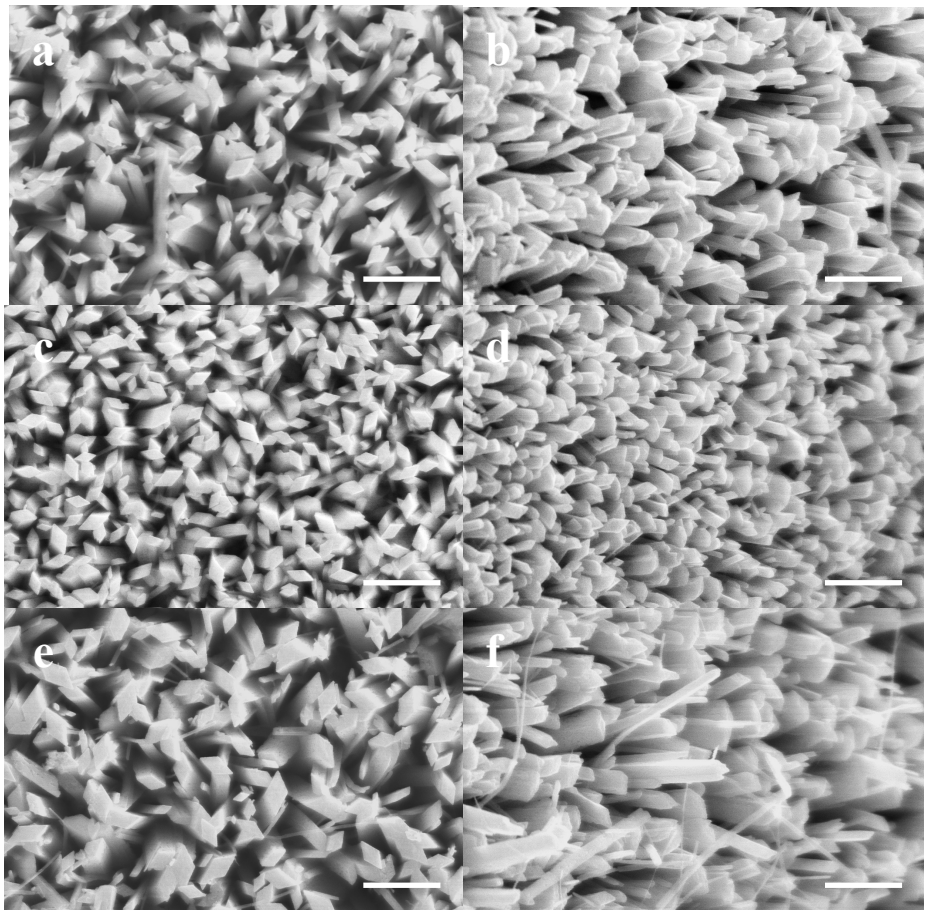

Figure 7-2: SEM images of the hydrogen treated Ga_2O_3 samples: (a) (b)(c) (d) are top view and (e) (f) (g)(h) are tilt 45 degree view pictures of hydrogen treatment at 300, 400, 500 °C respectively.

While in the gas sensing tests, we found that post hydrogen treatments has an excellent gas performance on β-Ga_2O_3 nanorods. **Figure 7-3(a)** shows the dynamic sensing characteristics of the pure β-Ga_2O_3 nanorod arrays sensor toward four different CO gas concentrations (20, 50, 80 and 100 ppm in N_2 balance at high temperature (500 °C). The results show the base sensitivity of pristine β-Ga_2O_3 nanorod arrays is around 2 to 4 within CO concentrations ranging from 20 to 100 ppm at 500 °C. Besides, CO sensitivity basically increases as CO concentrations increase. The dynamic characteristics of β-Ga_2O_3 nanorod arrays sensors with post hydrogen annealing at different temperatures

were shown in **Figure 7-3(b)**. It clearly shows that hydrogen treatment at 400 °C can improve CO sensitivity to about 20 at 20 ppm which is almost 10 times larger compare with pristine β-Ga_2O_3 nanorod arrays sensors.

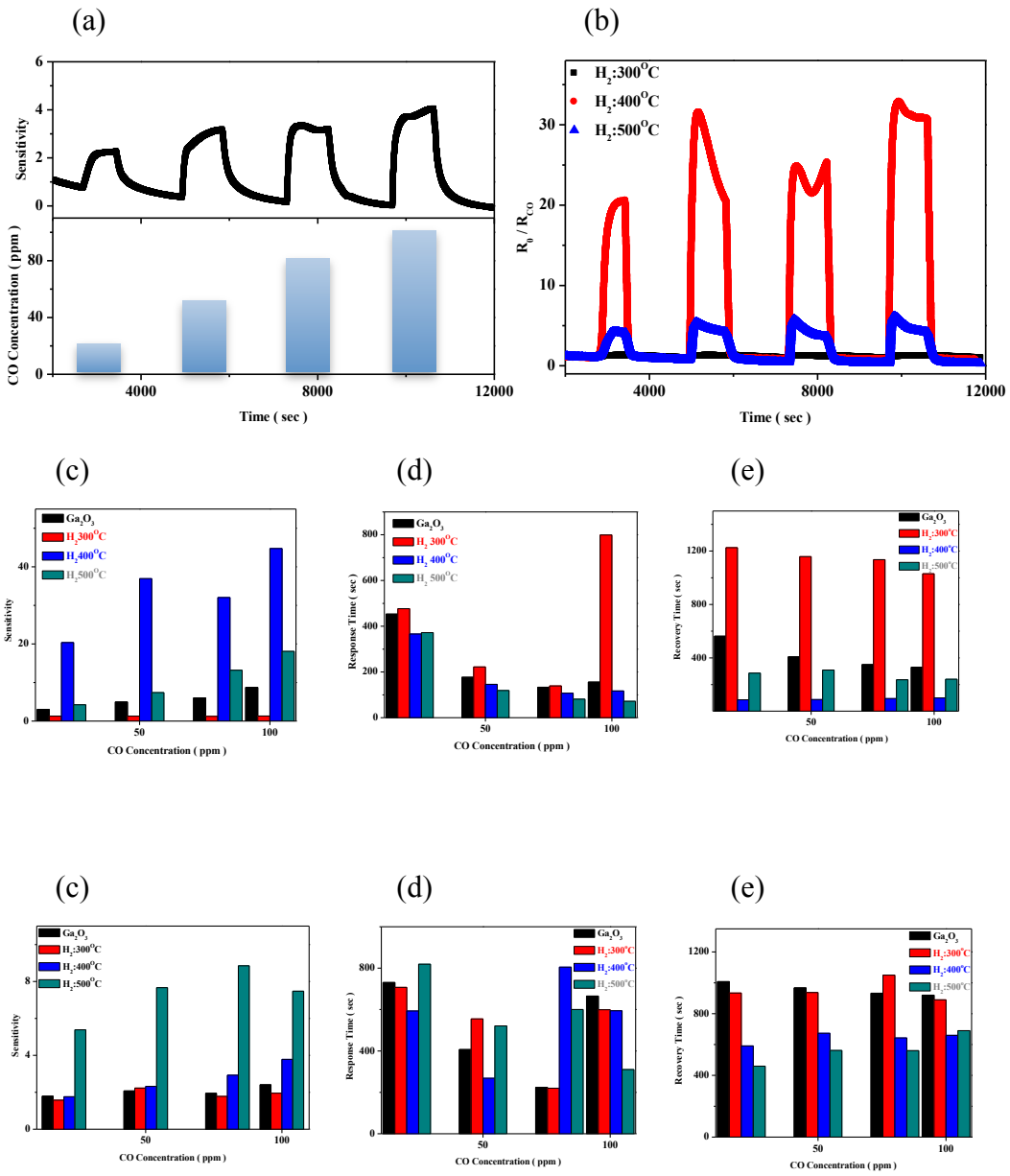

Figure 7-3: (a) Dynamic CO sensing characteristic of Ga_2O_3 nanorod arrays and (b) post-hydrogen treatments at different temperatures toward different CO concentrations at 500 °C. (c) sensitivity, (d) response time and (e) recovery time of gas sensor performance at 500 °C, (e) sensitivity, (f) response time and (g) recovery time at 800 °C.

Figure 7-3 (c) shows CO sensitivity of pristine β-Ga_2O_3 and the samples with post hydrogen treatment at different temperatures. It shows that the sensitivities after hydrogen treatments at 400 and 500 °C increase with respect to increasing CO concentration from 20 to 100 ppm. However, post hydrogen treatment at 400 °C yielded the best CO sensitivity in treated β-Ga_2O_3 nanorod arrays sensor, which is of ~10 times enhancement at CO concentrations between 20-100 ppm at 500 °C in comparison with β-Ga_2O_3 nanorod arrays sensor. The possible reason might be due to the increase of the oxygen vacancies induced by post hydrogen treatment; these defects can preferentially absorb more oxygen ions at these defect sites and thus provide more reaction sites for CO gas molecules that contribute to the sensing signals. After CO gas was injected, there were more and more electrons exchange at these defects sites and increase sensitivity.

Similar results were also observed at 800 °C shown in **Figure 7-3(f)**, post hydrogen treatments at both 400 and 500 °C improve the sensitivity in CO concentration range from 20 to 100 ppm. The sensitivity of post hydrogen treatment at 500 °C also improves to around 3 folds at 800 °C. However, the dominant sensing mechanism is different at different testing temperatures. Defects and defects distribution will be dominated at 800 °C and surface pre-adsorbed oxygen species can be dominated at 500 °C, thus post hydrogen treatment at different temperature will give different contribution to CO sensitivity at testing temperature of 500 or 800 °C.

In addition, post hydrogen treatment also improves response and recovery properties. For the test at 500 °C, post hydrogen treatment at either 400 or 500 °C can reach about 85 % of response time compared with pure β-Ga_2O_3 which was shown in **Figure 7-3(d)**. **Figure 7-3(e)** depicts that the recovery time can improve to about 20 % of β-Ga_2O_3. When the gas sensing

test was operated at 800 °C, however, post treatment at 500 °C did not improve the response performance but recovery time can reach about 40 % of β-Ga_2O_3 at 20 ppm CO and about 70 % at 100 ppm CO which was shown in **Figure 7-3(g)** and **Figure 7-3(h)**.

Besides, *in-situ* nitrogen dioxide detection at 800 °C had also been tested on pristine β-Ga_2O_3 and post-annealed samples. **Figure 7-4(a)** depicts the typical electrical responses of the pristine β-Ga_2O_3 nanorod arrays sensor as a function of time upon periodic exposure to NO_2 with concentration of 100, 200 and 300 ppm balanced in high purity N_2. In order to fully recover the sensor and repeat the test, high purity N_2 was used to purge the surface of the sensor for the recovery, indicating the purging N_2 leads to quick desorption of nitrogen dioxide molecular attached on the surface of β-Ga_2O_3 nanorod. The results showed the pristine β-Ga_2O_3 nanorod arrays sensor is a fast, reproducible, sensitive sensor upon exposure to nitrogen dioxide, and therefore, β-Ga_2O_3 nanorod arrays sensor shows a promising result as a high temperature nitrogen dioxide sensor.

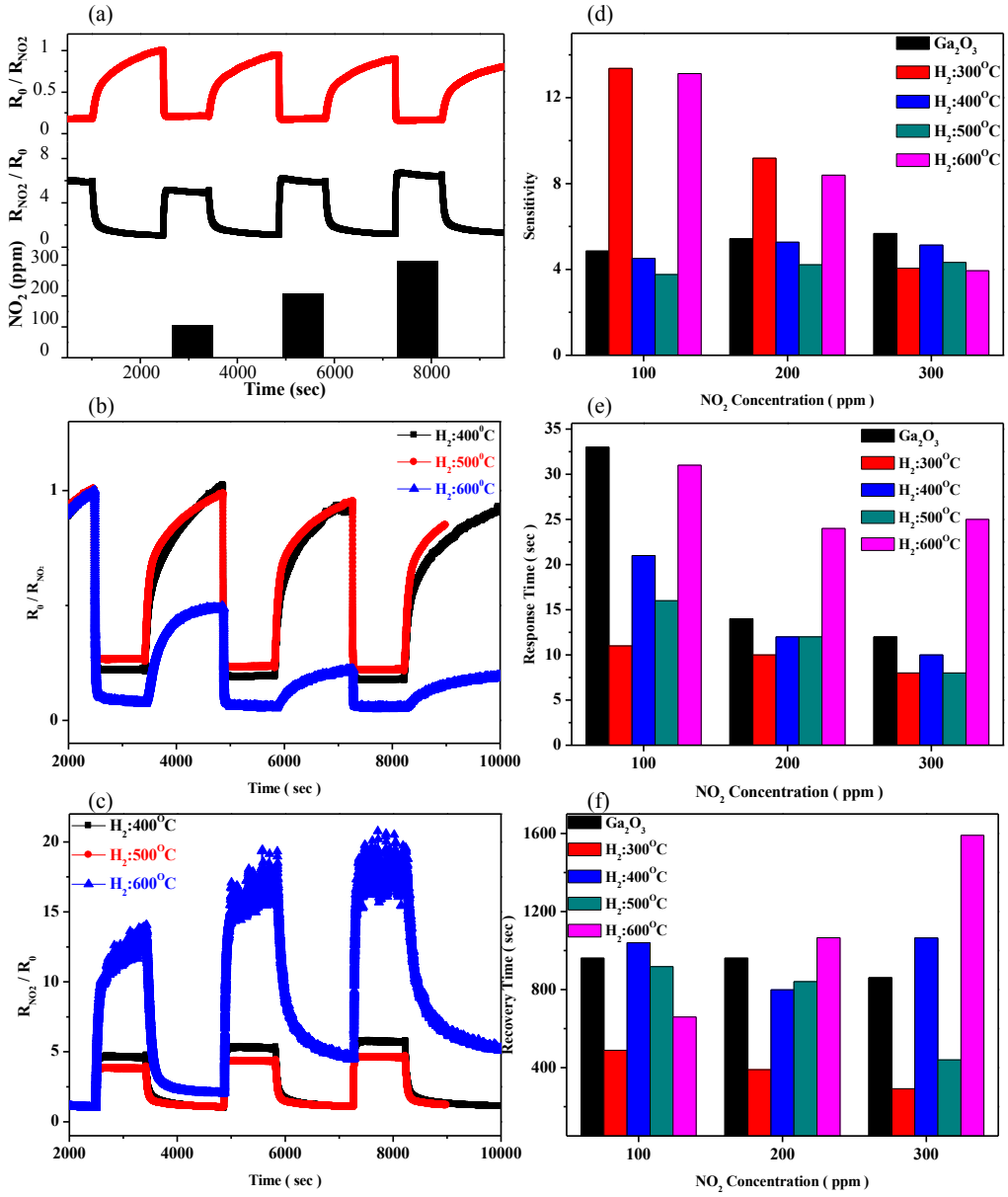

Figure 7-4: (a) Dynamic NO_2 sensing characteristic of pristine Ga_2O_3 nanorod arrays and (b), (c) post-hydrogen treatment samples toward different NO_2 concentrations at 800 °C, (d) sensitivity, (e) response time and (f) recovery time of NO_2 gas sensor performance at 800 °C

The dynamic electrical responses of β-Ga_2O_3 nanorod arrays samples treated with post hydrogen treatments with exposure to the same NO_2 condition were shown in **Figure 7-4(b)**.

The results indicate that these samples has fast response time as well, however, N_2 can also be used to fully recover except the sample treated at 600 °C. The dynamic sensitivity was converted and shown in **Figure 7-4(c)**. **Figure 7-4 (d)**, **(e)** and **(f)** represent the sensitivity, response time and recovery time on different contents of NO_2 gas of pristine β-Ga_2O_3 and post hydrogen treatment samples tested at 800 °C, respectively. Hydrogen treatment at 300 °C can increase sensitivity around 10 % compared with pure β-Ga_2O_3 sample. For response time, basically, gas sensors based on post hydrogen treated β-Ga_2O_3 have fast response on NO_2. For β-Ga_2O_3 sensor, it just takes 19 seconds to detect 100 ppm NO_2. And after hydrogen treatment at 300 °C, the response time can further decrease to just 13 seconds which is just 68 % response time of pure β-Ga_2O_3 sample.

Based on the results shown above, it's clearly seen the conductivity of β-Ga_2O_3 nanorod arrays increased upon exposure to reducing gas CO, decreased toward oxidizing gas NO_2, which indicate β-Ga_2O_3 is an n-type gas sensor. In addition, the classic mechanism of electrical conductivity for β-Ga_2O_3 material has been reported as the following equation:

$$Ga_2O_3 \leftrightarrow 2Ga_{Ga}^{x} + 2O_O^{x} + V_O^{*} + e^{-} + \tfrac{1}{2} O_2$$

where Ga_{Ga}^{x} and O_O^{x} represent the regular lattice ions, while V_O^{*} is the charged defect with single ionized oxygen vacancy. These oxygen vacancies and the electrons trapped by lattice Ga are the intrinsically predominant point defects of β-Ga_2O_3. These defects have been invoked as most possible sources to affect the properties of β-Ga_2O_3. Therefore, by control the defects concentrations in β-Ga_2O_3 nanorods can in turn change

the sensing performances. The existence of such defects exerts profound influence on the performance of electronic devices and as a result methods for their modification are of interest.

Hydrogen annealing has been known to be an effective way of desorbing the oxygen sites on the surface of metal oxides which act to introduce more oxygen vacancies, thereby increasing the conductivity. Since electronegativity of the oxygen is larger than that of Ga, oxygen is desorbed from the surface through the annealing process.

Since β-Ga_2O_3 nanorods consist of very high surface areas, which could exhibit significant strains on the bonds near the surface due to their small diameters, and thus hydrogen react with the surface bonds on the β-Ga_2O_3 and would break Ga-O bonds easily. Therefore, this process would lead to an oxygen deficit in the structure and would increase the concentration of the oxygen vacancy.

Another possible explanation is that oxygen vacancies would act as preferential adsorption sites for targeting gases. Several theoretical predictions have been demonstrated that surface defects dominate the electronic or chemical properties and adsorption behaviors of metal oxide surfaces for many years.[33]

Density functional theory showed that the adsorption energy of the gases molecules on the oxygen-vacancy site is significantly increased, larger than that on the perfect site. Thus, charge transfer from the oxygen-vacancy site to gases molecules is much larger than that from the perfect site to gases molecules. That's to say that oxygen vacancies bind more tightly with gases molecules and thus attracting more charge from the surface of β-Ga_2O_3 nanorods compared with oxygen-vacancy-free β-Ga_2O_3 surface.

On defect-free surface, current drop by NO_2 adsorption is due to the interaction between NO_2 molecules and surface Ga atoms, formatting the bridging nitrate groups. When oxygen vacancies are introduced in the surface of β-Ga_2O_3 nanorods, an additional current drop is expected upon interaction of oxygen with oxygen vacancies and the neighboring Ga atoms.

7.4: Conclusion

In summary, post hydrogen treatment can induce more oxygen vacancies into β-Ga_2O_3 nanorods and thus enhance sensitivity of CO at high temperature. Creation of more oxygen defects can generate more electrons and thus more oxygen species formed on the surface of β-Ga_2O_3. Oxygen vacancy acts as preferential adsorption sites for CO molecules. In addition, response and recovery time can be improved as well. Such improvements can also been found in the test of NO_2 at high temperature 800 °C.

Reference

1. Korotcenkov, G., Metal Oxides for Solid-State Gas Sensors: What Determines Our Choice? *Mater. Sci. Eng., B* 2007, 139, 1-23.
2. Franke, M. E.; Koplin, T. J.; Simon, U., Metal and Metal Oxide Nanoparticles in Chemiresistors: Does the Nanoscale Matter? *Small* 2006, 2, 36-50.
3. Maeng, S.; Kim, S.-W.; Lee, D.-H.; Moon, S.-E.; Kim, K.-C.; Maiti, A., SnO_2 Nanoslab as NO_2 Sensor: Identification of the NO_2 Sensing Mechanism on a SnO_2 Surface. *ACS Appl. Mater. Interfaces* 2014, 6, 357-63.
4. Huang, H.; Tian, S.; Xu, J.; Xie, Z.; Zeng, D.; Chen, D.; Shen, G., Needle-Like Zn-Doped SnO_2 Nanorods with Enhanced Photocatalytic and Gas Sensing Properties. *Nanotechnology* 2012, 23, 105502.
5. Liu, Y.; Koep, E.; Liu, M., A Highly Sensitive and Fast-Responding SnO_2 Sensor Fabricated by Combustion Chemical Vapor Deposition. *Chem. Mater.* 2005, 17, 3997-4000.
6. Kolmakov, A.; Zhang, Y.; Cheng, G.; Moskovits, M., Detection of CO and O_2 Using Tin Oxide Nanowire Sensors. *Adv. Mater.* 2003, 15, 997-1000.

7. Park, S.; An, S.; Ko, H. K.; Jin, C.; Lee, C., Synthesis of Nanograined ZnO Nanowires and Their Enhanced Gas Sensing Properties. *ACS Appl. Mater. Interfaces* 2012, 4, 3650-6.
8. Chen, M.; Wang, Z.; Han, D.; Gu, F.; Guo, G., Porous ZnO Polygonal Nanoflakes: Synthesis, Use in High-Sensitivity NO_2 Gas Sensor, and Proposed Mechanism of Gas Sensing. *J. Phys. Chem. C* 2011, 115, 12763-12773.
9. Zhang, J.; Wang, S.; Xu, M.; Wang, Y.; Zhu, B.; Zhang, S.; Huang, W.; Wu, S., Hierarchically Porous ZnO Architectures for Gas Sensor Application. *Cryst. Growth Des.* 2009, 9, 3532-3537.
10. Moon, H. G.; Shim, Y.-S.; Su, D.; Park, H.-H.; Yoon, S.-J.; Jang, H. W., Embossed TiO_2 Thin Films with Tailored Links between Hollow Hemispheres: Synthesis and Gas-Sensing Properties. *J. Phys. Chem. C* 2011, 115, 9993-9999.
11. Wang, C.; Yin, L.; Zhang, L.; Qi, Y.; Lun, N.; Liu, N., Large Scale Synthesis and Gas-Sensing Properties of Anatase Tio_2 Three-Dimensional Hierarchical Nanostructures. *Langmuir* 2010, 26, 12841-12848.
12. Kim, I.-D.; Rothschild, A.; Lee, B. H.; Kim, D. Y.; Jo, S. M.; Tuller, H. L., Ultrasensitive Chemiresistors Based on Electrospun TiO_2 Nanofibers. *Nano Lett.* 2006, 6, 2009-2013.
13. Moos, R.; Izu, N.; Rettig, F.; Reiss, S.; Shin, W.; Matsubara, I., Resistive Oxygen Gas Sensors for Harsh Environments. *Sensors* 2011, 11, 3439.
14. Tuller, H. L., Materials for High Temperature Electrochemical Applications: Automotive Sensors, Catalysts and Traps. *Sens. Actuators, B* 2013, 187, 106.
15. Akbar, S.; Dutta, P.; Lee, C., High-Temperature Ceramic Gas Sensors: A Review. *Int. J. Appl. Ceram. Technol.* 2006, 3, 302.
16. Hjiri, M.; El Mir, L.; Leonardi, S. G.; Pistone, A.; Mavilia, L.; Neri, G., Al-Doped ZnO for Highly Sensitive CO Gas Sensors. *Sens. Actuators, B* 2014, 196, 413-420.
17. Chiang, Y.-J.; Pan, F.-M., PdO Nanoflake Thin Films for CO Gas Sensing at Low Temperatures. *J. Phys. Chem. C* 2013, 117, 15593-15601.
18. Wu, J.; Gross, A.; Yang, H., Shape and Composition-Controlled Platinum Alloy Nanocrystals Using Carbon Monoxide as Reducing Agent. *Nano Lett.* 2011, 11, 798-802.
19. Francioso, L.; Presicce, D. S.; Siciliano, P.; Ficarella, A., Combustion Conditions Discrimination Properties of Pt-doped TiO_2 Thin Film Oxygen Sensor. *Sens. Actuators, B* 2007, 123, 516-521.
20. Bartic, M.; Ogita, M.; Isai, M.; Baban, C.-L.; Suzuki, H., Oxygen Sensing Properties at High Temperatures of β-Ga_2O_3 Thin Films Deposited by the Chemical Solution Deposition Method. *J. Appl. Phys.* 2007, 102, 023709.
21. Izu, N.; Shin, W.; Murayama, N., Fast Response of Resistive-Type Oxygen Gas Sensors Based on Nano-Sized Ceria Powder. *Sens. Actuators, B* 2003, 93, 449-453.
22. Izu, N.; Shin, W.; Murayama, N.; Kanzaki, S., Resistive Oxygen Gas Sensors Based on CeO_2 Fine Powder Prepared Using Mist Pyrolysis. *Sens. Actuators, B* 2002, 87, 95-98.
23. Savage, N. O.; Akbar, S. A.; Dutta, P. K., Titanium Dioxide Based High Temperature Carbon Monoxide Selective Sensor. *Sens. Actuators, B* 2001, 72, 239-248.
24. Bene, R. P., Z.; Perczel, I.V.; Fleischer, M.; Reti, F., High-Temperature Semiconductor Gas Sensors. *Vacuum* 2001, 61, 275-278.

25. Fleischer, M.; Meixner, H., Fast Gas Sensors Based on Metal Oxides Which Are Stable at High Temperatures. *Sens. Actuators, B* 1997, 43, 1-10.
26. Schwebel, T.; Fleischer, M.; Meixner, H.; Kohl, C.-D., CO-Sensor for Domestic Use Based on High Temperature Stable Ga_2O_3 Thin Flms. *Sens. Actuators, B* 1998, 49, 46-51.
27. Fleischer, M. S., M.; Kohl, C.-D.; Mexiner, H., A Selective H_2 Sensor Implemented Using Ga_2O_3 Thin-Films Which Are Covered with A Gas-Filtering SiO_2 Layer. *Sens. Actuators, B* 1996, 35, 297-302.
28. Tan, S. T.; Tan, C. H.; Chong, W. Y.; Yap, C. C.; Umar, A. A.; Riski Titian, G.; Hock Beng, L.; Kok Sing, L.; Yahaya, M.; Salleh, M. M., Microwave-Assisted Hydrolysis Preparation of Highly Crystalline Zno Nanorod Array for Room Temperature Photoluminescence-Based CO Gas Sensor. *Sens. Actuators, B* 2016, 227, 304-312.
29. Bai, J.; Zhou, B., Titanium Dioxide Nanomaterials for Sensor Applications. *Chem. Rev.* 2014, 114, 10131-76.
30. Lin, H.-J.; Baltrus, J. P.; Gao, H.; Ding, Y.; Nam, C.-Y.; Ohodnicki, P.; Gao, P.-X., Perovskite Nanoparticle-Sensitized Ga_2O_3 Nanorod Arrays for CO Detection at High Temperature. *ACS Appl. Mater. Interfaces* 2016, 8, 8880-8887.
31. Lin, H.-J. G., H.Y.; Gao, P.X., Perovskite Nanoparticle Sensitized Ga_2O_3 Nanorod Arrays For Highly Selective NO_2 Detection Over O_2 At 800°C 2016.
32. Lin, H.-J. G., P.X., UV-Enhanced CO Sensing Using Ga_2O_3-Based Nanorod Array at Elevated Temperature. 2016.
33. Schaub, R.; Wahlstro¨m, E.; Rønnau, A.; Laegsgaard, E.; Stensgaard, I.; Besenbacher, F., Oxygen-Mediated Diffusion of Oxygen Vacancies on the TiO_2(110) Surface. *Science* 2003, 299, 377-379.

CHAPTER 8

Summary and Outlook

8.1: Summary

As an important enabling technology for monitoring and controlling the combustion environments that are normally involved in various advanced energy systems, high temperature chemical sensors have immediate impact in automotive, chemical, mechanical and energy industries, exemplified by mobile engines and gas turbine power stations. Over the past few decades, the research and development of solid state gas sensors for high temperature applications has been focused on the ease of fabrication, sustainable and robust devices with good sensitivity, selectivity and long-term stability, so-called '3S'. Here in this dissertation work, we successfully synthesized large scale three-dimensional (3-D) β-Ga_2O_3 nanorod arrays (NRAs) on Si substrates using a cost-effective hydrothermal deposition process followed by high temperature annealing. Based on these 3-D β-Ga_2O_3 NRAs, we design and investigate three material and sensor design strategies in order to improve and understand the new materials architecture and sensing mechanism at high temperature. Firstly, using trace amount of perovskite oxide nanoparticles decoration, 3-D β-Ga_2O_3 NRA gas sensors are not only sensitized to a degree that rivals noble metal nanoparticle sensitizing effect, but also greatly enhanced in their oxidative gas selectivity, e.g., in NO_2 detection over O_2. Secondly, post hydrogen treatment is utilized to tune the defects in the β-Ga_2O_3 to help enhance the sensor performance at high temperature. Furthermore, UV-assisted photoelectron generation in wide bandgap β-Ga_2O_3 significantly enhanced the sensor performance. Finally, an in-

depth understanding of the 3-D architecture and sensing mechanism is being pursued using various complementary spectroscopy tools such as Temperature Programmed spectroscopy and Fourier Transform Infrared (FTIR) spectroscopy, as well as *ex-situ* and *in-situ* X-ray Photoelectron Spectroscopies (XPS).

Specifically in Chapter 1, we briefly introduce several classic configurations of solid-state gas sensors applied at high temperature, including equilibrium potentiometric, non-equilibrium potentiometric, amperometric and resistive sensors, the corresponding working mechanisms are also discussed in this section. Besides, due to the resistor-type gas sensors used in this dissertation was made of nanorod arrays, the physical and chemical properties of one-dimensional nanorods were also introduced. Additionally, the challenges of up-to-date research on high temperature gas sensor are also described.

The high temperature gas sensor devices were made of β-Ga_2O_3 nanorod arrays through the combination of the hydrothermal method and post-annealing treatment due to its easy process, cost-efficient facility to generate one-dimensional nanorod on silicon substrates. Therefore, the precursors, fabrication-related facilities and its corresponding working mechanism, such as hydrothermal synthesis or radio frequency sputtering technique, were described in chapter 2. The characterization techniques, such as XRD, SEM and TEM are also described in this section.

In Chapter 3, the experimental details and the growth mechanism of GaOOH nanorod arrays, which were fabricated on Si substrates topped with SnO_2 as the seed layer by hydrothermal synthesis, were discussed in this section. The GaOOH nanorod arrays can be fully transformed to β-Ga_2O_3 nanorod arrays by post-annealing treatment at 1000 °C. In addition, the β-Ga_2O_3 nanorod arrays were employed as *insitu* and real-time resistive-

type gas sensors to detect gases in the high temperature, which would be discussed in the following chapters.

In Chapters 4-5, through surface decoration approaches, the sensitivity and selectivity of resistor-type gas sensors for reducing, oxidizing gas detection in the high temperature, which is rather challenging. In the chapter 4, we employed perovskite-type $La_{0.8}Sr_{0.2}FeO_3$ nanoparticle surface decoration of 10 nm on β-Ga_2O_3 nanorod to improve around one order of magnitude enhanced sensitivity to CO at 500 °C. Based on the X-ray photoelectron spectroscopy studies, it suggests that LSFO nanoparticle sensitization effect is attributed to a spillover-like effect associated with the gas-LSFO-Ga_2O_3 triple-interfaces that spread the negatively charged surface oxygen ions from LSFO nanoparticles surfaces over to β-Ga_2O_3 nanorod surfaces with faster surface CO oxidation reactions.

In Chapter 5, β-Ga_2O_3 nanorod arrays demonstrated good sensitivity to NO_2 at 800 °C, with excellent reversible and reproducible response characteristics. In addition, the sensitivity towards NO_2 can be further enhanced by nearly an order of magnitude, along with much faster temporal senor response dynamics through the surface decoration of perovskite-type $La_{0.8}Sr_{0.2}CoO_3$ (LSCO) nanoparticles. We also observe a remarkable selectivity toward oxidative gases as we demonstrate the differentiation of NO_2 over O_2, by virtue of the bi-fold enhancements in both sensitivity and response time.

In Chapter 6, additional ultra-violet illumination was introduced into the system, including pristine β-Ga_2O_3, $La_{0,8}Sr_{0.2}FeO_3$(LSFO)-decorated β-Ga_2O_3. The enhancement of sensing properties for detecting CO gas under UV light illumination at high temperature is due to the increase of photoinduced electron-hole pairs. In the condition of

LSFO-decorated β-Ga_2O_3 nanorad array sensor under UV light, the enhancement is through the combination of sensitizing effect and photocurrent.

In Chapter 7, we attempt to control the defects (oxygen vacancies) to modify gas sensing performance by post-hydrogen treatments on pristine β-Ga_2O_3 nanorod arrays. The resulting H_2-treated Ga_2O_3 material serves as an efficient high temperature gas-sensing material for specific carbon monoxide (CO) detection with both high sensitivity and fast response/recovery. Such H_2-treated concept is anticipated to give a promising motivation to rational design of gas sensing device at high temperature.

In summary, this dissertation developed novel high temperature gas sensors with good sensitivity and selectivity for reducing and oxidizing gas detection by incorporation of perovskite nanoparticles. Equipped with UV illumination or hydrogen treatments can also improve the gas sensing performances.

8.2: Outlook

According to the results from Chapters 3 & 4, the sputtered-perovskite-nanoparticles would enhance the gas sensing performance. However, based on the TEM images and line scanning of X-ray energy disperse spectroscopy spectra, the distribution of perovskite nanoparticles was uneven and non-uniform across β-Ga_2O_3 nanorod due to the sputtering shadow effect. Therefore, it is believed that well-distributed perovskite nanoparticle might lead to better gas sensing performance due to the creation of more heterocontacts between perovskite nanoparticles and β-Ga_2O_3 nanorods. Several perovskite materials thin films have been successfully fabricated by atomic layer deposition, such as $LaCoO_3$, $La_{1-x}Sr_xFeO_3$, $LaAlO_3$ or $LaGaO_3$.[1-4] Therefore, atomic layer

deposition technique would be a promising method to enhance the structure and dispersion controllability over the size, shape and interfaces of the comprised oxide-perovskite core-shell nanowire arrays. This undoubtedly will provide a good opportunity to further study and understand the electronic transport in the perovskite nanoparticle catalytic sensitizing effect. Simply from physical geometry stand, perovskite nanoparticles could be spread all over the porous β-Ga_2O_3 nanorods to further enhance gas-sensing performance. Meanwhile, through the creation of UV light-assisted high temperature sensing mode, steady and high intensity of UV light source which can sustain at high temperature is critically important toward more robust and selective detection of chemical species at high temperature. As an important extension of the current work, quartz optic fiber with silica core/silica clad could be a good solution for providing UV-light source at high temperature (up to ~1000 °C).

Finally, the post-hydrogen treatments are proved to be able to help manipulate and control the defect conditions in the sensing nanomaterials and lead to different levels of deep/shallow donor states, which could be further investigated and understood by various optical spectroscopies such as steady-state and transient (temporally resolved) dynamic photoluminescence spectroscopies.